MEDNARODNA
PODIPLOMSKA ŠOLA
JOŽEFA STEFANA

7. ŠTUDENTSKA KONFERENCA MEDNARODNE PODIPLOMSKE ŠOLE JOŽEFA STEFANA

Zbornik - 1. del

7th JOŽEF STEFAN INTERNATIONAL POSTGRADUATE SCHOOL STUDENTS' CONFERENCE

Proceedings - Part 1

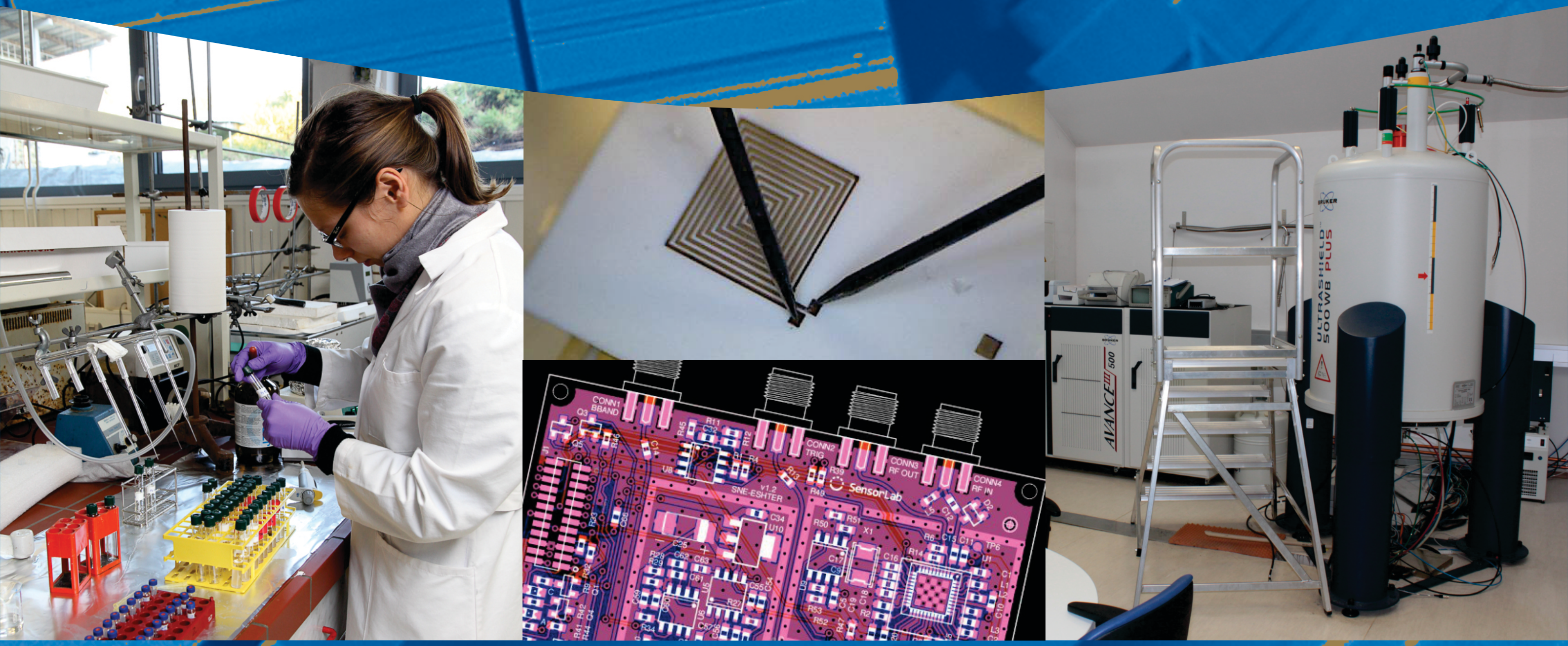

20. - 21. 05. 2015, Ljubljana

Zbornik 7. Študentske konference Mednarodne podiplomske šole Jožefa Stefana
(Proceedings of the 7th Jožef Stefan International Postgraduate School Students Conference)

Uredniki / Editors:
Andraž Rešetič
Ana Kroflič
Aleksander Matavž
Melisa Junuzović
Janja Vidmar
Maja Somrak

Založnik / Publisher:
Mednarodna podiplomska šola Jožefa Stefana, Ljubljana

Dosegljivo na / Attainable at:
http://ipssc.mps.si/2015/proceedingsIPSSC2015Papers.pdf

Ljubljana, maj 2015

Konferenco organizira Študentski Svet Mednarodne podiplomske šole Jožefa Štefana
(The Conference is organized by Jožef Stefan International Postgraduate School - IPS Student Council)

CIP - Kataložni zapis o publikaciji
Narodna in univerzitetna knjižnica, Ljubljana

5/6(082)
378.046-021.68:001.891(497.4)(082)

MEDNARODNA podiplomska šola Jožefa Stefana. Študentska konferenca (7 ; 2015 ; Ljubljana)
Zbornik = Proceedings / 7. študentska konferenca Mednarodne podiplomske šole Jožefa Stefana = 7th Jožef Stefan International Postgraduate School Students' Conference, 20.-22. 5. 2015, Ljubljana ; [organizira študentski svet Mednarodne podiplomske šole Jožefa Štefana = organized by Jožef Stefan International Postgraduate School - IPS Student Council] ; uredili, edited by Andraž Rešetič ... et al.]. - Ljubljana : Mednarodna podiplomska šola Jožefa Stefana, 2015

ISBN 978-961-92871-9-4
1. Rešetič, Andraž 2. Mednarodna podiplomska šola Jožefa Stefana (Ljubljana)
279459840

7. ŠTUDENTSKA KONFERENCA MEDNARODNE PODIPLOMSKE ŠOLE JOŽEFA STEFANA

ZBORNIK - 1. DEL

7th JOŽEF STEFAN INTERNATIONAL POSTGRADUATE SCHOOL STUDENTS' CONFERENCE

PROCEEDINGS - PART 1

Uredili / Edited by

Andraž Rešetič, Ana Kroflič, Aleksander Matavž, Melisa Junuzović, Janja Vidmar
in Maja Somrak

20. - 21. 05. 2015, Ljubljana

Organizacijski odbor / Organising Committee

Redakcijski odbor / Technical Review Committee

IPSSC: Microstructure, mechanical and electrical properties of Glass Fiber Reinforced Composites (GFRC)

Barbara Bertoncelj[1,2], Katarina Vojisavljević[3], Janez Rihtaršič[1], Gregor Jelenc[1], Barbara Malič[3]
[1] Domel, d.o.o., Železniki, Slovenia
[2] Jožef Stefan International Postgraduate School, Ljubljana, Slovenia
[3] Jožef Stefan Institute, Ljubljana, Slovenia
barbara.bertoncelj@domel.com

Abstract. In this study, the influence of E-glass fiber and mineral filler content on the microstructure, physical, mechanical and dielectric properties of Glass Fiber Reinforced Composites (GFRC) was investigated. Five sets of GFRC, based on polymer resin with varying E-grade glass fibers and $CaCO_3$ mineral filler weight fractions (15/64, 20/59, 25/54, 30/49, 35/44), were commercially prepared. Test specimens were prepared by compression molding. Scanning Electron Microscope images revealed that at higher concentrations, the fibers clustered together, resulting in heterogeneous microstructures. Characterization of the composites showed that glass fiber content and distribution significantly affects the mechanical properties. The flexural strength of the composites decreased with increasing glass fiber content. The dielectric constant ε` decreased with increasing fiber content.

Keywords: glass fiber reinforced composites, E-glass fibers, microstructure, flexural strength, electrical properties

1 Introduction

Over the last years, GFRC have gradually replaced traditional structural materials, such as steel and aluminium, especially in applications where strength to weight ratio is important, for example in construction and building industry. Applications of GFRC are also widespread in automotive, electronic and electro industry. Typical products are car panels, internal car parts, switchgears, housings of domestic applications, etc.

Good dimensional stability, chemical and corrosion resistance and good insulating properties are favorable properties of GFRC over steel and Al. Furthermore, manufacturing processes of GFRC products, such as injection molding, is energy less-consuming especially for the reason that molded products are made in one piece and consequently they do not need additional machining. Although, GFRC have been in use for several decades, continuous improvement of properties and competitive price still makes them attractive for an even wider use.

The main components of GFRC are polymer matrix and glass fibers, each of them having its own function. Polymer resin acts like a glue - holding the fibers in a proper spatial orientation, and furthermore helps in stress transfer between the fibers. Since polymers typically have low strength and stiffness, fibers are added to improve the mechanical properties of the composite material. Thus, the final properties of the composite are determined by the type and quantity of the fibers. In combination with the polymer matrix, glass fibers are the most frequently used. Sometimes, inorganic fillers, such as Al_2O_3, mica or $CaCO_3$ are incorporated into the polymer matrix to modify the viscosity of the polymer resin, to lower the overall cost of the material and to achieve some special properties such as improved dimensional stability or self-extinguishing.

Physical and mechanical properties of GFRC are influenced by the phase composition, physical and chemical properties of individual components and fiber distribution and orientation. Therefore, with appropriate selection and ratio of individual constituents, composites with desired properties can be fabricated.

The aim of this work was to study the influence of E-glass fibers on the microstructure, mechanical and electrical properties of GFRC with different weight fractions of glass fibers and mineral filler while keeping the weight fraction of the polymer phase constant.

2 Experimental work

Five sets of GFRC with varying contents of glass fibers and mineral filler were commercially prepared. The compositions of the composites are listed in Table 1. The fibers were 4.5 mm long E-grade glass fibers (“electrical grade” which exhibit low electrical conductivity) [2] with the diameter of 11 μm, as confirmed by scanning electron microscopy (SEM), and the mineral filler was $CaCO_3$ [3]. The polymer phase was kept constant (21 wt%) and was based on thermosetting unsaturated polyester, styrene and additives. Test specimens were prepared by compression molding, according to standard ISO 3167 [4].

Table 1: Composition of GFRC samples.

	Polymer matrix	E-glass fibers	$CaCO_3$
	Content [wt%]		
1	21	15	64
2	21	20	59
3	21	25	54
4	21	30	49
5	21	35	44

The density of the samples was determined by immersion method and calculated using the equation (1),

$$\rho = \frac{m_s}{m_s - m_w} \cdot \rho_w \qquad (1)$$

where the m_s is the mass of the sample in the air, m_w is the mass of the sample when immersed in the water and ρ_w is the density of water at room temperature [5].

Test specimens of individual samples were then cut perpendicular to the filling flow direction of the material during compression molding to obtain cross-sectional and plan-view sections for microstructural characterization. Representative scheme of the sample cutting position and the sample dimensions are shown in Figure 1. The cross-sections and plan-view sections of the test specimens were prepared by the standard metallographic technique, i.e. by grinding and polishing, and examined by scanning electron microscope (SEM, JEOL JSM 5800). Prior to the SEM observations the samples were coated with a thin carbon layer. The SEM micrographs were taken at the accelerating voltage of 20 kV.

The flexural strength of the test specimens was measured by three-point bending method (Alpha 50-5), according to standard ISO 178:2003 [6]. The span between the supports was 64 mm and the crosshead speed was 2.0 mm/min. The test was carried out on 15 specimens of each composition and calculated by the equation (2),

$$\sigma_f = \frac{3Pl}{2bh^2} \tag{2}$$

where σ is the flexural strength, P is the maximum fracture load, l is the span between the supports, b is the width of the sample and h is the height of the sample.

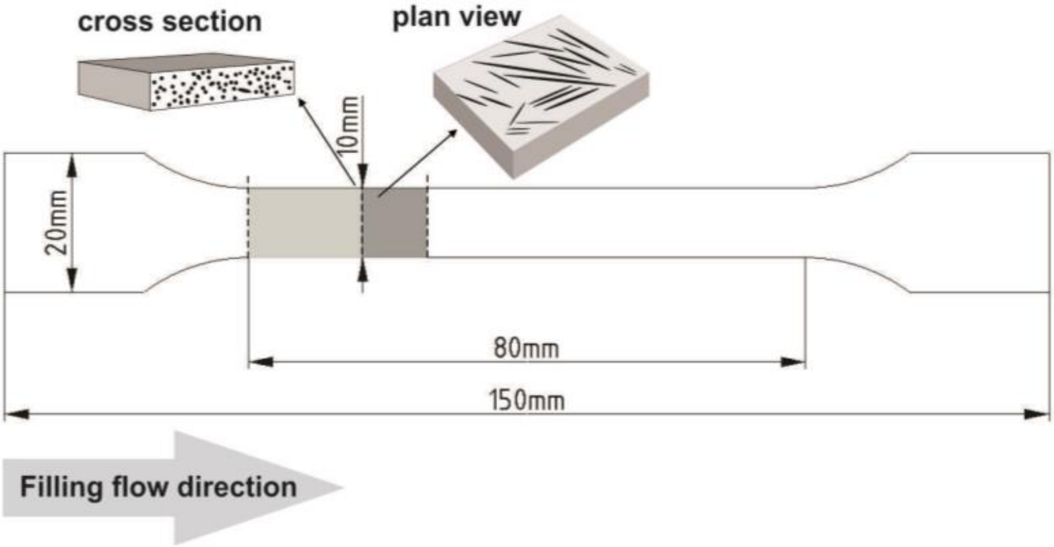

Figure 1: Scheme of the test specimen illustrating the cutting directions for cross-section and plan-view sections for SEM observation. The arrow indicated the flow of the material during molding.

Prior to electrical properties measurement Cr/Au electrodes were applied on the surface of each sample by RF-magnetron sputtering (5 Pascal). The dielectric properties were measured by the Impedance analyzer HP 4284A. The measurements were performed at room temperature over the frequency range from 100 Hz to 1 MHz. The dielectric constant ε' was calculated according to the equation (3),

$$\varepsilon' = \frac{C \cdot d}{\varepsilon_0 \cdot A} \tag{3}$$

where ε' is the dielectric constant, C is the capacitance of the sample, d and A are the thickness of the sample and the area of the electrode, respectively, and ε_0 is the permittivity of free space. The imaginary part of the complex dielectric permittivity ε'' was determined by the equation (4),

$$\varepsilon'' = \varepsilon' \cdot tan\delta \quad (4)$$

where ε'' is the dielectric loss factor, ε' is the dielectric constant and $tan\delta$ is the loss factor.

3 Results and discussion

3.1 Physical properties

The density values are listed in Table 2. The results showed that the samples with different weight fractions of glass fibers have very similar densities, around 2 g/cm^3, which is attributed to the similar densities of EGF (2,54 g/cm^3) and $CaCO_3$ mineral filler (2,65 g/cm^3) [7].

Table 2: Density values of individual GFRC.

Composition (wt% EGF/$CaCO_3$)	Density [g/cm^3]
15/64	2,04
20/59	2,03
25/54	2,02
30/49	2,04
35/44	2,03

3.2 Microstructure

SEM images of plan view and cross-sectional areas are shown in Figure 2. From the micrographs it is evident, that the fibers are mostly oriented perpendicular to the filling direction of the material during molding. At lower EGF content, the distribution of fibers is quite homogeneous (see Figure 2 a), b)). However, at higher fiber contents, above 20 wt%, we observed that fibers are clustered together which is due to the lack of space for fibers to orient in the "proper" direction and consequently the microstructure becomes non-homogeneous with some areas filled only with polymer resin and mineral filler. We observe that a homogeneous distribution of the fibers could not be achieved at higher fiber contents.

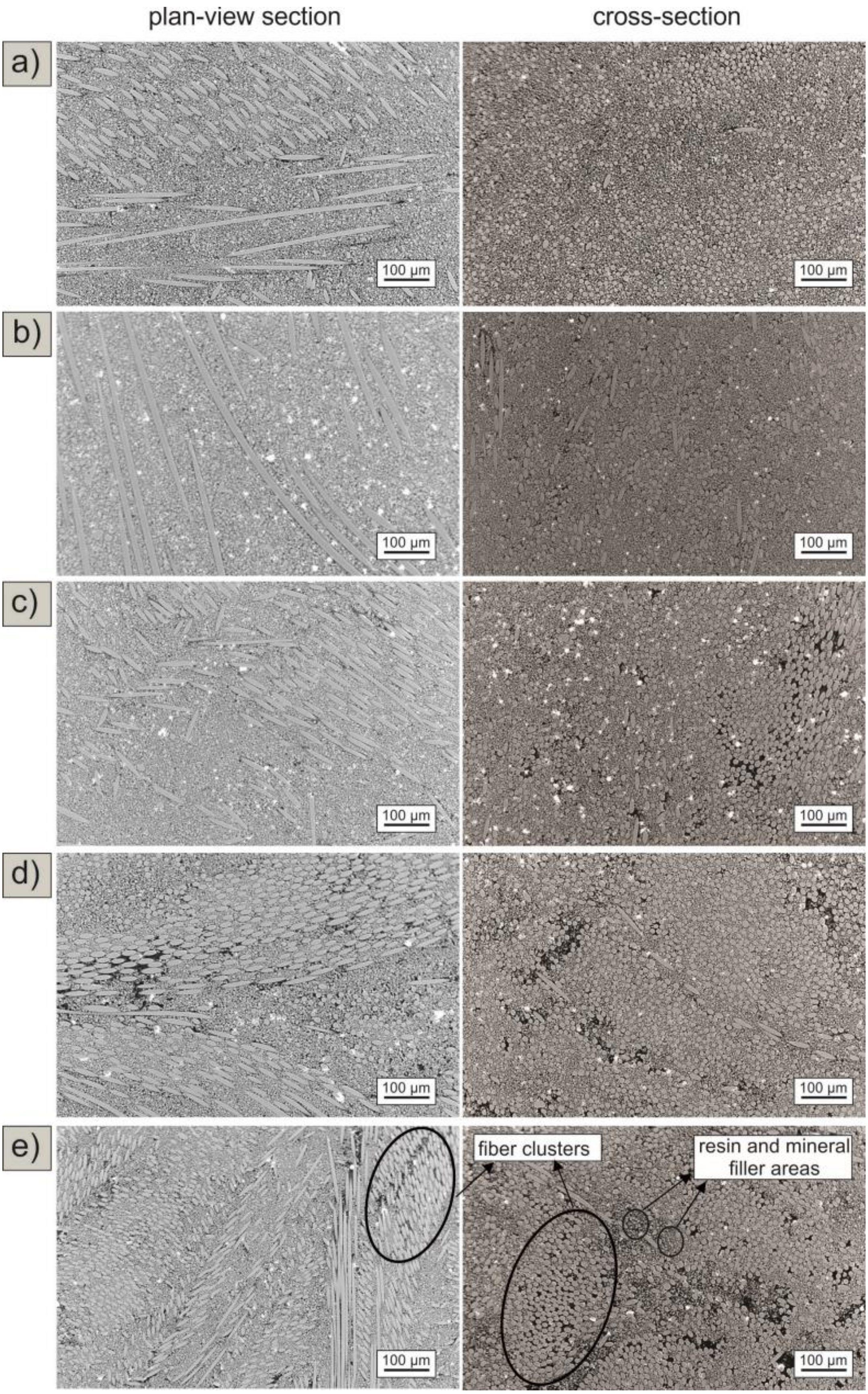

Figure 2: SEM micrographs of plan-view and cross-sectional areas of GFRC: a) 15 wt% of EGF, b) 20 wt% of EGF, c) 25 wt% of EGF, d) 30 wt% of EGF, e) 35 wt% of EGF.

3.3 Mechanical properties

The results of flexural strength measurement of all GFRC are presented in Figure 3. The maximum value of flexural strength was measured with the sample comprising of 15 wt% of EGF, i.e. around 130 MPa. With increasing the EGF content the flexural strength decreased, reaching the final value of 72.3 MPa for the composite with 35 wt% of EGF. The decrease in the flexural strength with increasing EGF content was not expected. However, the deterioration of flexural strength was attributed to the increasingly non-homogeneous fiber distribution in the composites with higher fiber contents. Fiber clustering was observed from the SEM micrographs, which is especially apparent in the composites with fiber contents above 20 wt% (see Figure 2 c),d),e)). Therefore increased fiber-fiber interactions could contribute to the less efficient stress transfer in the material.

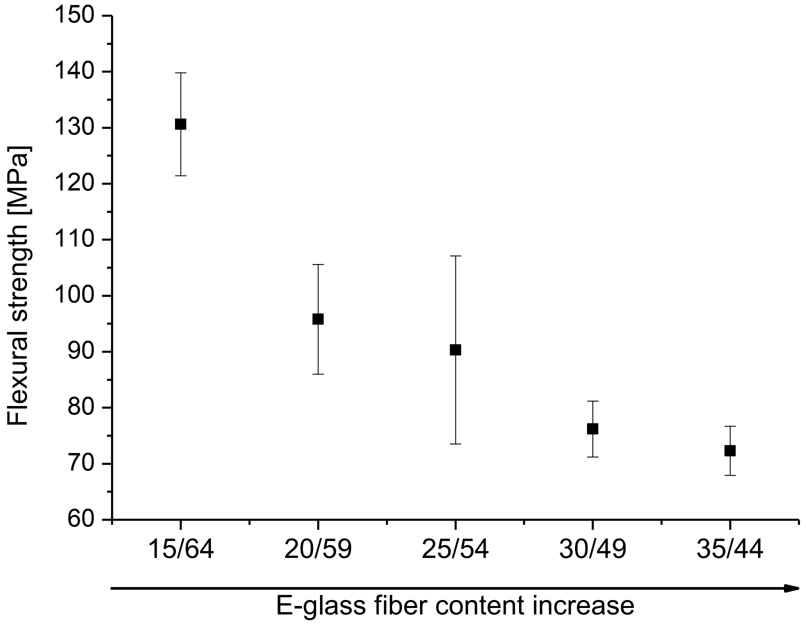

Figure 3: Flexural strength of GFRC samples.

3.4 Dielectric properties

The values of dielectric constant measured at different frequencies are presented in Figure 4. The dielectric constant ε` for the sample with 15 wt% of EGF at 100 Hz was 6.86 and 6.65 at 1MHz. The results show that ε` of all composites decreases with increasing frequency. The result is in agreement with [8]. With increasing the weight fraction of glass fibers the ε` decreases, with the exception of the composition with 35 wt% of EGF. Figure 4 also shows the frequency dependence of dielectric loss factor ε`` for all composites. The value ε`` for the sample with 15 wt% of EGF was 0.14 at 100 Hz and 0.05 at 1MHz. The results also show that ε`` is increasing with increasing glass fiber content.

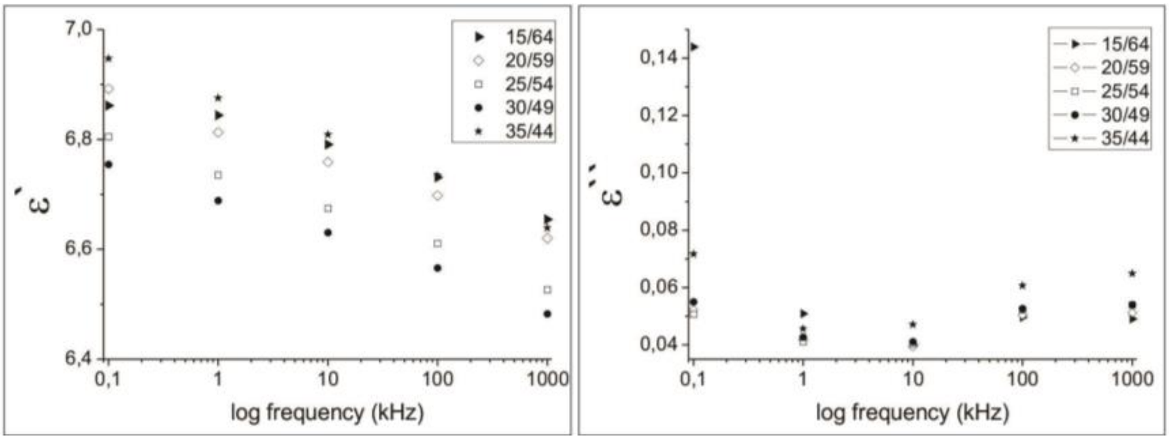

Figure 4: Frequency dependence of dielectric constant ε` and dielectric loss factor ε`` for composites with varying E-glass fiber content.

4 Conclusions

In order to study the effect of EGF content on the microstructure, mechanical and electrical properties 5 sets of GFRC were commercially fabricated with varying fiber and mineral filler contents. The density of GFRC samples did not change with the composition and was around 2 g/cm^3. From the SEM micrographs it was observed that fiber distribution at lower weight fractions of EGF is quite homogeneous. However, microstructures of the samples with higher EGF contents, above 25 wt%, revealed a non-homogeneous distribution of the fibers, i.e. clusters of fibers and areas filled only with the resin and mineral filler. We connect the observed non-homogeneous microstructure at higher fiber contents with the deterioration of flexural strength. The results showed that flexural strength of the composites decreased with increasing EGF content which was in contrast to the expected reinforcing effect of EGF. The room temperature dielectric permittivity in all composites decreased with increasing frequency and with increasing glass fiber content.

5 Acknowledgements

We acknowledge the assistance of colleagues from Electronic Ceramics Department, Jožef Stefan Institute, Silvo Drnovšek and Tanja Pečnik, for their help with measuring dielectric properties. One of the authors (B.B.) gratefully acknowledges the financial support of the Ministry for education, science and sport of Republic of Slovenia and European Commission through the European Social Fund. B.M. and K.V. acknowledge the support of the Slovenian Research Agency (P2-0105).

References:

[1] A. Kelly, C.H. Zweben (eds.). *Comprehensive composite materials*, Elsevier, Amsterdam, 2000.

[2] F.T. Wallenberger, P.A. Bingham (eds.). *Fiberglass and glass technology*. Springer Scince+Business Media, New York, 2010.

[3] B. Bertoncelj, K. Vojisavljević, J. Rihtaršič, G. Jelenc, B. Malič. Characterization of glass fiber reinforced composites for housing of electrical motors. In A. Žemva (Ed.), P. Šorli (Ed.), I. Šorli, (Ed.). *Proceedings of the 49th MIDEM International Conference on Microelectronics, Devices and Material*, Kranjska Gora, Slovenia, 2013.

[4] ISO 3167: Plastics-Multipurpose test specimens. International Organization for Standardization. https://www.iso.org.

[5] Mohamed N. Rahaman. *Ceramics Processing*. CRC Press, Boca Raton, 2007.

[6] ISO 178:2003: Plastics. Determination of flexural properties. International Organization for Standardization. https://www.iso.org.

[7] William D. Callister. *Materials science and engineering*. John Wiley & Sons, New York, 2007.

[8] M. Akram, A. Javed, T. Z. Rizvi. Dielectric properties of industrial polymer composite materials. *Turkish Journal of Physics*, 29(6):355-62, 2005.

For wider interest

Composites consist of two or more distinct materials, whose combination results in improved properties that cannot be achieved only by one of the constituents.

Glass fiber reinforced composites (GFRC) are combination of polymer matrix and glass fibers, each having its own role that contributes to final properties. Polymer matrix surrounds the fibers and holds them in the "proper" spatial arrangement. Since polymers most often have low strength and stiffness, glass fibers are added to reinforce the polymer and improve its mechanical properties.

Final properties of GFRC depend on chemical and physical properties of individual constituents, their relative amounts and spatial orientation and distribution of fibers.

In recent years GFRC have replaced metals and also found new applications in many industry areas, such as in construction, transportation, electro and electronic industry. Main advantages of GFRC over metals are high strength and stiffness in combination with low density. For example, use of GFRC in vehicles results in lower overall weight and consequently increases fuel savings. Such properties make them attractive for an even wider use. Thus, understanding of relationship between *structure-composition-properties* of GFRC can help in developing new composites with improved properties and in optimizing the existing materials.

Photogeneration of Charge Carriers in Few-Layer MoS_2

Tetiana Borzda[1,2], **Christoph Gadermaier**[1,2], **Natasa Vujicic**[1,3], **Peter Topolovsek**[1,2], **Milos Borovsak**[1], **Tomaz Mertelj**[1], **Daniele Viola**[4], **C. Manzoni**[4], **E. A. A. Pogna**[4], **D. Brida**[5], **Maria Rosa Antognazza**[6], **Francesco Scotognella**[6], **Guglielmo Lanzani**[6], **Giulio Cerullo**[4], **and Dragan Mihailovic**[1,2,7]

[1] Department of Complex Matter, Jozef Stefan Institute, Jamova 39, 1000 Ljubljana, Slovenia

[2] Jozef Stefan International Postgraduate School, Jamova 39, 1000 Ljubljana, Slovenia

[3] Institute of Physics, Bijenicka 46, 10000 Zagreb, Croatia

[4] Department of Physics, Politecnico di Milano, P. Leonardo da Vinci 32, 20133 Milan, Italy

[5] Department of Physics, University of Konstanz, PO box M696 78457 Konstanz, Germany

[6] Center for Nano Science and Technology, Italian Institute of Technology, Via Pascoli 70/3, 20133 Milano, Italy

[7] Center of Excellence in Nanoscience and Nanotechnology, Jamova 39, 1000 Ljubljana, Slovenia

tetiana.borzda@ijs.si

Abstract. The two-dimensional semiconductor MoS_2 in its mono- and few-layer form is expected to have a significant exciton binding energy of several 100 meV, leading to the consensus that excitons are the primary photoexcited species. Nevertheless, even single layers show a strong photovoltaic effect and work as the active material in high sensitivity photodetectors, thus indicating efficient charge carrier photogeneration (CPG). Here we use continuous wave photomodulation spectroscopy to identify the optical signature of long-lived charge carriers and femtosecond pump-probe spectroscopy to follow the CPG dynamics. We find that intitial photoexcitation yields a branching between excitons and charge carriers, followed by excitation energy dependent hot exciton dissociation as an additional CPG mechanism. Based on these findings, we make simple suggestions for the design of more efficient MoS_2 photovoltaic and photodetector devices.

Keywords: Two-dimensional crystals, MoS_2, transition metal dichalcogenides, excitons, femtosecond spectroscopy, photomodulation, photophysics, charge generation.

1 Preparation and Characterization of Samples

Recent progress in the exfoliation of layered materials [1], [2] and the nanofabrication of functional structures has revived the interest in two-dimensional materials with properties complementary to graphene, in particular transition metal dichalcogenides [3], [4] (TMDs) such as MoS_2. Depending on the metal atoms' coordination and oxidation state, TMDs can be metallic, semimetallic, or semiconducting. Additionally, some TMDs show superconductivity [5], charge-density waves [6] and hidden electronically ordered phases [7]. Their potential for electronics has become evident by the realization of a field effect transistor [8] (FET) and a logic circuit device [9] based on a single flake of monolayer MoS_2.

The optical absorption of MoS_2 in the visible spectral range shows four excitonic resonances [10], commonly labeled (see Figure 1a) A to D at 1.9, 2.1, 2.7, and 2.9 eV. The spectral positions of these resonances are almost independent of the number of layers, while the indirect band gap is at 1.2 eV in the bulk and grows progressively as the number of layers is reduced, even exceeding the energy of the A exciton resonance for the monolayer. Hence the monolayer, contrary to bi- and multilayers, behaves like a direct gap semiconductor and shows significant fluorescence [11], [12]. The exciton binding energy for bulk MoS_2 has been determined to be 45 meV and 130 meV for the A and B excitons, respectively [13]. Both exciton binding energies increase upon decreasing the sample thickness, with estimates for monolayers [14-16] ranging from 0.4 to 0.9 eV. Despite this high exciton binding energy, monolayer MoS_2 shows a strong photovoltaic effect [17] and potential for high sensitivity photodetectors [18]. Both findings require efficient charge carrier photogeneration (CPG), either via direct excitation of mobile carriers or via exciton dissociation.

The spectral signature of charge carriers has been identified by absorption and fluorescence spectroscopy of MoS_2, where the charge concentration is varied either via the gate voltage in a FET geometry [19] or via adsorption [20] or substrate doping [21]. The absorption peaks of charges are red-shifted by about 40 meV compared to the ground state absorption into the A and B excitons and have been attributed to optical transitions from a charged ground state to a charged exciton (trion). The possibility of alternative interpretations, such as polarons [22], [23] or Stark effect in the local electric field of the charges [24-26] does not compromise the identification of these absorption peaks as belonging to charges.

Here we use continuous wave (cw) photomodulation (PM) and femtosecond pump-probe spectroscopy to identify the spectral features of photogenerated charges and trace their dynamics, starting with their generation either by direct impulsive excitation into the charge continuum or via exciton dissociation. We exfoliated MoS_2 in ethanol, following the protocol in Ref [1]. The dispersion was dried and the obtained few-layer flakes were re-dispersed in a solution of PMMA, a transparent and electronically inert polymer. This dispersion was spin-cast onto a quartz substrate, yielding a macroscopic PMMA film with a homogenous greenish-yellow color characteristic of thin MoS_2 films [27] (see Fig. 1a).

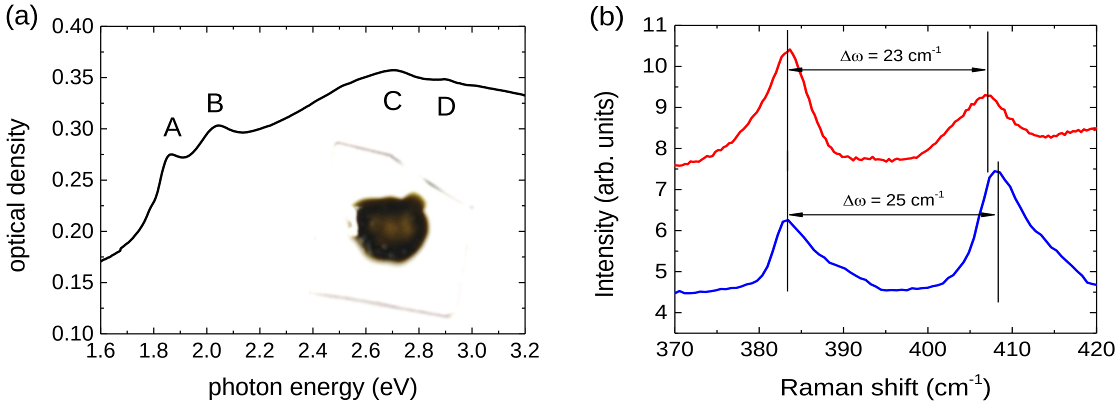

Figure 1: (a) Absorption spectrum of the sample of MoS_2 in PMMA. Inset shows a photograph (the dark area has a diameter of approximately 7-8 mm). (b) Raman spectra for two excitation wavelengths at 633 nm (red line) and 488 nm (blue line).

PMMA in this sample serves as a matrix that holds an ensemble of flakes with lateral size [1] of few-hundred nm. The distance Δω between the two Raman peaks around 400 cm^{-1} is generally viewed as the most robust measure of the flake thickness [28]. From the Raman spectra in Fig 1b we obtain $\Delta\omega = 23$ cm^{-1} for excitation at 633 nm and $\Delta\omega = 25$ cm^{-1} at 488 nm. Within the distribution, various thicknesses contribute differently at the two excitation wavelengths [29]. Overall, the Raman spectra indicate a flake thickness distribution that is dominated by three- to six-layer flakes.

The advantages of this kind of sample compared to individual flakes are the ease of fabrication and handling and the possibility to use any spectroscopic technique without the need for high-resolution optical microscopy. MoS_2 flakes embedded in PMMA are in a slightly different environment than mono- or few layer flakes on dielectric substrates used in previous femtosecond studies [30], [31]. However, as our results will show, the spectra and the relaxation times of the signal are very similar to those obtained on individual few-layer flakes. Hence the present study directly extends existing knowledge on the femtosecond behavior of few-layer MoS_2.

2 Results and Discussion

The absorption spectrum in Fig. 1a shows the characteristic A and B exciton resonances, which are broader and red-shifted compared to undoped MoS_2, as is typical of commercial MoS_2 of mineral origin [32], which is doped due to dislocations induced by the exfoliation and due to (mostly metallic) impurities. Hence, each of the two absorption peaks is actually an overlap of at least two contributions: neutral ground state to exciton absorption at the higher energy side of each peak and lowest charged state to excited charged state at the lower energy side. For the A peak, an even lower energy contribution has been identified [32], which has alternatively been ascribed to a surface trapped exciton [33], an edge state [34], or a plasmon resonance [35], so that peak A actually arises from the overlap of three peaks. Similar to the notation in Refs 19, 20, and 32, we will use the labels L, A^-, and A^0 for the low energy peak, charge peak and exciton peak of the A resonance, and B^- and B^0 for the charged and neutral contributions to the B resonance. Please note that, contrary to electrical or chemical doping, photoexcitation generates charges in pairs of opposite polarities. However, although we expect the signatures of the corresponding positive charges at the same spectral positions, we know only those of the negative charges, hence our labeling.

To identify long lived photoexcitations we performed cw PM spectroscopy. Here, a cw laser with 3.1 eV photon energy used for exciting the sample is periodically modulated via a mechanical chopper. The relative change $\Delta T/T$ of the transmitted light from a halogen lamp is measured via phase sensitive detection. Those photoexcitations whose population changes significantly over the modulation cycle (i.e. their lifetime is long enough to build up sufficient population while the laser is on and short enough to sufficiently reduce their population while it is off) are identified in the cw PM spectrum via their photoinduced absorption (negative $\Delta T/T$) transitions to higher excited states. Concomitantly with the increase of photoexcited populations, the ground state population and its associated absorption is reduced (photobleaching, positive $\Delta T/T$). The cw PM spectrum at room temperature upon excitation at 3.1 eV, above the C and D exciton resonances, is shown in Fig. 2a. The signal is largely in phase with the modulation of the photoexcitation, with a negligible quadrature contribution. This means that the populations at the origin of the signal can easily follow the modulation at 245 Hz, implying that the lifetimes of the respective photogenerated species are much shorter than the modulation period of ~4 ms.

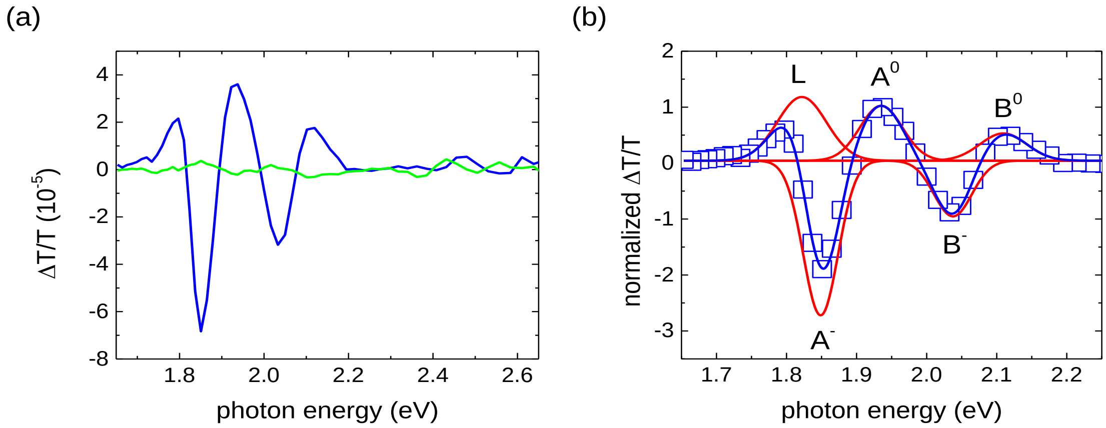

Figure 2: (a) CW photoinduced absorption spectrum of MoS_2 in PMMA at room temperature for excitation at 3.1 eV. In-phase (blue) and quadrature (green) signal components are shown for a modulation frequency of 245 Hz. (b) Five Gaussian fits (red) whose sum (blue) fits the normalized in-phase spectrum (open squares).

The main features of the spectrum are three positive (photobleaching) and two negative (photoinduced absorption) peaks. We fit the spectrum using five overlapping Gaussians (see Fig 2b), which represent the thermal and disorder-induced (in particular by polydispersity of flake thickness) broadening of the electronic resonances. The strong overlap between neighboring peaks makes them appear narrower than their actual lineshape and connected by an almost straight line, masking the inflection points characteristic of isolated Gaussian peaks. The spectral positions of the five peaks correspond very well with the three neutral and two charge peaks discussed in References 19, 20, and 32. Assuming the same origin for the peaks in the PM spectrum, we obtain a straightforward interpretation. Upon photoexcitation, the number of electrons in the neutral ground state is reduced, and the number of charge carriers is increased. Hence the absorption features L, A^0, and B^0 from transitions between neutral states are reduced, resulting in a positive $\Delta T/T$ (photobleaching), while the absorption features A^- and B^- from charges are increased, yielding a negative $\Delta T/T$ (photoinduced absorption).

Alternatively, one could interpret the PM spectrum based on its resemblance of a derivative lineshape. A photoinduced blue shift of the absorption spectrum would result in a ΔT/T contribution that follows the first derivative of the absorption spectrum (or a negative first derivative for a red shift); a photoinduced broadening of the absorption peaks would contribute a negative second derivative. If we interpreted our spectrum in terms of derivative lineshapes, it would be dominated by a positive second derivative, which indicates a photoinduced line narrowing. We are not aware of any such mechanism. However, the A peak is composed of the three overlapping narrower peaks L, A^-, and A^0 (no equivalent to the L peak has yet been identified for the B peak, but we may extrapolate our reasoning also to B). In our proposed scenario photoexcitation generates charges and the middle peak A^- increases at the expense of the other two, which decreases the overall width of the A peak. Hence, CPG leads to an apparent photoinduced line narrowing, which explains the positive second derivative lineshape.

To investigate CPG in real time, we now turn to femtosecond optical pump-probe spectroscopy. Like cw PM, this technique measures the relative change in transmission $\Delta T/T$. However, rather than continuously, the sample is photoexcited at a well-defined point in time by a fs laser pulse (the pump) and the transmission spectrum is measured with a second fs laser pulse (the probe) at a well-defined delay after the pump. Scanning the pump-probe delay allows to follow the evolution of the photoexcitated states' populations. We start by comparing the $\Delta T/T$ signal for excitation at 3.1 eV at long pump-probe delay (300 ps) with the cw PM (see Fig. 3a). The two normalized spectra are very similar, with three important differences: the L peak is absent, there is an additional broad photoinduced absorption feature peaking around 2.45 eV, and the whole spectrum is red shifted. The red shift of the whole spectrum is more pronounced at higher pump intensities (see Fig 3b) and shorter pump-probe delays (see Figs 3c and d).

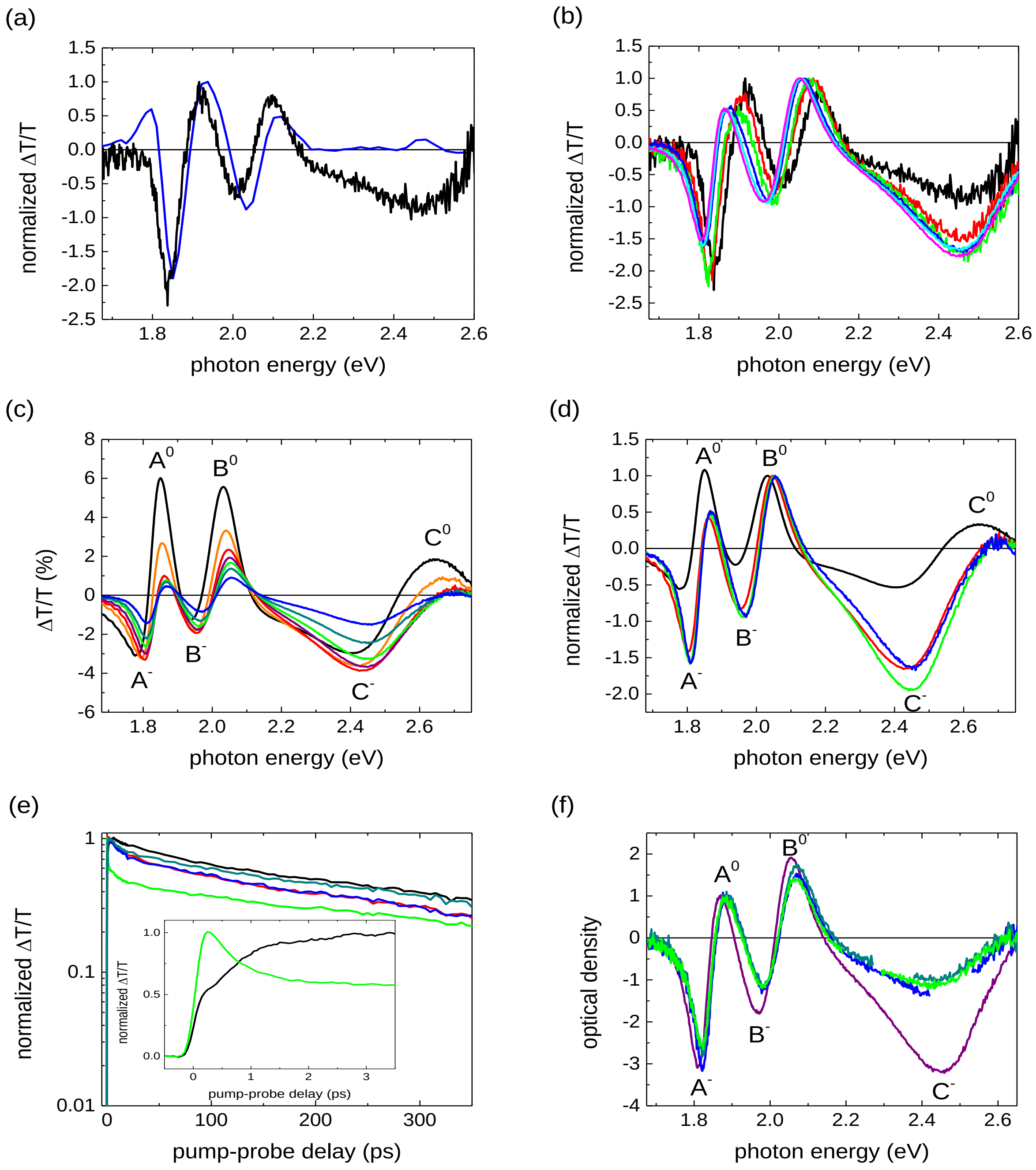

Figure 3: (a) Normalized cw photomodulation spectrum of MoS_2 in PMMA (blue) compared to the fs transient spectrum at 300 ps pump-probe (black) delay for 2 10^{14} cm^{-2} excitation fluence, 3.1 eV pump photon energy (b) pump-probe spectra at 300 ps normalized to the B exciton peak for different pump fluences at 3.1 eV pump photon energy: 2 (black), 3(red), 6 (green), 20 (blue), 40 (cyan) and 80 10^{14} cm^{-2} (c) absolute and (d) normalized (to the B exciton peak) pump-probe spectra for 4 10^{15} cm^{-2} pump fluence at delays 300 fs (black), 1 ps (orange), 3 ps (red), 10 ps (purple), 30 ps (green), 100 ps (dark cyan), and 300 ps (blue) (e) normalized time traces for different probe energies: 2.48 (black), 2.25 (red), 2.07 (green), 1.94 (blue) and 1.80

eV (dark cyan) (f) normalized spectra at 300 ps pump-probe delay for different pump photon energies: 3.10 (purple), 2.48 (blue), 2.34 (dark cyan) and 2.25 eV (green).

Both these correlations suggest that the red shift is stronger for higher concentration of a certain species of excited states. The most intuitive interpretations are Stark effect due to the local field of photogenerated charges, as has been observed in semiconductor nanocrystals [24], organic semiconductors [25], and carbon nanotubes [26], [36] , inter-excitonic interaction [37] or band gap renormalization, as has been found in semiconducting quantum wells upon photoexcitation [38] and inferred in recent works on semiconducting TMDs [39], [40]. This intensity dependent red-shift also explains how the non-linear optical properties of MoS_2 can change from saturable absorption (i.e. photobleaching) to optical limiting (i.e. photoinduced absorption) as a function of pump intensity [41]. After approximately 3 ps, the spectrum decays without any significant shifts or changes of shape, through a dominant process with a time constant of approximately 500 ps (see Fig. 3e), as previously obtained on few-layer MoS_2 supported on a dielectric substrate [30].

In addition to the previously identified A^-, A^0, B^-, and B^0 peaks, we note an additional broad absorption peak and a further positive peak at higher probe energies. Due to its position, we straightforwardly assign the positive peak to bleaching of the C exciton and label it C^0. The absorption peak shows a formation similar to A^- and B^- (see next paragraph), and is similarly long lived, hence it should belong to a charge population. Like the C exciton bleaching, it is absent in cw PM, and strongly reduced for excitation energies below the C exciton resonance, see (Fig 3f), hence we ascribe it to a charge associated with the C exciton, labeled C^-. The C exciton is ascribed either to excitation from a band below the valence band, or between the valence and conduction bands in a region of the bands nesting slightly off the Γ point [42]. In both scenarios it is plausible that the C^0 and C^- feature do not appear in the cw experiment, which probes populations that have relaxed towards the edges of the band gap.

During the first 3 ps the $\Delta T/T$ spectrum undergoes a characteristic change of shape: the positive signal components are formed during the instrumental resolution and decay monotonically, while the main photoinduced absorption features, associated to charges A^-, B^- and C^-, show an initial instrument-limited rise followed by a delayed rise component after the pump pulse and by a slower decay. We can interpret this dynamics by assuming that the pump pulse creates an ensemble of excitons and charges with a combined spectrum $S_1(E)$.

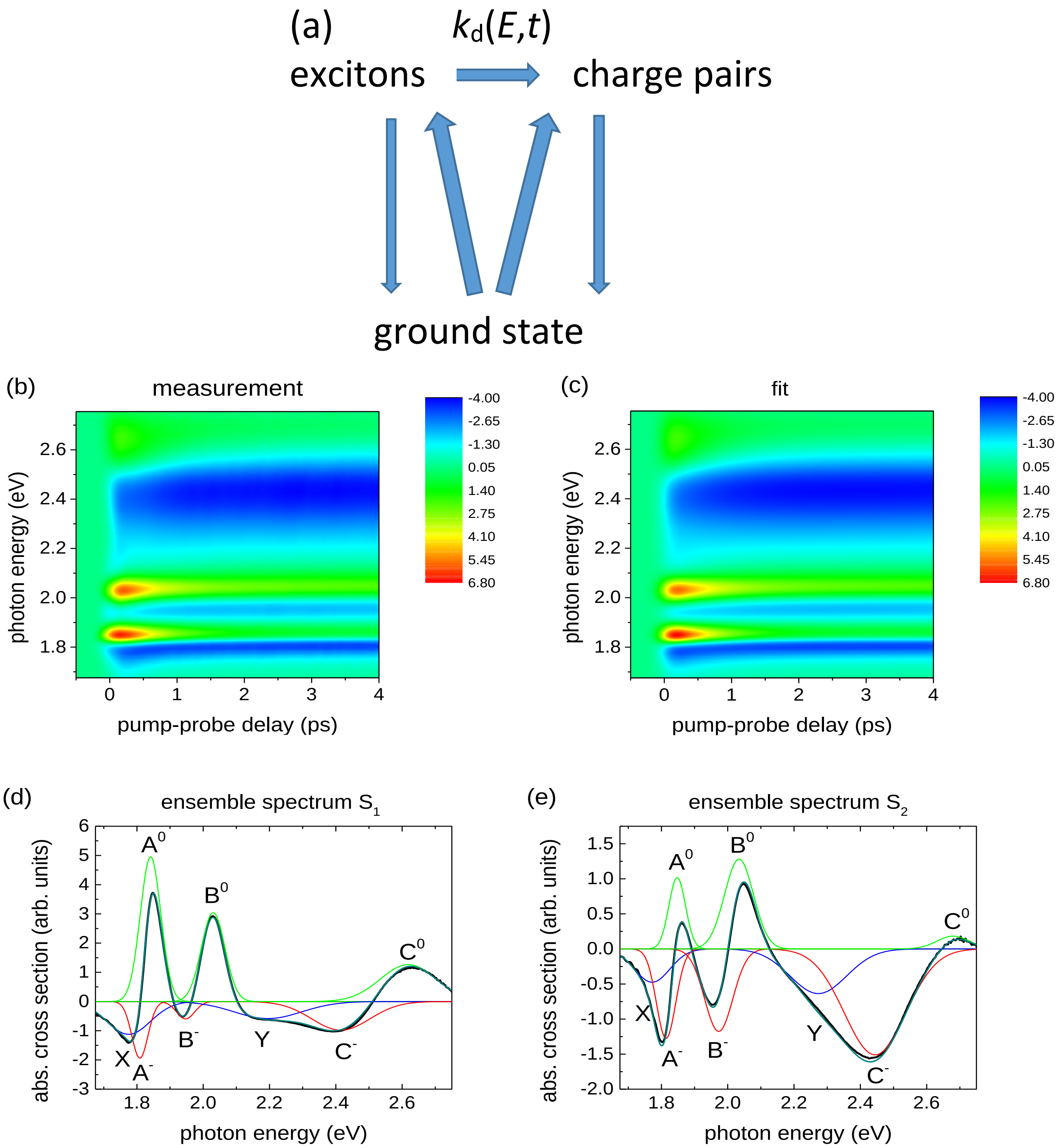

Figure 4: (a) Scheme of the photoexcitation dynamics of excitons and charges. (b) contour plot of the fitted $\Delta T/T$ (in %) (c) contour plot of the measured $\Delta T/T$ (in %) (d) spectrum S_1 described in the text (black) and fit to eight Gaussian peaks (photoinduced absorption from charges: red, photoinduced absorption from

excitons: blue, photobleaching: green) and their sum (dark cyan) (e) spectrum S_2 described in the text with the same color coding as (d).

During the first 3 ps, this ensemble evolves into one with less excitons and more charges, with a combined spectrum $S_2(E)$. Subsequently, the exciton and charge populations decay with very little further change of shape, meaning that either the decay times of excitons and charges are very similar (either by coincidence or due an interdependent relaxation mechanism), or that the population after 3 ps is already dominated by charges. The latter hypothesis is corroborated by the similarity between the fs $\Delta T/T$ spectrum at longer delays and the cw PM spectrum, which should not show any exciton contribution. In the simplest possible case, the ensemble with the spectrum $S_1(E)$ evolves into the one with the spectrum $S_2(E)$ with only one characteristic sub-picosecond relaxation time τ_1. Hence we propose the simple scheme of the underlying photoexcitation dynamics shown in Fig. 4a: The pump pulse generates a mixed population of charge carriers and excitons. Subsequently a certain fraction of the excitons dissociates into charges.

The evolution of the photoexcited states' population according to Fig. 4a is best fitted with a characteristic time $\tau_1 = 680$ fs. The assumption of only one common time constant τ_1 for the dissociation of the A, B, and C excitons may be a gross simplification, but it describes the data remarkably well (Figs 4b+c). The spectra S_1 and S_2 in Figs. 4d and e can be fitted with overlapping Gaussians analogously to the cw PM spectrum. Besides the six already identified charge absorption and exciton bleaching features, there are two additional peaks, which we label X and Y. Since they do not show the delayed formation characteristic of charges, we assign them to photoinduced absorption by one of the exciton populations.

Comparing the relative contributions of the X and Y peaks to the S_1 and S_2 spectra, we can deduce that after 3 ps approximately the exciton population is somewhat decreased (by approximately a factor of 2). On the other hand, if the exciton population followed a curve ~ $exp(-t/\tau_1)$, the remaining exciton population would be only 1%. Hence, τ_1 is not the time constant of the exciton dissociation, but rather the characteristic time with which the dissociation rate diminishes. Besides its time dependent rate, the exciton dissociation yield depends also on the energy of the exciting photons. This is expressed in Fig. 4a as a rate constant $k_d(E, t)$ that depends on the pump energy and on time. Fig 3f shows that the ratio between the absorption peaks due to charges and the respective bleaching peaks is higher for higher photon energy. This is consistent with the lower PL quantum yield for higher excitation energy, which has also been ascribed to charge separation [42].

Detailed studies of the CPG dynamics exist for carbon nanotubes and conjugated polymers, which are materials with exciton binding energies similar to MoS_2. In carbon nanotubes, there is an initial branching between mostly excitons and 1-2% directly excited charges [36], with a higher charge yield for higher excitation energy. In conjugated polymers, there is a similar initial branching, followed by additional CPG via dissociation of "hot" excitons during the first few picoseconds [43]. Elaborate models describe how the surplus energy of hot excitons increases their dissociation probability [44], [45]. The relaxation of the electron and hole to the lowest exciton state are typically faster than our observed 680 fs [46-48], however electron-phonon coupling creates a phonon heat bath that can live on for a few ps [49]. Additionally, exciton migration, which is facilitated by the extra energy and comes to a halt when the exciton reaches a local energy minimum, increases the probability that the exciton reaches a site where its dissociation is facilitated. In MoS_2 flakes, such sites could be surface defects, flake edges, metallic inclusions, crystal faults or small islands of an extra MoS_2 layer. We therefore conclude that the exciton dissociation probability is high while the excitons are hot and mobile and decreases as they reach their energetic minima. CPG in few-layer MoS_2 is a combination of two processes, both which have increased efficiency for higher exciting photon energy: direct excitation of charge pairs (within the 50-100 fs instrument resolution of our experiment) and hot exciton dissociation.

Before we discuss the implications of time- and pump energy dependent hot exciton dissociation, we review how our findings compare to previous femtosecond work on TMDs. Intervalley scattering [50], [51] requires circular polarization and is not probed in our experiment, because all our laser polarizations are linear. On a time scale of 1 ps to 500 ps, Shi et al. obtained results very similar to ours in few layer flakes deposited on a dielectric substrate [30], but they do not discuss the temporal change of shape of the spectrum, which is crucial in understanding exciton dissociation and charge generation. They estimate that for excitation fluences similar to ours, the sample temperature should change by only 0.1 K, thus dismissing sample heating as a possible source of the signal. In our samples, due to the low heat conductivity of PMMA [52], heating could be a bit stronger. However, a signal due to heating would not change its shape with time and, most crucially, its shape would not depend on the excitation photon energy. In Fig 3f, there is a small C^- signal even for excitation below the C exciton resonance. This contribution, which at any delay is 20% or less compared to the spectrum for excitation above the C resonance, may originate from heating or any other mechanism that changes the overall lineshapes and/or peak positions, such as Stark effect or band gap renormalization. Hence, for the combination of all such processes including heating, we estimate an upper boundary of 20% contribution. Any such mechanism is less important in the cw PM experiment, where no appreciable C^- signal is found. Therefore, both the femtosecond and the cw signals are dominated by changes in excited and ground state populations, not pure lineshape/shift mechanisms.

Considering further lineshape/shift mechanisms, inter-exciton interaction is expected to result in a red-shift [37] and line broadening. However, we observe an apparent line narrowing (see discussion of the cw PM spectrum) due to the increase of the central A^- peak at the expense of its neighbors on either side. The Burrstein-Moss effect, which has been observed in substitutionally doped MoS_2 fullerenes [53] should lead to a blue shift with increasing excited state population. Our contrasting observation implies that any Burrstein-Moss contribution is overwhelmed by one or more red-shifting mechanisms.

3 Conclusion and Outlook

We have shown that charge carrier photogeneration in few layer MoS_2 arises from two different processes. First, there is a branching into excitons and charge carriers as the primary photoexcited species. Additionally, there is an increased, excitation energy dependent charge carrier yield from hot exciton dissociation during the first few ps. For monolayer MoS_2, due to the higher exciton binding energy [14], we can expect both CPG processes to have a lower yield. According to our findings, the efficiency of MoS_2 photovoltaic [17] and photodetector [18] devices depends significantly on the excitation wavelength and can be strongly increased, especially in monolayer devices, by facilitating exciton dissociation, e. g. via a strong built-in field using appropriate electrode materials, by engineering a p-n junction [54], [55] , or by combining MoS_2 with a second material [56-58] so one of them acts as electron donor and the other as acceptor in a heterojunction.

References:

[1] Coleman, J. N. *et al.* Two-Dimensional Nanosheets Produced by Liquid Exfoliation of Layered Materials. *Science* 331, 568–571, 2011.

[2] Nicolosi, V.; Chhowalla, M.; Kanatzidis, M. G.; Strano, M. S.;Coleman, J. N. Liquid Exfoliation of Layered Materials. *Science* 340, 1420, 2013.

[3] Wang, Q. H.; Kalantar-Zadeh, K.; Kis, A.; Coleman, J. N.; Strano, M. S. Electronics and optoelectronics of two-dimensional transition metal dichalcogenides. *Nature Nanotech.* 7, 699-712, 2012.

[4] Butler, S. Z. *et al. ACS Nano* 7, 2898-2926, 2013.

[5] Sipos, B.; Kusmartseva, A. F.; Akrap, A.; Berger, H.; Forro, L.; Tutis, E. From Mott state to superconductivity in 1T-TaS_2. *Nature Mater.* 7, 960-965, 2008.

[6] Thomson, R.; Burk, B.; Zettl., A.; Clarke, J. Scanning tunneling microscopy of the charge-density-wave structure in 1T-TaS_2. *Phys. Rev. B* 49, 16899–16916, 1994.

[7] Stojchevska, L.; Vaskivskyi, I.; Mertelj, T.; Kusar, P.; Svetin, D.; Brazovskii, S.; Mihailovic, D. Ultrafast Switching to a Stable Hidden Quantum State in an Electronic Crystal. *Science* 344, 177-180, 2014.

[8] Radisavljevic, B.; Radenovic, A.; Brivio, J.; Giacometti, V.; Kis, A. Single-layer MoS_2 transistors. *Nature Nanotech.* 6, 147–150, 2011.

[9] Radisavljevic, B.; Whitwick, M. B.; Kis, A. Integrated circuits and logic operations based on single-layer MoS_2. *ACS Nano* 5, 9934–9938, 2011.

[10] Frindt, R. F.; Yoffe A. D. Physical Properties of Layer Structures: Optical Properties and Photoconductivity of Thin Crystals of Molybdenum Disulphide. *Proc. Roy. Soc. A* 273, 69-83, 1962.

[11] Mak, K. F.; Lee, C.; Hone, J.; Shan, J.; Heinz, T. F. Atomically thin MoS_2: a new direct-gap semiconductor. *Phys. Rev. Lett.* 105, 136805, 2010.

[12] Splendiani, A.; Sun, L.; Zhang, Y.; Li, T.; Kim, J.; Chim, C.-Y.; Galli, G.; Wang, F. Emerging photoluminescence in monolayer MoS_2. *Nano Lett.* 10, 1271–1275, 2010.

[13] Evans, B. L.; Young, P. A. Exciton spectra in thin crystals: the diamagnetic effect. *Proc. Phys. Soc.* 91, 475-482, 1967.

[14] Ramasubramaniam, A. Large excitonic effects in monolayers of molybdenum and tungsten dichalcogenides. *Phys. Rev. B* 86, 115409, 2012.

[15] Cheiwchanchamnangij, T.; Lambrecht, W. R. L. Quasiparticle band structure calculation of monolayer, bilayer, and bulk MoS_2. *Phys. Rev. B* 85, 205302-1-4, 2012.

[16] Ye, Z.; Cao, T.; O'Brien, K.; Zhu, H.; Yin, X.; Wang, Y.; Louie, S. G.; Zhang, X. Probing excitonic dark states in single-layer tungsten disulphide. *Nature* 513, 214-218, 2014.

[17] Fontana, M.; Deppe, T.; Boyd, A. K.; Rinzan, M.; Liu, A. Y.; Paranjape, M.; Barbara, P. Electron Hole Transport and Photovoltaic Effect in Gated MoS2 Schottky Junctions. *Sci.Rep.* 3, 1634, 2013.

[18] Lopez-Sanchez, O.; Lembke, D.; Kayci, M.; Radenovic, A.; Kis, A. Ultrasensitive Photodetectors Based on Monolayer MoS_2. *Nat. Nanotechnol.* 8, 497–501, 2013.

[19] Mak, K. F.; He, K.; Lee, C.; Lee, G. H.; Hone, J.; Heinz, T. F.; Shan, J. Tightly Bound Trions in Monolayer MoS2. *Nat. Mater.* 12, 207–211, 2012.

[20] Mouri, S.; Miyauchi, Y.; Matsuda, K. Tunable Photoluminescence of Monolayer MoS2 via Chemical Doping *Nano Lett.* 13, 5944-5948, 2013.

[21] Scheuschner, N.; Ochedowski, O.; Kaulitz, A. M.; Gillen, R.; Schleberger, M., Maultzsch, J. Photoluminescence of freestanding single- and few-layer MoS_2. *Phys. Rev. B* 89, 125406, 2014.

[22] Dean, N.; Petersen, J. C.; Fausti, D.; Tobey, R. I.; Kaiser, S.; Gasparov, L. V.; Berger, H.; Cavalleri, A.; Polaronic Conductivity in the Photoinduced Phase of 1*T*-TaS_2. *Phys. Rev. Lett.* 106, 016401, 2011.

[23] Osterbacka, R.; An, C.; Jiang, X.; Vardeny, Z. Two-Dimensional Electronic Excitations in Self-Assembled Conjugated Polymer Nanocrystals. *Science* 287, 839−842, 2000.

[24] Klimov, V. I.; Ivanov, S. A.; Nanda, J.; Achermann, M.; Bezel, I.; McGuire, J. A.; Piryatinski, A. Single-exciton optical gain in semiconductor nanocrystals *Nature* 447, 441−446, 2007.

[25] Cabanillas-Gonzalez, J.; Virgili, T.; Gambetta, A.; Lanzani, G.; Anthopoulos, T. D.; de Leeuw, D. M. *Phys. Rev. Lett.* 96, 106601, 2006.

[26] Gadermaier, C.; Menna, E.; Meneghetti, M.; Kennedy, W. J.; Vardeny, Z. V.; Lanzani, G. Long-Lived Charged States in Single-Walled Carbon Nanotubes. *Nano Lett.* 6, 301−305, 2006.

[27] Gatensby, R.; McEvoy, N.; Lee, K.; Hallam, T.; Berner, N. C.; Rezvani, E.; Winter, S.; O'Brian, M.; Duesberg, G. S. Controlled synthesis of transition metal dichalcogenide thin films for electronic applications. *Appl. Surf. Sci.* 297, 139-146, 2014.

[28] Lee, C.; Yan, H.; Brus, L. E.; Heinz, T. F.; Hone, J.; Ryu, S.; Anomalous Lattice Vibrations of Single- and Few-layer MoS_2. *ACS Nano* 4, 2695-2700, 2010.

[29] Li, H.; Zhang, Q.; Yap, C. C. R.; Tay, B. K.; Edwin, T. H. T.; Olivier, A.; Baillargeat, D.; From Bulk to Monolayer MoS_2: Evolution of Raman Scattering. *Adv. Funct. Mater.* 22, 1385-1390, 2012.

[30] Shi, H.; Yan, R.; Bertolazzi, S.; Brivio J.; Bao, G.; Kis, A.; Jena, D., Xing, H. G.; Huang, L. Exciton Dynamics in Suspended Monolayer and Few-Layer MoS_2 2D Crystals. *ACS Nano* 7, 1072-1080, 2013.

[31] Mai, C.; Barrette, A.; Yu, Y.; Semenov, Yu. G., Kim, K. W.; Cao, L.; Gundogdu, K. Many-Body Effects in Valleytronics: Direct Measurement of Valley Lifetimes in Single-Layer MoS_2. *Nano Lett.* 14, 202-206, 2014.

[32] Sercombe, D., Schwarz, S., Del Pozo-Zamudio, O.; Liu, F.; Robinson, B. J.; Chekhovich, E. A.; Tartakovskii, I. I.; Kolosov, O.; Tartakovskii, A. I. Optical investigation of the natural electron doping in thin MoS_2 films deposited on dielectric substrates. *Sci. Rep.* 3, 3489, 2013.

[33] Plechinger, G.; Schrettenbrunner, F.-X.; Eroms, J.; Weiss, D.; Schuller, C.; Korn, T. Low-temperature photoluminescence of oxide-covered single-layer MoS_2. *Phys. Stat. Sol. RRL* 6, 126-128, 2012.

[34] Gutierrez, H. R. et al. Extraordinary Room-Temperature Photoluminescence in Triangular WS_2 Monolayers. *Nano Lett.* 13, 3447-3454, 2013.

[35] Yadgarov, L.; Choi, C. L.; Sedova, A.; Cohen, A.; Rosentsveig, R.; Bar-Elli, O.; Oron, D., Dai, H.; Tenne, R. Dependence of the Absorption and Optical Surface Plasmon Scattering of MoS_2 Nanoparticles on Aspect Ratio, Size, and Media. *ACS Nano* 8, 3575-3583, 2014.

[36] Soavi, G.; Scotognella, F.; Brida, D.; Hefner, T.; Späth, F.; Antognazza, M. R.; Hertel, T.; Lanzani, G.; Cerullo, G. Ultrafast Charge Photogeneration in Semiconducting Carbon Nanotubes. *J. Phys. Chem. C* 117, 10849-10855, 2013.

[37] Sim, S.; Park, J.; Song, J.-G.; In, C.; Lee, Y.-S.; Kim, H.; Choi, H. Exciton dynamics in atomically thin MoS_2: Interexcitonic interaction and broadening kinetics. *Phys. Rev. B* 88, 075434-1-5, 2013.

[38] Tränkle, G.; Lach, E.; Forchel, A.; Scholz, F.; Ell, C.; Haug, H.; Weimann, G.; Griffiths, G.; Kroemer, H.; Subbanna, S. General Relation between Band-Gap Renormalization and Carrier Density in Two-Dimensional Electron-Hole Plasmas. *Phys. Rev. B* 36, 6712-6714, 1987.

[39] Wang, Q.; Ge, S.; Li, X.; Qiu, J.; Ji, Y.; Feng, J.; Sun, D. Valley Carrier Dynamics in Monolayer Molybdenum Disulfide from Helicity-Resolved Ultrafast Pump-Probe Spectroscopy. *ACS Nano* 7, 11087-11093, 2013.

[40] Ugeda, M. M. et al. Giant bandgap renormalization and excitonic effects in a monolayer transition metal dichalcogenide semiconductor. *Nature Mater.* advance online publication.

[41] Ouyang, Q. Y.; Yu, H. L.; Zhang, K.; Chen, Y. J. Saturable absorption and the changeover from saturable absorption to reverse saturable absorption of MoS_2 nanoflake array films. *J. Mater Chem C* 2, 6319-25, 2014.

[42] Kozawa, D. et al. Photocarrier relaxation pathway in two-dimensional semiconducting transition metal dichalcogenides. *Nature Commun.* 5, 4543-1-5, 2014.

[43] Gadermaier, C.; Cerullo, G.; Sansone, G.; Leising, G.; Scherf, U.; Lanzani, G. Time-Resolved Charge Carrier Generation from Higher Lying Excited States in Conjugated Polymers. *Phys. Rev. Lett.* 89, 117402, 2002.

[44] Noolandi, J.; Hong, K. M. Theory of photogeneration and fluorescence quenching. *J. Chem. Phys.* 70 3230-3236, 1979.

[45] Arkhipov, V. I., Emilianova, E. V., Bassler, H. Hot exciton dissociation in a conjugated polymer. *Phys. Rev. Lett.* 82, 1321-1324, 1999.

[46] Leitenstorfer, A.; Furst, C.; Laubereau, A.; Kaiser, W.; Trankle, G.; Weimann, G. Femtosecond carrier dynamics in GaAs far from equilibrium. *Phys. Rev. Lett.* 76, 1545-1548, 1996.

[47] Sun, D.; Wu, Z.-K.; Divin, C.; Li, X.; Berger, C.; de Heer, W. A.; First, P. N., Norris, T. B.; Ultrafast Relaxation of Excited Dirac Fermions in Epitaxial Graphene Using Optical Differential Transmission Spectroscopy. *Phys. Rev. Lett.* 101, 157402-1-4, 2008.

[48] Gadermaier, C. *et al.* Strain-Induced Enhancement of the Electron Energy Relaxation in Strongly Correlated Superconductors. *Phys. Rev. X* 4, 011056-1-6, 2014.

[49] Dhar, L.; Roger, J. A.; Nelson, K. A. Time-Resolved Vibrational Spectroscopy in the Impulsive Limit. *Chem. Rev.* 94, 157-193, 1994.

[50] Mai, C.; Barrette, A.; Yu, Y. F.; Semenov, Y. G.; Kim K. W.; Cao, L. Y.; Gudnogdu, K. Many-Body Effects in Valleytronics: Direct Measurement of Valley Lifetimes in Single-Layer MoS_2. *Nano Lett.* 14, 202-206, 2014.

[51] Lagarde, D.; Bouet, L.; Marie, X.; Zhu, C. R.; Liu, B. L.; Amand, T.; Tan, P. H.; Urabaszek, B. Carrier and Polarization Dynamics in Monolayer MoS_2. *Phys. Rev. Lett.* 114, 047401-1-4, 2014.

[52] Assael, M. J.; Botsios, S.; Gialou, J.; Metaxa, I. N. Thermal Conductivity of Polymethyl Methacrylate (PMMA) and Borosilicate Crown Glass BK7. *Int. J. Thermophys.* 26, 1595-1605, 2005.

[53] Sun, Q. C.; Yadgarov, L.; Rosentsveig, R.; Seifert, G.; Tenne, R.; Musfeldt, J. L.; Observation of a Burstein-Moss Shift in Rhenium-Doped MoS_2 Nanoparticles. *ACS Nano* 7, 3506-11, 2013.

[54] Pospischil, A.; Furchi, M. M.; Mueller, T. Solar-energy conversion and light emission in an atomic monolayer p-n diode. *Nature Nanotech* 9, 257-261, 2014.

[55] Bauger, B. W. H.; Churchill, H. O. H.; Yang, Y. F., Jarillo-Herrero, P. Optoelectronic devices based on electrically tunable p-n diodes in a monolayer dichalcogenide. *Nature Nanotech.* 9, 262-267, 2014.

[56] Britnell, L. *et al.* Strong Light-Matter Interactions in Heterostructures of Atomically Thin Films. *Science* 340, 1311-1314, 2013.

[57] Lee, C.-H. et al. Atomically thin p-n junctions with van der Waals heterointerfaces. *Nature Nanotech.* 9, 676-681, 2014.

[58] Hong, X.; Kim, J.; Shi, S.-F.; Zhang, Y.; Jin, C.; Sun, Y.; Tongay, S.; Wu, J.; Zhang, Y.; Wang, F. Ultrafast charge transfer in atomically thin MoS_2/WS_2 heterostructures. *Nature Nanotech.* 9, 682-686, 2014.

For wider interest

MoS_2 – layered semiconducting crystal, which consist of layers with strong in-plane chemical (covalent or ionic) bonds and relatively weak (van der Waals) adhesion between these layers. A single sheet of MoS_2 absorbs more than 5% of the incident light in the visible range. This means that an extremely small amount of material – deposited on a transparent electrode or blended into a transparent polymer – could be efficient for the fabrication of a low-cost, lightweight solar cell that can be applied to many irregular surfaces. Such versatility has so far been the reserve of organic photovoltaics, which is still struggling with photodegradation.

In order to find out how to use semiconducting TMDs for photovoltaics, we need to understand what goes on when they absorb light. Since the expected processes are very fast (occuring in less than a nanosecond or sometimes even less than a picosecond), we use ultrafast lasers to study them. In what we call pump-probe spectroscopy, a first laser pulse of approximately 100 fs duration excites the sample, creating a population of electrons and holes (electron vacancies) at a very well defined point in time, which marks the start for all relaxation processes occurring after excitation. A second, weaker but similarly short laser pulse probes the optical absorption of the sample at a defined point in time after the excitation, which is different for an excited sample compared to a sample in equilibrium. By varying the pump-probe delay we can follow the relaxation processes.

First results on prototype photovoltaic elements of monolayer MoS2 have indicated that their efficiency is limited by the strong interaction between the photoexcited electrons and holes, which hampers their extraction from the device. Here we show that in few-layer MoS2 flakes dispersed in tranparent plastic the separation of electrons and holes is very efficient (close to 100%) and occurs on a time scale of 700 fs. This result suggests that few-layer MoS2, which is even easier to obtain than monolayers, is actually more suitable for photovoltaics.

Non- destructive Analysis of Archaeological Metals

Helena Fajfar[1,2,3], **Zdravko Rupnik**[1], **Žiga Šmit**[1,4]
[1] Department of Low and Medium Energy Physics, Jožef Stefan Institute, Ljubljana, Slovenia
[2] Jožef Stefan International Postgraduate School, Ljubljana, Slovenia
[3] JUVI Domžale d.o.o., Domžale, Slovenia
[4] Faculty of Mathematics and Physics, University of Ljubljana, Ljubljana, Slovenia
helena.fajfar@ijs.si

Abstract. Ion beam analysis is an efficient method for studies of archaeological metals. It is based on excitation of characteristic X-rays and gamma rays. In this paper we present PIXE and PIGE analysis of different metal alloys. Spot analysis was used for analysis of bronzes, which were used for medieval early fiery weapons. In the second part of the paper, the inhomogeneous metal objects are examined. The external beam facility was improved for the mapping measurements, which allow detection of inhomogeneous gilded layers. The new system allows the external beam to be scanned over an area of a few cm^2.

Keywords: PIXE, PIGE, metals, mapping

1 Introduction

Archaeological metals are important testimony of human past. Material identification is basic objective of scientific characterization of ancient objects and provides important clues about fabrication. Elemental analysis of metals provides valuable information about the composition of alloys and may lead to identifying the metal origin. Analytical data on metal composition may also provide interesting insight into past technologies, including mining, melting and metal working [1]. When a unique artefact is found, the analytical methods are required of being non-destructive and able to give the chemical analysis without sampling. PIXE and PIGE methods allow us detection of major, minor and trace elements. An advantage of PIXE compared to other IBA methods is its speed and sensitivity.

Up to now only spot analysis was used in our studies of archaeological metals [2, 3]. In the present paper we report about further development of the method applied on historical metals. The spot analysis was used to measure medieval bronzes of early weapons. Recent development includes application of mapping, using an in-air beam. The new mapping system allows us to provide elemental concentration maps from the PIXE spectra. As an example of metal inhomogeneous composition we studied the structure of a bronze-iron alloy known as aes rude. From the map of a gilded medieval fragment it is possible to identify the metal plating technique.

2 Experimental

The 2 MV particle accelerator at the Microanalytical Center of the Jožef Stefan Institute is equipped with four measuring lines. One line allows measurements with in-air proton beam. The method of Proton Induced X-ray Emission (PIXE) and Particle Induced Gamma-ray Emission (PIGE) were used. PIXE is a non-destructive analytical method. The characteristic X-rays are emitted while filling the inner shell vacancies created by proton bombardment. The respective X-rays intensities are directly related to the concentrations of the corresponding elements. PIXE is used for elements with Z>12. For light elements we used gamma rays, because with PIGE we can see deeper below surface. The nominal energy of protons in our measurements was 3 MeV. The beam intensity was a few nA and the counting rate was below 500 cps. The beam was extracted into air through a 2 μm thick tantalum foil. The induced X-ray passed through a 6.0 cm air gap between the target and a Si(Li) detector. The beam profile at the target was Gaussian, with 0.8 mm full width at half maximum. For spot analysis, three spectra were taken in a particular measuring point. The measurement in air provided X-rays of the elements heavier than silicon. For hard X-rays around silver, a 0.3 mm thick aluminum absorber was used. After measuring with the aluminum absorber we repeated the measurement using a selective filter of cobalt, which provided better sensitivity for iron and nickel. The measuring time for one sample was around 7 minutes. The spectra were fitted using the AXIL software package.

The new system for mapping allows the external beam to be scanned over an area of a few cm^2. The sample is fixed on a remote controlled stage driven by high precision stepping motors. After selecting the area of interest of the sample and setting the scanning conditions, the measurement can start. During the scanning process, the measurement process is executed through the following steps: moving the sample to the selected position, acquiring the data, saving the spectra and finally moving the sample to the next position. After measurements the PIXE spectra were processed with the AXIL program and the elemental concentrations were calculated by the program [4]. The elemental maps were performed on the most typical elements for metals and were built up by program ORIGIN 8.0. The images were composed of 10 x 7 points and 10 x 20 points, so the scanned area measured 10 mm x 7 mm and 1 cm x 2 cm. The accuracy of the procedure was within 5% for major elements, about 10% for the elements with concentrations below 1%, and about 15% for trace elements.

3 Results

3.1 Medieval bronzes for weapons

Medieval weaponry spanned a range from simple tools and farm implements to sophisticated siege engines. Europeans certainly had firearms by the first half of the 1300s. In army different kind of weapons were used. One of them was called handgonne or hand cannon. The hand cannon was a simple weapon, effectively consisting of a barrel with some sort of handle, and it came in different shapes and sizes. It was constructed of metal and attached to some kind of stock, usually wooden. Due to the poor quality of powder that was often used in these weapons and their crude construction, they were not effective missile weapons, as early examples often lacked sufficient power to punch through light armor [5, 6].

Three different fragments of handgonnes were measured (Table 1). They were all found in south Slovenia in the vicinity of castle ruins [7]. The tin concentration in all samples was lower than 5%. With such a low concentration of tin the alloys remains tough, i.e. not too hard and not too fragile. Samples also contained antimony (0.87% - 2.66%) and arsenic (0.61% - 2.20%), so we can conclude that the copper was extracted from polymetallic ores tennantite and tetrahedrite ($(\mathrm{(Cu,Fe)_{12}Sb_4S_{13}})$). The sample no. 1 (Fig. 1) contained 9.46% Pb. Lead has the effect of making the alloys of copper easier to cast. Such a high concentration (sample no.1) improved the fluidity of the alloy in the melt, but reduced the mechanical strength of the metal. In sample no. 2 we detected 1.71% Pb. It is generally accepted that such a small concentration is impurity in the raw materials and has not been added intentionally. The highest concentration of zinc was in the sample no. 3 (4.63%) and the lowest in sample no. 1 (0.71%). We believe that there were different reasons for the explosion of handgonnes. For sample no. 1 and 2 it was certainly the quality of material. No. 1 contains only about 4% Sn, which in a pure Cu-Sn alloy would make the metal ductile, however, the presence of 2.66% antimony and 9.46% lead would render material with worse material properties, especially as such an amount of lead cannot dissolve in copper but forms distinct globules. According to their composition, bronzes no. 1 and 2 are quite similar to the alloys used in Late Bronze Age, so it is not impossible the material was collected from a prehistoric hoard. It is only no. 3 that contains about 4-5% tin and zinc that qualify it as gunmetal. It was the use of improved gunpowder in granular form that turned out fatal for many early fiery weapons [5]. The bore in no. 3 is not cylindrical, but slightly spherical as an indication of being blown up. In this case the reason for explosion might not be material, but imprecise, non-centred boring.

Table 1: Analysis of three pieces of handgonnes (in mass %)

No./Location	**Caliber [mm]**	**Fe**	**Ni**	**Cu**	**Zn**	**As**	**Ag**	**Sn**	**Sb**	**Pb**
1. Čretež	25	0.15	0.37	82.0	0.71	0.61	0.14	3.95	2.66	9.46
2. Kostel	13	1.61	2.53	85.6	0.80	2.20	0.29	3.93	1.37	1.71
3. Šumberk	16	0.67	0.48	85.2	4.63	0.68	0.20	3.61	0.87	3.68

Figure 1: Fragments of three different handgonnes from south Slovenia.

3.2 Aes rude

The AES RUDE (raw bronze) indicates cast bronze used in Italy between the 8th and 4th centuries BC. In that time a pre-monetary system was valid in Italy, which featured bronze or copper ingots cast in a rough shape, which the Romans called aes. Different forms of these metals were found. The oldest specimens were just worked lumps of copper or bronze. Rome obtained inspiration from the ingot shape to establish its own currency system. It was called aes signatum [8, 9]. It was based on ingots made of cast copper or bronze and stamped on each side.

A sample of aes rude from Košana, Slovenia was measured and traces amounts of As, Zn, Mo and Pb were detected. Zinc and arsenic impurities are correlated with copper. We also found out that the molybdenum is correlated with iron. Aes rude is technologically useless, so the metal ingots that circulated among prehistoric settlements were either intended for further processing or they were just used for commercial exchange. The scanning area of the sample was 7 x 10 mm.

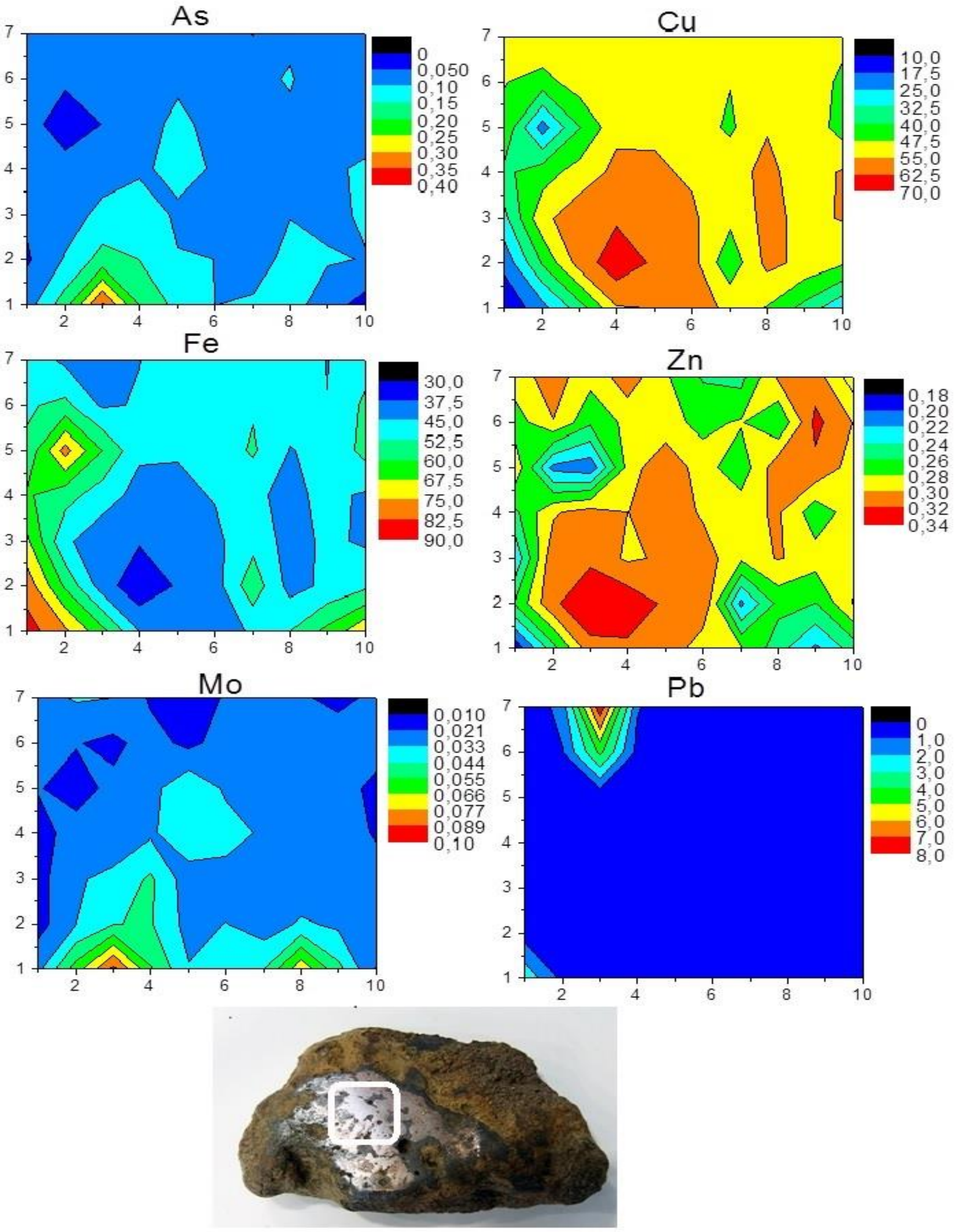

Figure 2: Elemental maps on the sample of aes rude. The scanning area was 10 mm x 7 mm. The color scale reflects weight %.

3.3 Gilded fragments

Gilding is application of gold to the surface of some other material. In Roman and medieval period the gilding techniques included the process of fire gilding, depletion gilding, application of golden leaves and dipping into molten gold [10, 11]. Fire gilding is also known as amalgamation gilding or mercury gilding [11-14]. This type of gilding was often used to gild small areas of the object, yet the gilding spread over the edge of the intended area. For this process small gold fragments were first dissolved in liquid mercury at a moderate temperature to obtain an amalgam, and that amalgam was applied onto the metal object which was then heated to a temperature higher than the mercury boiling point (356.5°C) in order to evaporate it. In practice, the objects to be gilded generally made of copper, bronze or brass were first coated and then heated with the amalgam decomposed. Amalgamation gilding was used extensively in the Roman and medieval period. The depletion gilding is a method for producing a layer of nearly pure gold on an object made of low-grade gold alloy by removing less noble metals from its surface. The surface was etched with acids, resulting in a surface of porous gold. The porous surface is then remelted, resulting in a shiny gold surface.

In Fig. 3, analysis of a medieval fragment from Kolovec, Slovenia (probably part of a cross, dating to 14th - 15th century and showing the scene of annunciation) is presented. High concentration of mercury in the range up to 11% indicates that the technique used was fire gilding. The object was made of copper (the lowest concentration was 30%). The correlated maps of gold and mercury confirm that the method of amalgamation was applied. The concentration of gold reached up to 55% at the surface. The silver content in this sample was low (< 1%). The silver is correlated with gold, which shows it was an admixture to gold before an amalgam was made.

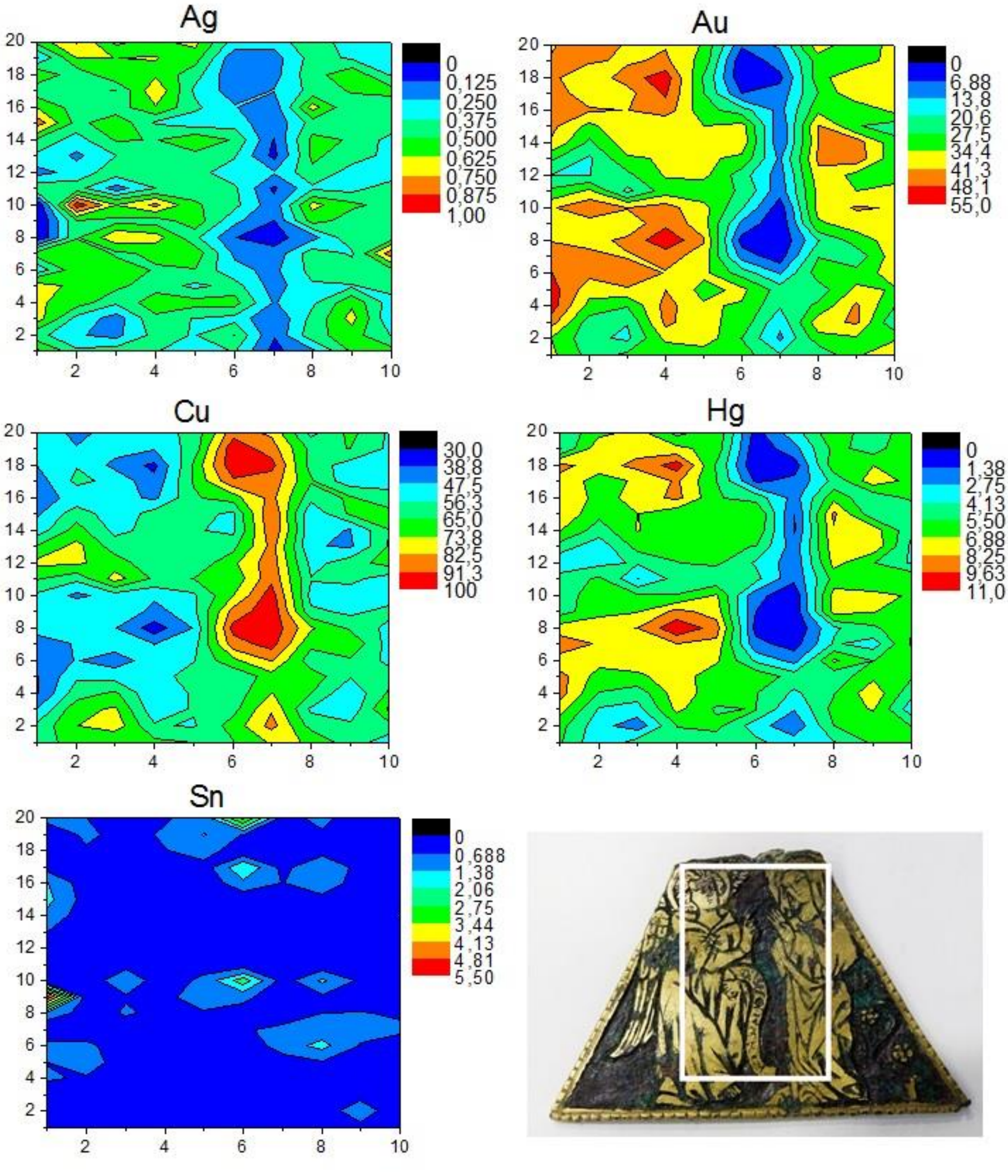

Figure 3: Elemental maps of the fragment of a cross showing the scene of Annunciation. The color scale is in weight %. The scanning area was 10 x 20 mm.

4 Conclusion

Ion beam analysis techniques were used to characterize metals of cultural heritage objects. With spot analysis three bronzes of medieval weapons were measured. They are of low quality, with large amounts of added impurities. More information about the sample composition can be obtained with mapping. Elemental mappings provide more information, because we investigate a large area of the sample. The correlated maps of gold and mercury on the fragment of medieval cross indicated that the method of amalgamation was applied.

References:

[1] M. F. Guerra, I. Tissot, The role of nuclear microprobes in the study of technology, provenance and corrosion of cultural heritage: The case of gold and silver items, *Nucl. Instr. Meth.* B 306: 227-251, 2013.

[2] Ž. Šmit, J. Istenič, V. Gerdun, Z. Milić and A. Mladenović, Archaeometric analysis of Alesia group brooches from sites in Slovenia, *Arheološki vestnik* 56: 213-233, 2005.

[3] Ž. Šmit, J. Istenič and S. Perovšek, PIXE analysis of Late La Tėne scabbards with non-ferrous openwork plates (and associated swords) from Slovenia, *Arheološki vestnik,* 61: 165-173, 2010.

[4] Ž. Šmit, P. Pelicon, J. Simčič, J. Istenič, Metal analysis with PIXE: The case of Roman military equipment, *Nucl. Instr. Meth. B* 239: 94-99, 2005.

[5] I. V. Hogg, The story of the gun, New York, 1996.

[6] *http://www.handgonne.com*, [access, December 2014].

[7] Ž. Šmit, Strelna cev, *Vojnozgodovinski zbornik* 28, 2007.

[8] E. A. Sydenham, Aes Grave, a Study of the Cast Coinages of Rome and Central Italy, London, 1926.

[9] *http://www.nbbmuseum.be,* [access, December 2014].

[10] Ž. Šmit, J. Istenič, T. Knific, Plating of archaeological metallic objects – studies by differential PIXE, *Nucl. Instr. Meth.* B 266: 2329-2333, 2008.

[11] S. L. Niece, in Metal Plating and Patination, Butterworth-Heinemann, 1993.

[12] K.N. Lechtman, Ancient methods of gilding silver: examples from the old and new worlds, In *Science and Archaeology, Cambridge,* 1971.

[13] T. Trojek, M. Hložek, X-ray fluorescence analysis of archaeological finds and art objects: Recognizing gold and gilding, *Applied Radiation and Isotopes,* Vol. 70: 1420-1423, 2012.

[14] V. Corregidor, L.C. Alves, N.P. Barradas, M.A. Reis, M.T. Marques, J.A. Ribeiro, Characterization of mercury gilding art objects by external proton beam, *Nucl. Instr. Meth.* B 269: 3049-3053, 2011.

For wider interest

Material identification is basic objective of scientific characterization of ancient objects and provides important clues about fabrication. The chemical composition of ancient objects is important for their authentication. The nature as well as the relative amounts of major, minor, and trace elements in any object are useful for determining the authenticity and production details of ceramics, glass, or metal alloys. We can use different analytical methods for the determination of cultural heritage objects and objects of art. In our measurements we used only non-destructive techniques.

The measurements are executed at the Tandetron accelerator, using proton beam in-air, so the analysis is generally done without sampling. Our methods are X-ray and gamma ray spectroscopy. Particle-induced X-ray emission (PIXE) and Particle-induced gamma-ray emission (PIGE) are non-destructive spectroscopic methods for analyzing different materials, especially useful for archaeological objects. This is a good choice if the chemical composition of an unknown substance is to be determined quickly. Liquid, solid and powdered samples can be analyzed. Soft X rays are absorbed in the air gap between target and detector. For this reason, PIXE is useless for soft element analysis. For light elements we measure gamma yields rather than X- rays. With PIGE we can analyze deeper below surface. The elements emit gamma photons after the collisions with protons. Photon energies vary between 100 keV and 2 MeV. Measuring the gamma spectra with PIGE, we obtain relative photon yields of light elements with respect to the standard. The X-ray and gamma ray data are then recalculated into concentrations simultaneously, estimating the matrix effects by an iterative procedure.

Up to now only spot analysis was used in our studies of archaeological metals. The new system for mapping allows the external beam to be scanned over an area of a few cm^2. The sample is fixed on a remote controlled stage driven by high precision stepping motors. The measurement starts with the selection of an area of interest and setting the initial conditions. The scanning process is based on the following cycles: moving the sample, data acquisition, saving the spectra, and moving to the next measuring point. Elemental mappings provide more information, because we investigate a large area of the sample.

Solution-derived Ta_2O_5 high-*K* thin films for gate dielectric applications

Raluca C. Frunză[1,2], Pedro Barquinha[3], Hermine Stroescu[4], Măriuca Gartner[4], Barbara Malič[1]

[1] Jožef Stefan Institute, Ljubljana, Slovenia

[2] Jožef Stefan International Postgraduate School, Ljubljana, Slovenia

[3] CENIMAT-I3N, Departament of Material Science and CEMOP/UNINOVA, Faculty of Science and Technology, Caparica, Portugal

[4] Ilie Murgulescu Institute of Physical Chemistry of the Romanian Academy, Bucharest, Romania

raluca.frunza@ijs.si

Abstract. Ta_2O_5 is a promising high-*K* dielectric, due to its high refractive index, high dielectric permittivity (in the range 22-28 for the amorphous state) and good thermal and chemical stability. The present study reports the preparation of solution-derived Ta_2O_5 thin films processed at low temperatures suitable for applications in transparent electronics. The investigated thin films exhibited promising properties for capacitors and thin-film transistors.

Keywords: Ta_2O_5, amorphous high-*K* dielectrics, sol-gel chemistry

1 Introduction

Transparent electronics emerges as a promising technology distinct from the conventional silicon one, and its viability depends on the performance, reliability and cost of both passive and active electronic applications. A lot of effort has been put in the research and development of transparent thin-film transistors (TFTs), which are mainly used as on-off switches in active matrix backplanes of flat panel displays. Their main components are a semiconductor layer, three electrodes, *i.e.*, gate, source and drain, and a dielectric layer between the gate and the semiconductor, also referred to as the gate dielectric. All of them are deposited in the form of thin films onto an insulator substrate. A TFT is a special type of field-effect transistor and its

working principle relies on the modulation of the current flowing in the semiconductor.
The development of transparent TFTs requires among other also high-quality amorphous high-*K* dielectrics processed at low temperatures, and tantalum-pentoxide thin films are of great interest.

The Ta_2O_5-based thin films presented herein were deposited from solution on selected substrates and were processed at temperatures not exceeding 400 °C. The influence of the processing temperature upon the structural and electrical properties of films was investigated. Their functionality was tested in passive and active electronic devices, namely thin film capacitors and TFTs.

2 Experimental details

The precursor was prepared by alkoxide-based sol gel synthesis. Further details on solution preparation and processing can be found elsewhere [1]. Thin films were deposited on platinized silicon ($Pt/TiO_2/SiO_2/Si$ or shortly Pt/Si) substrates by spin coating. After each deposition, the films were heated in air on the hot plates at 150 °C for 2 minutes and at 250, 300, 350 or 400 °C for additional 2 minutes. Note that as a typical high-*K* material, tantalum pentoxide begins to crystallize at 600 °C and it is crystalline above 700 °C [2]. In this study, the samples were processed at low temperatures, in order to ensure their amorphous structure, which is generally preferred in TFTs [3].

For all samples, the spinning–heating procedure was repeated ten times. The sample thickness values (estimated from the FE-SEM analysis of the fracture surfaces) decreased considerably with the processing temperature, from about 190 nm to about 115 nm for the samples heated at 250 °C and 400 °C, respectively. This was related to the process of densification [4].

The Fourier-transform infrared (FT-IR) analyses were performed using a Perkin Elmer Spectrum 100 FT-IR spectrometer. The transmittance data were collected in the range 4000-380 cm^{-1}, in the Attenuated Total Reflectance (ATR) mode. The spectrum of a bare Pt/Si substrate was measured as the background. All spectra were baseline corrected.

The samples were investigated by spectroscopic ellipsometry using a UV-Vis Variable Angle Spectroscopic Ellipsometer (VASE) with rotating analyzer from J.A. WOOLLAM. The experimental spectra were modelled as multi-layer structures given on the used substrate, rendering good agreement with the experimental data.

The surface morphology of the samples was analysed by an Asylum Research Molecular Force Probe 3D (MFP-3D-S™) atomic force microscope.

Au electrodes of 0.4 mm diameter were sputtered on top of the Pt/Si samples. Capacitance and loss factor, tan δ, were measured at room temperature with a driving signal of 50 mV, using a HP 4284A impedance analyzer. The relative permittivity values, ε, were calculated at the frequency of 100 kHz. The current–voltage characteristics were measured using a Keithley 2602A system sourcemeter and a HP 16058A test fixture combined setup. More details and comprehensive results are given in previous reports [1, 5].

Solution derived Ta_2O_5 dielectric thin films processed at 300 and 350 °C, of ≥ 250 nm, were used to fabricate TFTs with sputtered gallium indium zinc oxide (GIZO) channel layer [6]. The TFTs on Corning Eagle glass substrates had a width-to-length ratio (W/L) of 45 μm / 90 μm.

3 Results and discussion

To investigate the effect of the processing temperature on the chemical composition of the films deposited on Pt/Si, a FT-IR analysis was employed. The broad bands located below 1000 cm^{-1} are assigned to vibrations of Ta–O bonds [7, 8]. As expected, the bands that could be ascribed to residual functional groups became less distinct when increasing the heating temperature from 250 °C to 400 °C (see Fig. 1(a)). The band at 1100 cm^{-1}, which is presumably due to an overlapping of several vibrations belonging to residual organics, *i.e.*, to the C–C and C–O bending modes [7], was eliminated as some organics were decomposed upon heating at temperatures above 300 °C. Also, the signal of the modes due to the deformation of C–H (*i.e.*, at 1450 cm^{-1} and 1380 cm^{-1} in the case of the film processed at 250 °C) decreased with the processing temperature. The 350 °C sample showed an overlapped broader peak with a minimum at 1420 cm^{-1}, which was no longer visible in the spectrum of the sample heated at 400 °C. Even though the band at about 1600 cm^{-1}, presumably corresponding to the modes of adsorbed water and amino groups, was present in the spectra recorded for all the samples, its intensity decreased with the processing temperature. In addition, a shift towards lower wavenumbers from 1645 cm^{-1} to 1620 cm^{-1} for the samples heated at 250 °C and 400 °C, respectively, was observed. The broad band ranging up to 3600 cm^{-1}, with the minimum around 3200 cm^{-1}, corresponding to the stretching vibrations of water and hydroxyl groups (O−H) [7], could be assigned to residual H_2O.

Thereby, in the case of the samples processed at 400 °C, the presence of residual organic groups could not be excluded, however they could be detected in a much smaller amount as compared to the samples processed at lower temperatures.

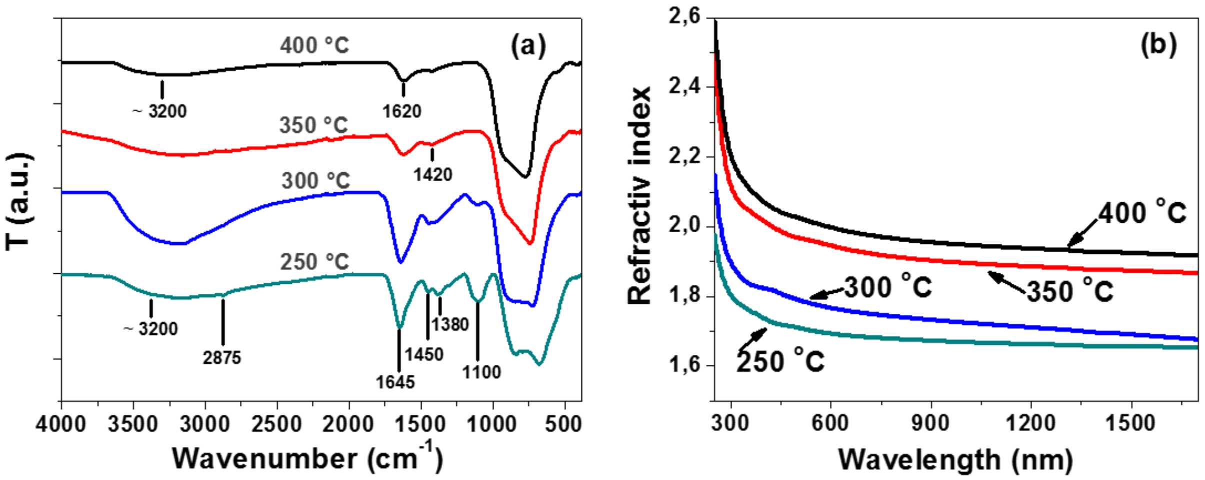

Figure 1: (a) FT-IR spectra of the Ta_2O_5 thin films prepared on Pt/Si and processed at the selected temperatures. (b) Refractive index dispersion of the thin films.

Spectroscopic ellipsometry measurements were also employed to determine the optical constants of the Ta_2O_5-based thin films. The determined refractive indices as a function of wavelength are given in Fig. 1(b). The refractive index increased with the processing temperature, in agreement with the consequent densification taking place at higher heating temperatures. The refractive index (at 600 nm) ranged from 1.7 to 1.99 for the samples processed at 250 °C and 400 °C, respectively. The Cauchy dispersion of the refractive index and its processing temperature dependence are in agreement with reports in the literature about solution-derived Ta_2O_5 thin films [3, 7, 9-11].

The surface morphology of the samples was characterized in terms of the root-mean-square (RMS) vertical roughness by AFM. The investigated thin films had uniform surface morphologies without any evident microstructural details, in agreement with their amorphous structure. The average vertical RMS surface roughness values were up to 0.3 nm. For a conclusive representation, the surface profiles were obtained from the topography images using an AFM software (*i.e.*, Igor Pro 6.34A). Typical AFM surface profiles are depicted in Fig. 2.

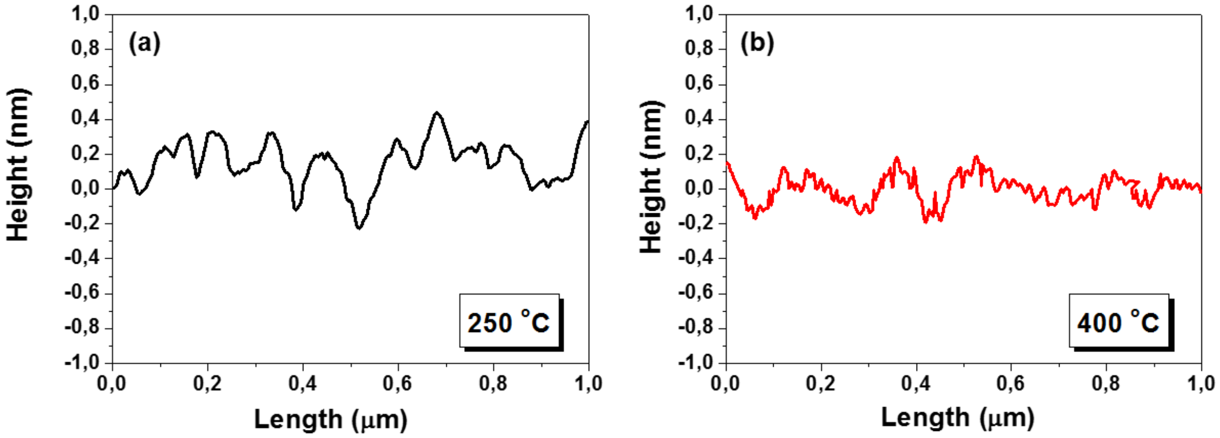

Figure 2: AFM surface profiles of the (a) 250 °C and (b) 400 °C samples.

These results are in agreement with other reports on chemical solution deposited thin films. In their study on Ta_2O_5 thin films prepared by metal-organic solution deposition technique, Joshi *et al.* [11] reported a smooth surface morphology of the films deposited on Pt/Si and no appreciable effect of the annealing temperature on their microstructure up to 600 °C.

The electrical properties of the metal-insulator-metal capacitors are given in Fig. 3. Amorphous Ta_2O_5 thin films have been reported to exhibit a relative dielectric permittivity in the range of 20 – 28 [2, 12]. In the current study, the highest permittivity value of 27± 2 was obtained for the film heated at 400 °C. However, a lower processing temperature led to an important and continuous decrease in the permittivity of the samples (see Fig. 3(a)). All samples exhibited dielectric losses up to about 5% at 100 kHz (Fig. 3(b)). The leakage currents of the investigated thin films increased with the processing temperature. The current density values measured at 160 kV/cm for all samples are given in Fig. 3(c).

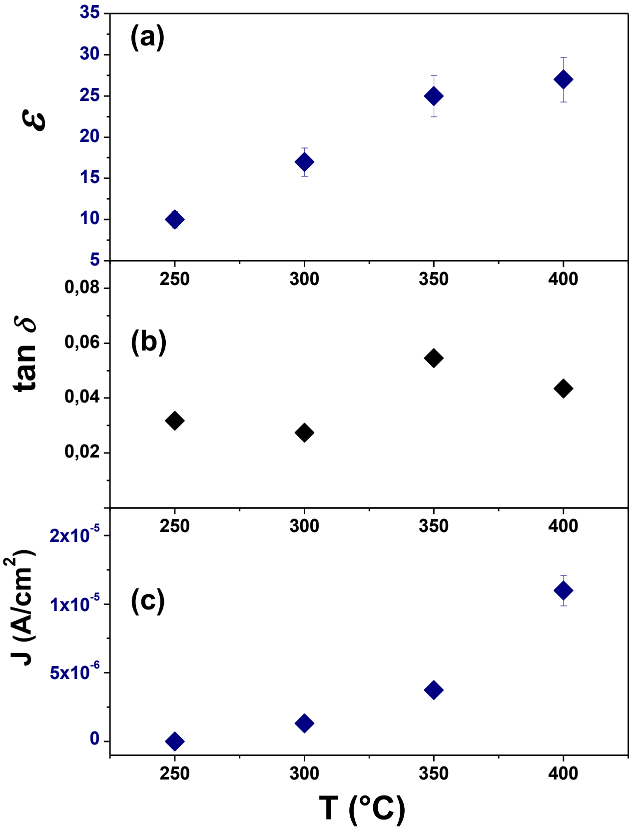

Figure 3: Electrical properties of the Ta_2O_5 thin films as a function of the processing temperature: (a) dielectric permittivity and (b) loss factor at 100 kHz, and (c) leakage current density at the applied field of 160 kV/cm.

Altogether, the electrical properties of the investigated samples depended on the thermal budget of the dielectric, and as previously shown, the optimal processing temperature should be at least 300 °C in order to ensure a good material yield. Therefore thin films processed at 300 and 350 °C were further employed in TFTs.

To evaluate the performance of the devices, the transfer characteristics (*i.e.*, the plots of the drain current (I_D) versus the gate voltage (V_G) at a constant drain voltage (V_D)) were recorded. Fig. 4 depicts the obtained plots together with two of the parameters that can be extracted from such curves. The *on/off* ratio is defined as the ratio of the maximum to the minimum drain current, and it evaluates the quality of the device from the point of view of an electronic switch application. It should be as large as possible, and values above 10^6 are typically reported [12]. The *subthreshold swing* (*S*) is the parameter that reflects the *gate voltage* required to increase *the drain current* by one decade, *i.e.*, it is the inverse of the maximum slope of the transfer characteristics. Small values of *S* ensure low power consumption of the device, and values of about 0.1-0.5 V/dec are generally required [13]. Compared to reports in the literature [14-16], the gate dielectrics from solution rendered high *on/off* values and low *subthreshold swing* values. The processing temperature of 350 °C rendered a slight improvement in terms of *field-effect mobility, i.e.,* 21 cm^2/V compared to the value of about 16 cm^2/V obtained for the TFT with the 300 °C dielectric.

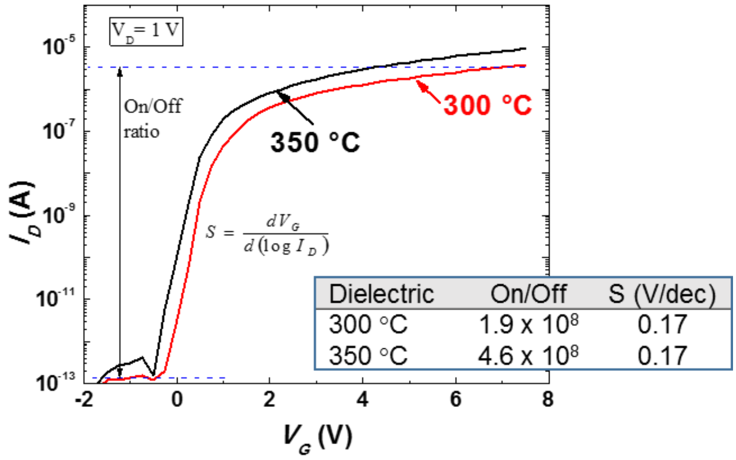

Dielectric	On/Off	S (V/dec)
300 °C	1.9×10^8	0.17
350 °C	4.6×10^8	0.17

Figure 4: Transfer characteristics of GIZO TFTs (W/L = 45/90) with the solution-processed Ta_2O_5 dielectrics, which were obtained at $V_D = 1V$. Some electrical properties extracted for these devices are given in the inset table.

4 Conclusions

Solution-derived Ta_2O_5 thin films were processed at temperatures not exceeding 400 °C. The amorphous thin films exhibited smooth and flat surfaces with low average roughness values. Residues of functional groups remained in the films upon heating at 250 ºC, and they could be detected in a much lower amount upon heating at 400 ºC, as evidenced by the FT-IR. In accordance with the densification taking place at higher heating temperatures, the refractive index ranged from 1.7 to 1.99 for the processing temperatures in the range 250–400 °C. Moreover, the samples processed at higher temperatures exhibited higher permittivity values. The film processed at 400 °C exhibited the permittivity value of 27± 2. Yet, the leakage currents increased with the heating temperature.

Spin-coated Ta_2O_5 thin films processed at 300 and 350 ºC were studied aiming to give a proof of concept for their integration as components in active electronic devices. The TFTs rendered good operating properties, such as *on/off* ratios of the order of 10^8 and a field-effect mobility larger than 10 cm^2/Vs, with slight improvements obtained in the case of the processing temperature of 350 ºC. Therefore, the investigated Ta_2O_5 thin films from solution exhibited promising properties for both passive and active electronic devices.

Acknowledgements:

The authors would like to thank the groups of Prof. Dr. Elvira Fortunato and Prof. Dr. Rodrigo Martins from CENIMAT-I3N and CEMOP/UNINOVA, Portugal for fabricating the TFT structures. We would like to thank to the Centre of Excellence NAMASTE, for the use of AFM.

We acknowledge the financial support of the Slovenian Research Agency (Young researcher programme, contract number: 1000-10-310134; projects: J2-4173, P2-0105, and bilateral project PR-04253, contract number: BI-RO/12-13-001), and of the EU7FP Project "ORAMA", Grant Agreement NMP3-LA-2010-246334.

References:

[1] R. C. Frunză, B. Kmet, M. Jankovec, M. Topič, B. Malič. Ta_2O_5-based high-K dielectric thin films from solution processed at low temperatures. *Materials Research Bulletin*, 50:323-328, 2014.

[2] C. Chaneliere, J. L. Autran, R. A. B. Devine, B. Balland. Tantalum pentoxide (Ta_2O_5) thin films for advanced dielectric applications. *Materials Science and Engineering: Reports*, R22(6):269-322, 1998.

[3] P. G. Clem, N.-L. Jeon, R. G. Nuzzo, D. A. Payne. Monolayer-Mediated Deposition of Tantalum(V) Oxide Thin Film Structures from Solution Precursors. *Journal of the American Ceramic Society*, 80(11):2821-2827, 1997.

[4] G. Scherer. Sintering of sol-gel films. *Journal of Sol-Gel Science and Technology*, 8(1-3):353-363, 1997.

[5] R. C. Frunză, M. Jankovec, B. Kmet, M. Topič, B. Malič. Current transients in dielectric Ta_2O_5-based thin films from solution. *Informacije MIDEM*, 44(1):21-26, 2014.

[6] P. Barquinha, L. Pereira, G. Gonçalves, R. Martins, D. Kuščer, M. Kosec, E. Fortunato. Performance and Stability of Low Temperature Transparent

Thin-Film Transistors Using Amorphous Multicomponent Dielectrics. *Journal of The Electrochemical Society*, 156(11):H824-H831, 2009.

[7] D. Saygin-Hinczewski, K. Koc, I. Sorar, M. Hinczewski, F. Z. Tepehan, G. G. Tepehan. Optical and structural properties of – thin films. *Solar Energy Materials and Solar Cells*, 91(18):1726-1732, 2007.

[8] J.-Y. Zhang, B. Lim, I. W. Boyd. Thin tantalum pentoxide films deposited by photo-induced CVD. *Thin Solid Films*, 336(1–2):340-343, 1998.

[9] F. Z. Tepehan, F. E. Ghodsi, N. Ozer, G. G. Tepehan. Optical properties of sol–gel dip-coated Ta_2O_5 films for electrochromic applications. *Solar Energy Materials and Solar Cells*, 59(3):265-275, 1999.

[10] J.-Y. Zhang, L.-J. Bie, V. Dusastre, I. W. Boyd. Thin tantalum oxide films prepared by 172 nm Excimer lamp irradiation using sol–gel method. *Thin Solid Films*, 318(1–2):252-256, 1998.

[11] P. C. Joshi, M. W. Cole. Influence of postdeposition annealing on the enhanced structural and electrical properties of amorphous and crystalline Ta_2O_5 thin films for dynamic random access memory applications. *Journal of Applied Physics*, 86(2):871-880, 1999.

[12] P. Barquinha, L. Pereira, R. Martins, E. Fortunato. *Transparent Oxide Electronics: From Materials to Devices*. Chichester, UK: John Wiley & Sons, Ltd, 2012.

[13] J.-S. Park, H. Kim, I.-D. Kim. Overview of electroceramic materials for oxide semiconductor thin film transistors. *Journal of Electroceramics*, 32(2-3):117-140, 2014.

[14] L. Zhang, J. Li, X. W. Zhang, X. Y. Jiang, Z. L. Zhang. High performance ZnO-thin-film transistor with Ta_2O_5 dielectrics fabricated at room temperature. *Applied Physics Letters*, 95(7 - 072112):1-3, 2009.

[15] P. Barquinha, L. Pereira, G. Gonçalves, R. Martins, E. Fortunato, D. Kuscer, M. Kosec, A. Vilà, A. Olziersky, J. R. Morante. Low-temperature sputtered mixtures of high-κ and high bandgap dielectrics for GIZO TFTs. *Journal of the Society for Information Display*, 18(10):762-772, 2010.

[16] C. J. Chiu, W. Y. Weng, S. J. Chang, S.-P. Chang, T. H. Chang. A Deep UV Sensitive Ta_2O_5/a - IGZO TFT. *IEEE Sensors Journal*, 11(11):2902-2905, 2011.

For wider interest

In the past years, transparent electronics emerged as a promising technology considered to have the potential to be the next generation of optoelectronics. Thin film transistors (TFTs) are the key components in most modern circuits used to amplify or switch electronic signals. A TFT is a special type of field-effect transistor formed by placing a thin dielectric layer (also referred to as the *gate dielectric*) as well as an active semiconductor layer and metallic contacts (*i.e.*, source, drain, gate) onto a supporting substrate. Furthermore, the fabrication of transparent TFTs requires low cost deposition of thin films with suitable properties onto substrates needing low temperature processing, as glass or even plastic.

Several different high-*K* (*K*= permittivity, dielectric constant) metal oxides have been researched for gate dielectric applications. Ta_2O_5 thin films were found to be suitable for metal–oxide–semiconductor field-effect transistors and high density memory cells due to their high dielectric permittivity, in the range from 20 to 28 for the amorphous state, high refractive index and chemical and thermal stability. In the past years, the use of Ta_2O_5 as a gate dielectric in transparent TFTs has also been proposed.

For microelectronic and optoelectronic applications, high quality thin films (both from the structural and electrical point of view) are required, and various deposition techniques may be employed for their fabrication. As regarding Ta_2O_5 gate dielectrics, it was found that the properties and performance of the thin films depend strongly on the fabrication process. Ta_2O_5 thin films fabricated by physical deposition methods and processed at low temperatures were employed in transparent TFTs. However, little work has been done on the sol-gel preparation of such materials.

The current work reports the preparation and characterization of solution-derived Ta_2O_5 thin films and provides a proof of concept for their use in transparent TFTs.

Matrix degradation as a mechanism for nanoparticles release from food contact materials

Viviana Golja[1,2], Goran Dražić[2,3,4], Martina Lorenzetti[4], Maša Zalaznik[5], Mitjan Kalin[5], Saša Novak[2,4]

[1] National Institute of Public Health, Ljubljana, Slovenia

[2] Jožef Stefan International Postgraduate School, Ljubljana, Slovenia

[3] Laboratory for Materials Chemistry, National Institute of Chemistry, Ljubljana, Slovenia

[4] Department of Nanostructured Materials, Jožef Stefan Institute, Ljubljana, Slovenia

[5] Laboratory for Tribology and Interface Nanotechnology, Faculty of Mechanical Engineering, University of Ljubljana, Slovenia

Viviana.Golja@nijz.si

Abstract.

Materials in contact with foodstuffs may contain nanoparticles which improve their properties. However, transfer of nanoparticles from the material into foodstuffs is not desirable. When nanoparticles are embedded in the matrix, probability of transfer is small, but release can be promoted by matrix degradation. Matrix degradation of quasi-ceramic coating on commercially available pans was studied. The most probable mechanisms of degradation were identified as mechanical, thermal and chemical. Our results show that matrix degradation during the worst case conditions of use may cause particles release into foodstuffs.

Keywords: food contact, nanoparticles, matrix degradation, release

1 Introduction

During the preparation, food comes into contact with different materials. Recently, new food contact materials are developed containing nanoparticles (Chaudhry et al., 2008). Possibility of nanoparticles release from materials into the food cause safety concerns as materials in nano size have different biological properties in comparison with bulk materials (Nel et al., 2006, EFSA, 2009).

It is not much known about nanoparticles release into the food. One possible mechanism identified to describe the release of nanoparticles from food contact materials into food is matrix degradation. The aim of our study was to investigate such process for so called quasi-ceramic non-stick pan coating containing micro and nano particles of TiO_2 and SiO_2 embedded in silicone matrix.

2 Materials and methods

Pan with quasi-ceramic non-stick coating was purchased from the Slovenian market. Microstructure of the coating surface was observed by field emission scanning electron microscopy (FE SEM, JEOL JSM 7600F, Japan), cross section of the coating was observed by focused ion beam scanning electron microscopy (FIB SEM, FEI Nanolab Helios 650 dual beam, OR, USA).

The thermal degradation of the coating was examined by differential scanning calorimetry/thermogravimetric analysis (DSC/TG, NETZSCH STA 449 C/6/G Jupiter – QMS 403) during heating up to 700 °C, with a rate of 10 ^{o}C /min.

Mechanical resistance of the coating toward scratching with metallic objects (e.g. cutlery) was studied by linear progressive scratch test on the sample P2 using a diamond indenter (Revetest Scratch tester CSM Instruments RST S/N 01-04283, Switzerland). The load was progressively increased from 1 N to 30 N, with a rate of 93,10 ± 0,01 mm/min and scratch length of 3 mm. The appearance of the wear debris was observed by stereo microscope (Zeiss Discovery V8, Germany), field emission scanning electron microscopy (FE SEM, JEOL JSM 7600F, Japan) and focused ion beam scanning electron microscopy (FIB SEM, FEI Nanolab Helios 650 dual beam, OR, USA).

The long-term wear behaviour of the coating P2 was tested on dedicated tribological tester (UMT-2, CETR, CA, USA) in a form of a pin-on-disk reciprocal sliding configuration to mimic the worst case conditions. The tribological tests were conducted for one hour at normal load of 3 N, with a stroke of 5 mm and sliding velocity of 0.03 m/s (3 Hz). Polymeric (PA6) and ceramic (Al_2O_3) pins were used against the pan sample, with contact pressures ranging from 1 MPa to 300 MPa, in order to simulate various scenarios of severity during cutlery contact with the pan surface. It is estimated that a normal use of wooden or polymer cutlery would result in pressures well below 100 MPa; however, metal contacts with forks or even knifes in a pan will easily exceed 300 MPa. After the tests, the appearance of the wear scar and the presence of the debris were observed by stereo microscope.

3 Results and discussion

Matrix degradation is one among possible mechanisms of nanoparticles release from nanoparticles containing food contact materials (Newsome, 2014, Noonan et al., 2014) besides desorption, diffusion and dissolution. In the case of quasi-ceramic coatings, which contain TiO_2 and SiO_2 nanoparticles embedded in polymer matrix (microstructure of the coating surface and cross section is shown in Figure 1), desorption of the TiO_2 and SiO_2 nanoparticles is not expected.

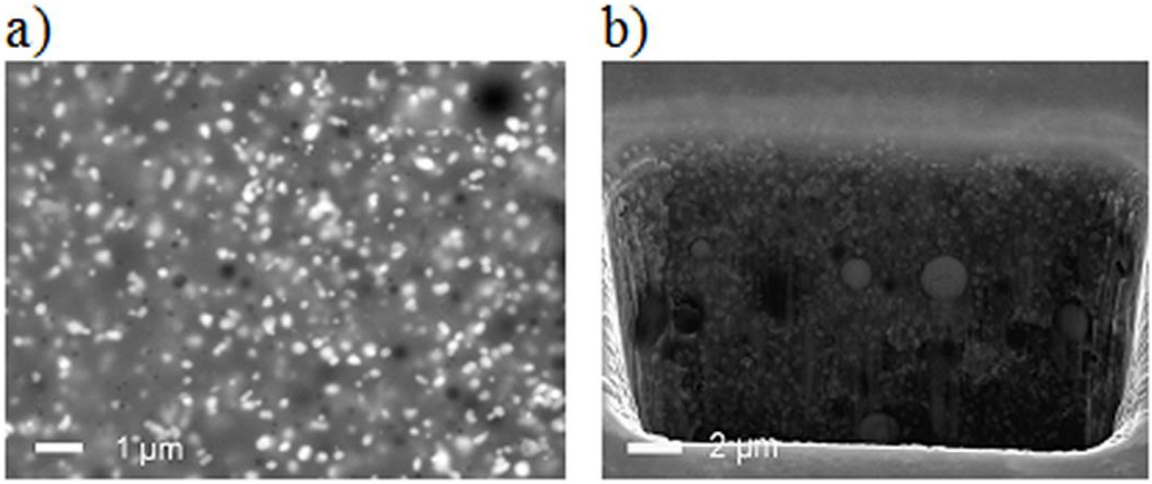

Figure 1: (a) Microstructure of the coating surface observed by FE SEM and (b) cross-section of the coating observed by FIB SEM

For the same reason, diffusion is not an important mechanism. Due to the very limited solubility of TiO_2 within the whole pH region, the mechanism of dissolution and migration of Ti-ions into food can also be considered as negligible. On the other hand, the solubility of SiO_2 is much larger and is relevant in particular in alkaline solutions such as, for example, in dishwashing machines. The dissolution of silica from the matrix and dissolution of the matrix (silicone) will highly likely result in the release of small fragments of SiO_2 and much less soluble TiO_2 nanoparticles. Thus, it might be presumed that the matrix degradation, including chemical degradation, is the most probable mechanism of the particle release from the examined quasi-ceramic pan coatings.

Other than chemical degradation, possible mechanisms of the matrix degradation are also thermal and mechanical ones.

The thermal stability of the pan coating was examined by DSC/TG analysis up to 700 °C (data not shown). Within the temperature range of cooking stove, the weight loss is minor, and the total weight loss up to 700 °C was ~7 % . The peak at 600 °C is accompanied by the formation of CO and CO_2. Furthermore, the first exothermic change, indicating decomposition of the material, appears only over 500 °C, which is above the temperature of exposure during the use.

The appearance of the sample after the DSC/TG analysis is presented in (Figure 2a). After heating at 700 °C, the white TiO_2 particles are not firmly incorporated into the matrix anymore and fine, nano-sized particles became visible (Figure 2b, 2c, 2d).

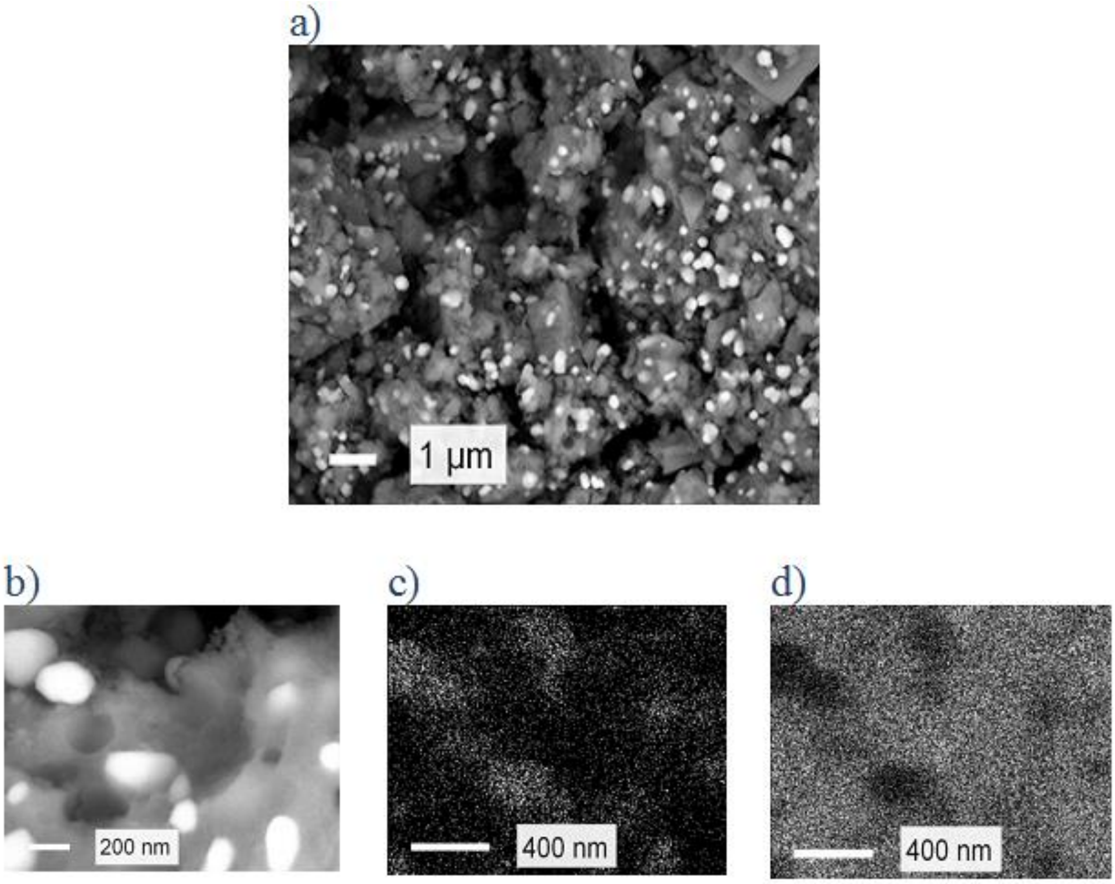

Figure 2: (a) Scanning electron micrograph of the sample after heating at 700 ^{o}C (DSC analysis), (b), (c) and (d) mapping of titanium and silicon distribution

The mapping of the area by EDX analysis (Figure 3a, 3b and 3c) confirmed white particles as being Ti-rich (TiO_2) and the surrounding material as Si-rich (SiO_2). It has to be pointed out that the temperature at which the SiO_2 nanoparticles appeared well visible exceeded the temperature at kitchen stoves; however, these results indicate that, under certain conditions, silica and, consequently, TiO_2 particles can be possibly released from the matrix.

The results of the analysis suggest that under the foreseeable conditions of use the examined coating is relatively stable and the TiO_2 and SiO_2 nanoparticles are not expected to be released by thermal decomposition of the silicon-based matrix, at least in a short term use. However, it is supposed that they can be released into food under more severe conditions, i.e. by (overheating).

Mechanical degradation of the coating was tested by scratch and wear tests. A scratch test was performed under increased load (simulating the worst case of use by e.g. knives, forks), while the wear resistance at constant load for a long time was used to simulate a long term use.

Scratch test was performed, with the load of the pin increased up to 30 N. Visible deformations appeared only at loads above 4 N, where scratches followed by chipping of the material at high loads were observed (Figure 3a). The particles created by chipping of the coating material were small, some were below 1 μm, and had irregular shapes (Figure 3b).

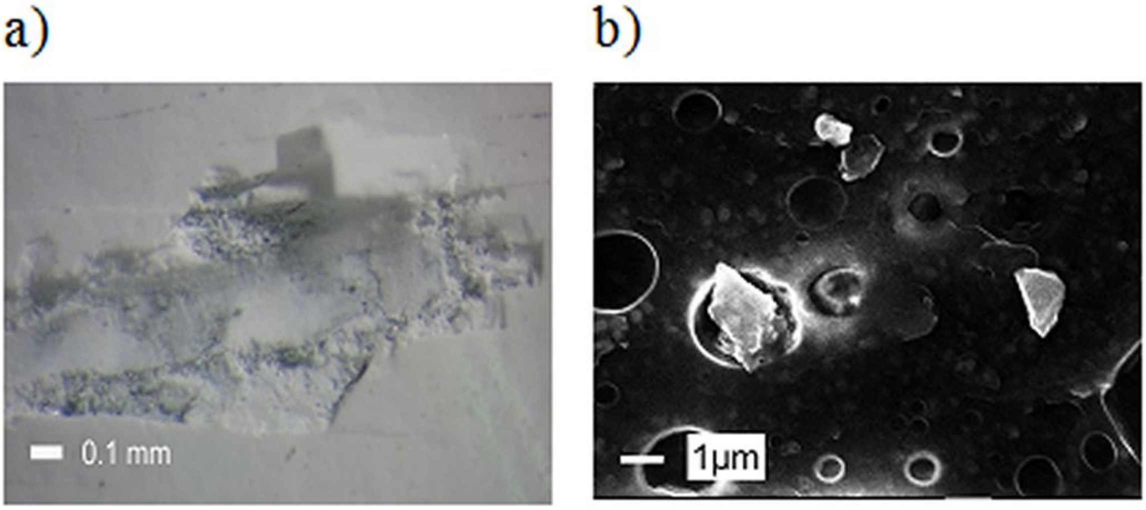

Figure 3: (a) Low magnification image of the scratch and (b) SEM image of the formed particles

This reveals a change from a predominantly elastic deformation at low loads to a brittle fracture under increased load. The appearance of the cracks after scratching the silicon-based coating with high crosslink density was reported to happen even under less severe conditions (Tiwari and Hihara, 2012), where the load was only 0.5 N.

The use of tableware was simulated under mild and more severe tribological conditions for a long time (1 h). Mild conditions simulated recommended use, more severe conditions simulated inappropriate contacts of the pan with any hard and sharp object, such as a fork or a knife.

Under mild conditions (polymer loaded at pressures less than 50 MPa), no visible wear appeared. In contrast, when higher contact pressures were applied by using steel or ceramic counterparts, i.e. above 200 MPa, the brittle nature of the coating became evident, especially above 300 MPa (Figure 4a). Some of produced wear debris was nanosized and had equiaxial shape (Figure 4b). As expected, the debris composition was in agreement with that one of the coating determined by the EDX analysis before the wear test, i.e. predominantly SiO_2 with some TiO_2.

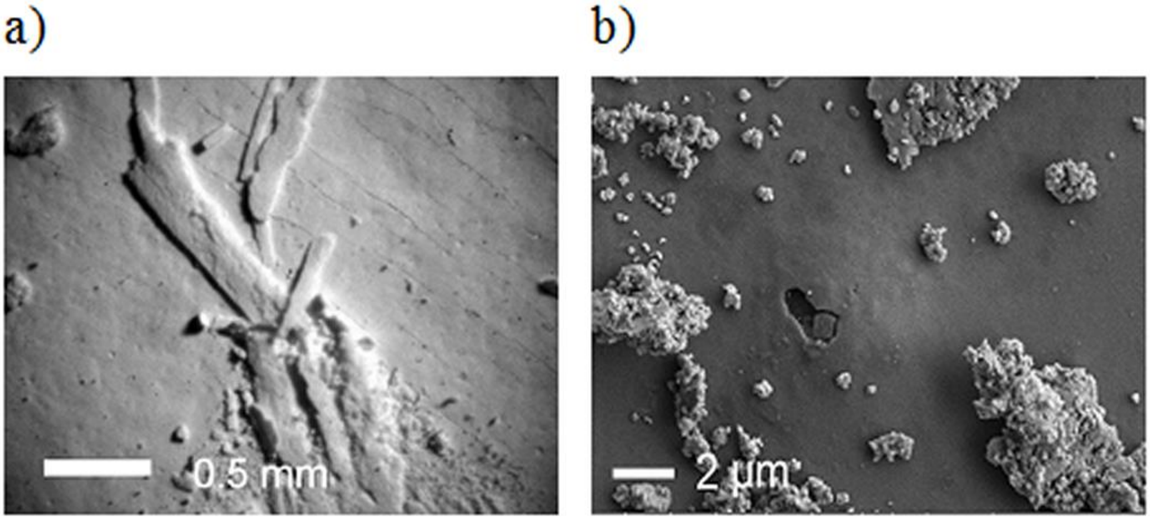

Figure 4: (a) Debris after wear test: stereomicroscope image and (b) SEM micrograph

Finally, photocatalytic degradation after exposure to UV light may also take place to some extent (because TiO_2 particles are present), as described by Wang (Wang et al., 2011). However, it is known that anatase is a much stronger photocatalyst than rutile (van Dyk and Heyns, 1998); regardless of that, indoor exposure of food contact materials to UV light is not particulary relevant.

4 Conclusions

Nanoparticles firmly bonded within the organic phase can be released by degradation of the silicone matrix. Three possible mechanisms of matrix degradation and consecutive particles release were identified: (i) thermal decomposition (overheating or possible long-term heating), (ii) mechanical wear (cutting, scratching) and (iii) chemical (dissolution in alkaline media).

During the worst case conditions of use matrix degradation may cause nanoparticles release into foodstuffs.

Acknowledgments

The authors would like to thank Dr. N. Drnovšek for SEM imaging, Dr. M. Maček for DSC/TG analysis and Dr. S. Paskvale for scratch testing

References:

[1] Q. Chaudhry, M. Scotter, J. Blackburn, B. Ross, A. Boxall, L. Castle, R. Aitken, R. Watkins. Applications and implications of nanotechnologies for the food sector. *Food Addit Contam Part A Chem Anal Control Expo Risk Assess,* 25**,** 241-58, 2008

[2] EFSA The Potential Risks Arising from Nanoscience and Nanotechnologies on Food and Feed Safety. *The EFSA Journal***,** 1-39, 2009

[3] A. Nel, T. Xia, L. Madler, N. Li. Toxic potential of materials at the nanolevel. *Science,* 311**,** 622-627, 2006

[4] R. Newsome. 2013 IFT International Food Nanoscience Conference: Proceedings. *Comprehensive Reviews in Food Science and Food Safety,* 13**,** 190-228, 2014

[5] G.O. Noonan, A.J. Whelton, D. Carlander, T.V. Duncan. Measurement Methods to Evaluate Engineered Nanomaterial Release from Food Contact Materials. *Comprehensive Reviews in Food Science and Food Safety,* 13**,** 679-692, 2014

[6] A.Tiwari, L.H. Hihara. Effect of inorganic constituent on nanomechanical and tribological properties of polymer, quasi-ceramic and hybrid coatings. *Surface & Coatings Technology,* 206**,** 4606-4618, 2012

[7] A.C. Van Dyk, A.M. Heyns. Dispersion stability and photo-activity of rutile (TiO2) powders. *Journal of Colloid and Interface Science,* 206**,** 381-391, 1998

[8] D.L. Wang, S.S. Watson, L.P. Sung, I.H. Tseng, C.J. Bouis, R. Fernando. Effect of TiO2 pigment type on the UV degradation of filled coatings. *Journal of Coatings Technology and Research,* 8**,** 19-33, 2011

For wider interest

New food contact materials may contain nanoparticles which can be released into foods. Nanoparticle release is not desirable. We examined such material (commercially available pan coatings) and find out that coating, in which nanoparticles were firmly bonded before use, decompose if used without care - after scratching with sharp utensils (knives, forks), after overheating during cooking or by dissolution in alkalis (washing in dishwasher machines). Because of coating degradation, nanoparticles may be released into foods.

Controlling the composition of electrodeposited Fe-Pd nanowires and thin films via determination of the diffusion and electrode kinetic parameters

Nina Kostevšek[1,2], Darja Pečko[1], Boris Pihlar[3], Spomenka Kobe[1], Kristina Žužek Rožman[1]

[1] Department for nanostructured materials, Jožef Stefan Institute, Ljubljana, Slovenia

[2] Jožef Stefan International Postgraduate School, Ljubljana, Slovenia

[3] Faculty of Chemistry and Chemical Technology, University of Ljubljana, Ljubljana, Slovenia

nina.kostevsek@ijs.si

Abstract. Fe-Pd alloys have many potential applications because of their unique chemical and magnetic properties, which can be tailored by changing their composition. We have investigated the kinetic parameters for depositing Fe and Pd and their influence on the Fe-Pd alloy's composition, while performing the deposition on a flat Au electrode and into an Au-sputtered porous alumina template. The electrodeposition of Fe and Pd was found to be irreversible and diffusion-controlled. The diffusion coefficient was found to be lower for both metallic ions, by 2-3 times, when the template was used as a working electrode. However, the exchange current densities are comparable for Fe^{2+} and Pd^{2+} on both working electrodes. This indicates that the kinetics of the electrodeposition process is not influenced by the electrode geometry. Because of similar diffusion-coefficient ratios and similar kinetics on both the investigated working electrodes, using the same deposition conditions results in Fe-Pd-based thin films and nanowires having similar compositions.

Keywords: Fe-Pd alloy, electrodeposition, kinetics, flat electrode, alumina template

1 Introduction

Fe-Pd alloys have recently attracted a lot of attention because of their many potential applications that arise from the alloys' specific chemical compositions. In alloys with a Pd content of 28-31 at.% a magnetic shape-memory effect can be observed [1-5]. Alloys containing about 50 at.% of Pd represent promising candidates for micro-electro-mechanical systems (MEMS) due to their high magnetocrystalline anisotropy [6-7]. Pd-rich alloys exhibit catalytic properties, which can result in a high hydrogen-adsorption capacity [8]. In a variety of experiments Fe-Pd thin films [3,7,9], nanowires [6,10] and nanotubes [11,12] with different compositions were fabricated. Electrochemical synthesis represents a cost-effective and efficient method for preparing metals and alloys. The shape of the deposited alloy can be easily modified using the appropriate geometry of the working electrode (WE). If a flat electrode is used as the WE, thin films can be deposited. Furthermore, arrays of nanowires/nanotubes can be obtained if a porous template with a large number of straight cylindrical pores and a narrow size distribution is used. Many studies were dedicated to investigating the physical properties of Fe-Pd alloys [1-4], whereas less attention has been given to the electrochemical aspects.

Rezaei et al. [13] investigated the electrodeposition process for Fe-Pd thin films on a Cu wire electrode. However, the complexity of the deposition process increases when the aim is to deposit an alloy into a porous template. Slow diffusion into long, nonconductive, template channels represents the main barrier for the deposition and the experimental challenge. The mass transport can be additionally hindered due to poorer wetting of the alumina template with an aqueous solution [14]. Therefore, in order to control the deposition and composition of Fe-Pd alloys into porous templates an understanding of the mass transfer and kinetics is of vital importance. The aim of this study was to compare the diffusion and the kinetic parameters of the same electrode process for Fe and Pd deposition by varying the electrode geometry, i.e., a flat electrode and a porous alumina template. A similar kinetic investigation of the deposition parameters was made for gold nanowires into a track-etched polycarbonate template [15]; however, no comparison with the process on a non-porous working electrode was made.

In this work a direct comparison of the mass transport and kinetic parameters of the Fe and Pd deposition on a flat electrode and into a porous alumina template was performed. Cyclic voltammetry (CV) and Butler-Volmer analyses at low over-potentials were used to provide a better understanding of the deposition processes and to calculate the kinetic and diffusion parameters.

2 Experimental

The electrolyte contained 200-mM $FeCl_3$ (Sigma Aldrich, >99.9%) and 30-mM $PdCl_2$ (Sigma Aldrich, 99%). Diammonium hydrogen citrate $(NH_4)_2C_6H_6O_7$ (Fluka, 99%) and ammonia (Merck, 25% aqueous solution) were used as complexing agents for the iron and palladium ions, respectively. In the Butler-Volmer analysis $(NH_4)_2Fe(SO_4)_2x6H_2O$ (Sigma Aldrich, 99%) was used as the source of Fe^{2+} ions. The pH of the prepared solution was adjusted to 9.0 by adding ammonia. All the experiments were performed in a three-electrode cell at room temperature without agitation. Before the measurements were performed the solutions were de-aerated with N_2 gas for 15 min. The reference electrode was an SSCE electrode (Ag/AgCl/3.5-M KCl, HANA Instruments GmbH – type HI5311). A circular platinum mesh was used as the counter electrode (Fig. 1). Two different working electrodes were used, i.e., a commercially available anodized alumina (AAO) template (Whatman Anopore, pore diameter 200 nm) as the porous electrode and glass sputtered with a conductive layer of Au served as the flat electrode. The AAO template and the flat electrode were sputtered with Au in the same batch (20-nm-thick layer of Cr for adhesion and a 600-nm-thick Au conductive layer). A 600-nm-thick layer of Au was sufficient to completely cover the pores of the template. The experiments were conducted in a Teflon cell with the template (Fig. 1a) and the flat electrode (Fig. 1b) facing upwards.

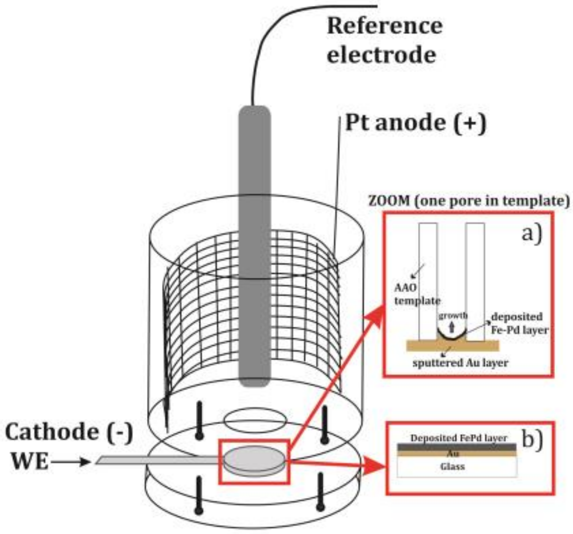

Figure 1: Scheme of the three-electrode cell where a) the WE is an AAO template attached to a holder (the deposition process during the initial stage in the bottom of one pore is schematically shown in the red square) and b) the WE is glass sputtered with Au (the initial stage of the thin film deposition is shown in the red square). The counter electrode is a circular Pt mesh.

For the cyclic voltammetry measurements a potentiostat/galvanostat Gamry Reference 600 equipped with PHE 200 software was used. The scan rate was varied in the range 5-150 mV/s. Thin films and nanowires were deposited potentiostatically at different cathodic potentials from -0.8 V to -1.3 V for 200 s and 900 s, respectively. Scanning electron microscopy (JEOL JSM 7600F) combined with energy-dispersive X-ray spectroscopy (EDXS) was used to determine the chemical composition of the deposited alloy. An accelerating voltage of 7 kV was used for the EDXS analysis. Under such analytical conditions the depth of the x-ray generation for the Fe-L_α and Pd-L_α spectral lines was about 120 nm, which is suitable for examining deposited nanowires with a diameter of 200 nm as well as thin films.

3 Results and discussion

1.1 Cyclic voltammetry of Fe and Pd complexes

The standard reduction potential of iron Fe^{2+}/Fe is -0.44 V vs. the standard hydrogen electrode (SHE), and for palladium Pd^{2+}/Pd the value is +0.95 V (vs. SHE). In order to bring the potentials of both metals closer together and enable their co-deposition, ammonia and diammonium hydrogen citrate (abbrev. Cit) were used as the complex-forming ligands [13]. In Fig. 2 the cathodic part of the cyclic voltammograms for the ammonium citrate, the Fe electrolyte, the Pd electrolyte and the Fe-Pd electrolyte recorded at the flat electrode and in the AAO template are shown. Since we are interested in the deposition of an Fe-Pd alloy, differences in the cyclic voltammograms of a common electrolyte compared to a single-ion electrolyte are important. The black curve in Fig. 2 represents the background electrolyte (only ammonium citrate) where no metal ions are present. The significant increase in the current density at -1.0 V corresponds to the reduction of H_2O, according to the reaction $2H_2O + 2e^- \rightarrow H_2 + 2OH^-$. Similar behaviour can also be observed for the citrate solution in the template (black curve in Fig. 2b). It can be seen that the reduction peaks of the Fe-Pd electrolyte are not in the same positions as in the case of the single-ion electrolyte for both investigated WEs. The reduction peak C_{1Pd} shifts towards more positive values when the Fe-Pd electrolyte was used, as was observed by Rezaei [13]. If the concentration of the Pd complex was reduced, the height of the first peak C_{1Pd} was decreased (not shown), which confirms that the first peak in the Fe-Pd electrolyte corresponds to the Pd reduction process and the second peak C_{1Fe} corresponds to the Fe^{3+}-Cit $\rightarrow$ Fe^{2+}-Cit reduction. The peak for the second reduction step (Fe^{2+}-Cit $\rightarrow$ Fe^0) was hidden in the hydrogen evolution region at more cathodic potentials. It is clear that the reduction peaks C_{1Fe} and C_{1Pd} in the Fe-Pd electrolyte appeared at very similar potentials at both WEs.

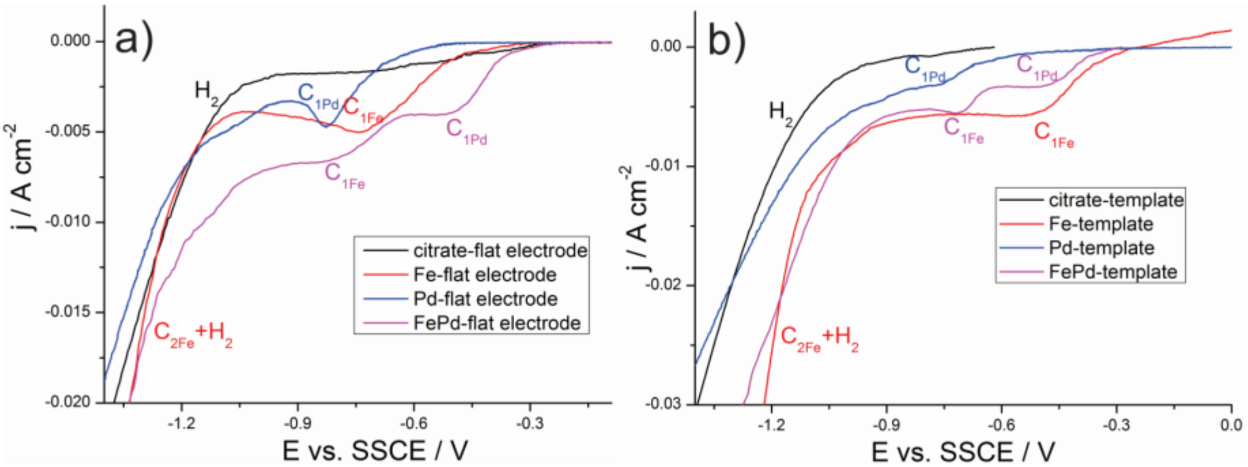

Figure 2: Linear sweep voltammograms of citrate, Fe, Pd and Fe-Pd electrolytes a) at the flat electrode and b) in the template. Scan rate was 20 mV/s.

1.2 Determination of the diffusion and the kinetic parameters using cyclic voltammetry analysis

Fe electrolyte and Pd electrolyte were used to determine diffusion coefficients and kinetic constants for both metallic ions on the flat electrode and in the template at different scan rates (5-150 mV/s).

Reduction peak for the first reduction step for Fe (reaction Fe^{3+}-Cit → Fe^{2+}-Cit) and the reduction peak for the reaction $[Pd(NH_3)_4]^{2+}$→ Pd^0 were used in the calculations. Because of the Fe^{3+} ion being transported from the bulk to the electrode surface, and not Fe^{2+}, which is produced at the electrode surface, we used the peak for the first reduction step (Fe^{3+} → Fe^{2+}) to determine the diffusion coefficient. From the obtained cyclic voltammograms, therefore, we can evaluate only the charge-transfer rate for the first Fe-reduction step, which should be a simple one-electron transfer reaction, while the second reduction step is much more complex [33]. Peak potentials E_p and the peak heights i_p depend on the scan rate on both electrodes for both metallic ions, thus indicating that the reduction is irreversible for the observed time scale. The dependence of the peak current on the square root of the scan rate was found to be linear, which is characteristic for electrodeposition reactions where the rate is determined by diffusion. Therefore, the diffusion coefficient for the irreversible diffusion-controlled process of Fe and Pd deposition was calculated using the Randles-Sevcik equation [16]:

$$i_p = 0{,}496nF^{3/2} \cdot AC_0^* D_0^{1/2} v^{1/2} (\frac{n\alpha}{RT})^{1/2} \qquad (1)$$

where F, α, n, A, D_0, C_0^*, R, T are the Faraday constant, the charge-transfer coefficient, the number of exchanged electrons involved in the electrode process, the active surface area (cm^2), the diffusion coefficient (cm^2/s), the solution bulk concentration (mol/cm^3), the scan rate (V/s), the gas constant and the temperature (K), respectively. In Table 1 the diffusion coefficients for the Fe and Pd electrodeposition process obtained from the voltammetric analyses are listed.

The charge-transfer coefficient α was determined using the Delahay equation [16]:

$$\left| E_p - E_{p/2} \right| = \frac{1{,}857RT}{\alpha n_\alpha F} \qquad (2)$$

where E_p, $E_{p/2}$ and n_α are the peak potential (V), the potential where $j=j_{p/2}$ and the number of electrons in the rate-determining step, respectively.

Dependence of $E_{p-Ep/2}$ vs. (scan rate)$^{1/2}$ is linear, which is characteristic for the irreversible reaction. Charge-transfer coefficients are listed in Table 1.

The diffusion coefficient for Fe^{3+} on the flat electrode is found to be higher ($2.1x10^{-5}$ cm^2/s) than in the AAO template ($0.7x10^{-5}$ cm^2/s). The same trend can be observed in the case of Pd, where the diffusion coefficient for Pd^{2+} on the flat electrode is higher ($5.1x10^{-5}$ cm^2/s) than in the AAO template ($2.7x10^{-5}$ cm^2/s).

From the obtained values it can be seen that the diffusion coefficient in the template is reduced by 2-3 times. Napolskii et al. [17] reported that the diffusion of Ni^{2+} is much slower in the AAO template compared to bulk diffusion, which was attributed to the suppression of diffusion by the electric double layer in the nanochannel. The diffusion coefficient calculated for the $[Pd(NH_3)4]_{2+}$ complex on the flat electrode ($5.1x10^{-5}$ cm^2/s) is slightly higher than in the reports by other authors ($2.2x10^{-5}$ cm^2/s [13] and $1.02x10^{-5}$ cm^2/s [18]). This could be attributed to the different experimental conditions (pH and concentration of the solution). However, in the work of Liang [19] the value for the diffusion coefficient for an Fe(III)-Cit complex of $1\text{-}4x10^{-5}$ cm^2/s is in good agreement with our value ($2.1x10^{-5}$ cm^2/s) for the flat electrode.

From the collected data it can be seen that the obtained charge-transfer coefficient for the Fe^{3+} complex is close to 0.5 at both WEs, which indicates a symmetric process; however, for the Pd^{2+} complex at the flat electrode and in the template the charge-transfer coefficient α is lower than 0.5, which means that the transition state between the oxidation and the reduction form is more asymmetric.

From the analysis of the cyclic voltammograms the kinetic constant k_0 for the rate-determining step in the Fe reduction process ($Fe^{2+} \rightarrow Fe^0$) could not be calculated, because the peaks for this reduction step in the cyclic voltammograms are hidden in the HER region. Therefore, in order to study the kinetics of the Pd^{2+} and Fe^{2+} reduction process a Butler-Volmer analysis at low overpotentials was performed, where the Butler-Volmer equation can be expressed in the form:

$$j = j_0 \frac{F}{RT} \eta, \qquad (3)$$

which shows that the net current is linearly related to the overpotential in a narrow potential region near the equilibrium potential E_{eq} [20]. To determine the exchange current density j_0 for this reduction process, the current was measured with a scan rate of 0.2 mV/s at E_{eq} ±20 mV. For these measurements $(NH_4)_2Fe(SO_4)2x6H_2O$ salt was used as a source of Fe^{2+} ions. The exchange current was normalized to the unit area and the calculated exchange-current densities j_0 are shown in Table 1.

Table 1: Charge transfer coefficients α, diffusion coefficients D and exchange current densities j_0 for Fe and Pd electrodeposition on the flat electrode and in the template (T=25°C)

Ion	Electrode	α	D (cm^2/s)	j_o (A cm^{-2})
Fe^{3+}	Flat electrode	0.46 ± 0.05	$(2.1 \pm 0.1)x10^{-5}$	$(1.1 \pm 0.1)x10^{-4}$ ($Fe^{2+} \rightarrow Fe^0$)
Fe^{3+}	Template	0.63 ± 0.05	$(0.7 \pm 0.1)x10^{-5}$	$(1.5 \pm 0.1)x10^{-4}$ ($Fe^{2+} \rightarrow Fe^0$)
Pd^{2+}	Flat electrode	0.42 ± 0.05	$(5.1 \pm 0.1)x10^{-5}$	$(1.2 \pm 0.1)x10^{-4}$ ($Pd^{2+} \rightarrow Pd^0$)
Pd^{2+}	Template	0.35 ± 0.05	$(2.7 \pm 0.1)x10^{-5}$	$(1.4 \pm 0.1)x10^{-4}$ ($Pd^{2+} \rightarrow Pd^0$)

1.3 Electrodeposition of the Fe-Pd thin films and nanowires

In order to investigate the influence of the kinetic parameters (i.e. the applied voltage) on the final composition, the electrodeposited Fe-Pd nanowires and thin films, deposited into the Au-sputtered AAO templates and on the flat Au electrode, respectively, were investigated. SEM images of Fe-Pd nanowires and thin films deposited at -1.2 V are shown in Figure 3b and 3c, respectively.

The Fe-Pd thin-film depositions were performed potentiostatically using different applied potentials from -0.8 V to -1.3 V vs. SSCE. The Fe content of the thin-film deposits increased from 27 to 75 at. % when the deposition potential changes from -0.8 V to -1.3 V vs. SSCE (Fig. 3a). In the case of the deposition in porous templates, the same potential range was used to deposit Fe-Pd nanowires. When the cathodic potential was changed from -0.8 V to -1.3 V vs. SSCE the Fe content in the nanowires increased from 31 to 76 at. % (Fig. 3a). At more cathodic potentials (more negative than -1.3 V), hydrogen evolution prevailed and disturbed the metal deposition and non-homogenous deposits were obtained (not shown). It can be seen from Fig. 3a that the WE geometry does not influence the alloy composition since the same composition of thin films and nanowires was obtained at the same applied potential. This is consistent with the observation in cyclic voltammograms of the Fe-Pd electrolyte (Fig. 2) where reduction peaks can be found at similar potentials for both WEs. Although the bulk deposition of Fe starts at approx. -1.1 V, a significant amount of Fe in the alloy can be detected at much more positive potentials, which can be related to the Fe underpotential co-deposition [13], like it was observed in the Fe-Pt co-deposition [19,21].

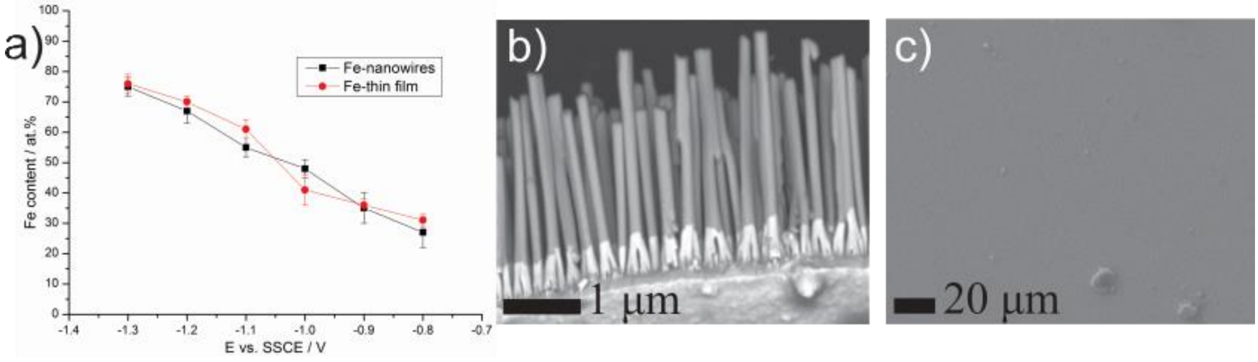

Figure 3: Graph indicating the influence of the cathodic potential on the Fe content in the Fe-Pd alloy in nanowires (template, black squares) and in thin films (flat electrode, red circle), SEM images of b) Fe-Pd nanowires after AAO template removal and c) Fe-Pd thin films at -1.2 V.

The conditions for the Fe-Pd alloy deposition differ from those for single-element Fe and Pd depositions; therefore, the diffusion and kinetic parameters obtained for a single ion are difficult to directly correlate with an alloy formation [22]. However, some conclusions can be made. It can be seen from Fig. 3a that the same composition of thin films and nanowires was obtained if the same deposition conditions were used (i.e., solution and applied potential). From this observation it can be concluded that the deposition process does not differ significantly for the flat electrode and the template. It was calculated that the exchange current densities for Fe^{2+} and Pd^{2+} are similar on both WEs, and because the same composition of the alloy on both WEs was achieved, this could indicate that the kinetics of the alloy deposition is not affected by the WE geometry. Besides the kinetics, also the diffusion should be taken into account when discussing the alloy deposition. A lower diffusion coefficient for both metallic ions in the template is observed not to have a significant influence on the alloy composition. The diffusion coefficients for Fe and Pd ions are reduced in the template by a similar amount (2-3x) in comparison to the diffusion coefficients calculated on the flat electrode. Due to the similar ratio of diffusion coefficient $D_{\mathrm{Fe}}/D_{\mathrm{Pd}}$ the thin-film or nanowire-alloy compositions are practically the same. The diffusion coefficient is reduced in the template in a similar proportion for both the Fe and the Pd ions and, consequently, the same alloy composition can be achieved on both WEs.

4 Conclusions

The kinetics and the diffusion of the electrodeposition process for Fe and Pd were evaluated on a flat Au electrode and in an Au-sputtered porous AAO template. The complexation of both ions, i.e., Fe with citrate and Pd with ammonia, is necessary to make the bath stable and to enable the ion co-deposition. The electrodeposition of Fe and Pd is a irreversible and diffusion-controlled process, both on the flat Au electrode and in the Au-sputtered porous AAO templates. The diffusion coefficient is found to be higher on the flat electrode for both investigated ions, due to the hindered mass transport in long non-conductive AAO pores; furthermore, the Pd diffusion coefficient is found to be larger than that of the Fe for both electrodes. The kinetics of the Fe-reduction process could not be evaluated via a cyclic volammogram analysis, because the peak for the second and rate-determining step of the Fe reduction ($Fe^{2+} \rightarrow Fe^{0}$) overlaps with the HER; however, the kinetics can be investigated by using the Butler-Volmer model at low overpotentials. From the Butler-Volmer calculations it is clear that the obtained exchange current densities j_0 for Fe^{2+} and Pd^{2+} are very similar for the flat electrode and in the template. This was expected, because the rate of the charge transfer across the same metal surface is equal, hence it follows that the geometry of the electrode has no significant influence on the rate of the deposition reaction. An almost equal alloy composition of thin films and nanowires was obtained when the same deposition conditions were used due to the comparable kinetics for both ions and the similar diffusion coefficients ratios $D_{\mathrm{Fe}}/D_{\mathrm{Pd}}$ for both WEs.

Acknowledgment

This work was supported by Slovenian Research Agency (ARRS) via project J2-4316.

References:

[1] J. Buschbeck, S. Hamann, A. Ludwig, B. Holzapfel, L. Schultz, S. Fähler. Correlation of phase transformations and magnetic properties in annealed epitaxial Fe–Pd magnetic shape memory alloy films, *Journal of Applied Physics*, 107: 113919, 2010

[2] T. Cohen-Karni, J. J. Vlassak, Y. Sugimura. Fe-Pd alloy ferromagnetic shape memory thin films, *Journal of Materials Research*, 20: 2279-2287, 2004.

[3] F. Wang, S. Doi, K.I. Hosoiri, H. Yoshida. Nanostructured Fe–Pd thin films for thermoelastic shape memory alloys—electrochemical preparation and characterization, *Electrochimica Acta*, 51: 4250-4254, 2006

[4] M. Sugiyama, R. Oshima, F. E. Fujita. Martensitic transformation in the Fe-Pd alloy system, *Transactions of the Japan Institute of Metals*, 25: 585-592, 1984

[5] I. Kock, T. Edler, S. G. Mayr. Growth behavior and intrinsic properties of vapor-deposited iron palladium thin films, *Journal of Applied Physics,* 103: 46108, 2008

[6] X. L. Fei, S. L. Tang, R. L. Wang, H. L. Su, Y. W. Du. Fabrication and magnetic properties of Fe–Pd nanowire arrays, *Solid State Communications*, 141: 25-27, 2007

[7] S. C. Hernandez, B. Y. Yoo, E. Stefanescu, S. Khizroev, N. V. Myung. Electrodeposition of iron–palladium thin films, *Electrochimica Acta*, 53: 5621–5627, 2008

[8] P. V. Jasen, E. A. Gonzalez, N. J. Castellani, A. Juan. Theoretical study of hydrogen adsorption on FePd face-centered cubic alloy surfaces, *Physical Rewievs*, 71: 235422, 2005

[9] X. N. Sun, X. Y. Xu, Z. B. Tang, G. S. Dong, X. F. Jin. Structure and magnetic properties of Fe_xPd_{1-x} thin films, *Physical Letters A*, 372: 1687–1690, 2008

[10] B. Jeon, S. Yoon, B. Yoo, Electrochemical synthesis of compositionally modulated Fe_xPd_{1-x} nanowires, *Electrochimica Acta*, 56: 401-405, 2010

[11] K. Žužek Rožman, D. Pečko, S. Šturm, U. Maver, P. Nadrah, M. Bele, S. Kobe. Electrochemical synthesis and characterization of Fe70Pd30 nanotubes for drug-delivery applications, *Materials Chemistry and Physics*, 113: 218-224, 2012

[12] H. Liu, F. Wang, Y. Zhao, J. Liu, K. Chul Park, M. Endo. Synthesis of iron–palladium binary alloy nanotubes by template-assisted electrodeposition from metal-complex solution, *Journal of Electroanalytical Chemistry*, 633: 15-18, 2009

[13] M. Rezaei, M. Ghorbani, A. Dolati. Electrochemical investigation of electrodeposited Fe–Pd alloy thin films, *Electrochimica Acta*, 56: 483-493, 2010.

[14] R. Redón, A. Vázquez-Olmos, M. E. Mata-Zamora, A. Ordóñez-Medrano, F. Rivera-Torres, J. M. Saniger. Contact angle studies on anodic porous alumina, *Journal of Colloid and Interface Science*, 287: 664-670, 2005.

[15] L. Soleimany, A. Dolati, M. Ghorbani. A study on the kinetics of gold nanowire electrodeposition in polycarbonate templates, *Journal of Electroanalytical Chemistry*, 645: 28-34, 2010.

[16] R. S. Nicholson, I. Shain. Theory of stationary electrode polarography. Single scan and cyclic methods applied to reversible, irreversible, and kinetic systems, *Analytical Chemistry*, 36: 706-723, 1964

[17] K. S. Napolskii, I. V. Roslyakov, A. A. Eliseev, D. I. Petukhov, A. V. Lukashin, S.-F. Chen, C.-P. Liu, G. A. Tsirlina. Tuning the microstructure and functional properties of metal nanowire arrays via deposition potential, *Electrochimica Acta*, 56: 2378-2384, 2011.

[18] R. Le Penven, W. Levason, D. Pletcher. Studies of the electrodeposition of palladium from baths based on $[Pd(NH_3)_2X_2]$ salts. I. $[Pd(NH_3)_2Cl_2]$ baths, *Journal of Applied Electrochemistry*, 20: 399-404, 1990

[19] D. Liang, J. J. Mallett, G. Zangari. Underpotential codeposition of Fe–Pt alloys from an alkaline complexing electrolyte: Electrochemical studies, *Journal of Electrochemical Society*, 158: D149-D157, 2011.

[20] A. J. Bard, L. R. Faulkner, *Electrochemical methods, Fundamentals and applications*, New York, John Wiley and Sons, 2001.

[21] K. Leistner, S. Oswald, J. Thomas, S. Fähler, H. Schlörb, L. Schultz. Potential dependence of composition and structure of electrodeposited Fe–Pt films, *Electrochimica Acta*, 52: 194-199, 2006
[22] J. J. Mallett, E. B. Svedberg, S. Sayan, A. J. Shapiro, L. Wielunski, T. E. Madey, W. F. Egelhoff, T. P. Moffat. Compositional control in electrodeposition of FePt films, *Electrochemical and Solid State Letters*, 7: C121-C124, 2004

For wider interest

Fe-Pd alloys have many potential applications because of their unique chemical and magnetic properties, which can be tailored by changing their composition. In alloys with a Pd content of 28-31 at.% a magnetic shape-memory effect can be observed, alloys containing about 50 at.% of Pd represent promising candidates for micro-electro-mechanical systems (MEMS) due to their high magnetocrystalline anisotropy and Pd-rich alloys exhibit catalytic properties, which can result in a high hydrogen-adsorption capacity. Electrochemical synthesis represents a cost-effective and efficient method for preparing metals and alloys. The shape of the deposited alloy can be easily modified using the appropriate geometry of the working electrode. Fe-Pd alloy in form of thin films, nanowires and nanotubes with different compositions can be fabricated.

In this study we have investigated the kinetic parameters for depositing Fe and Pd and their influence on the Fe-Pd alloy's composition, while performing the deposition on a flat Au electrode to get Fe-Pd thin films and into an Au-sputtered porous alumina template to get Fe-Pd nanowires. The electrodeposition of Fe and Pd was found to be irreversible and diffusion-controlled. Diffusion coefficients and charge-transfer coefficients were determined by cyclic voltammetry and the exchange current densities for both metallic ions in the porous alumina template and on the flat electrode were determined via a Butler-Volmer analysis. From the obtained results we can conclude that the kinetics of the electrodeposition process is not influenced by the electrode geometry. Moreover, similar diffusion-coefficient ratios $D_{\mathrm{Fe}}/D_{\mathrm{Pd}}$ and similar kinetics on the both investigated working electrodes under the same deposition conditions (i.e., solution and applied potential) results in Fe-Pd-based thin films and nanowires having similar compositions.

In summary, understanding diffusion and kinetic parameters of the electrochemical deposition process allow us to fabricate Fe-Pd alloy with different shapes (thin films, nanowires) and, at the same time, precisely control the composition.

Inkjet printing of alkoxide-based precursor solution for use in transparent electronics

Aleksander Matavž[1,2], Raluca C. Frunză[1], and Barbara Malič[1]
[1] Jožef Stefan Institute, Electronic Ceramics Department, Ljubljana, Slovenia
[2] Jožef Stefan International Postgraduate School, Ljubljana, Slovenia
matawzh@gmail.com

Abstract. We have studied the fabrication of inkjet-printed, a few 10 nm thick 2D-structures of a Ta_2O_5-based dielectric for possible use in transparent electronics. The precursor solution, consisting of Ta-, Al-, and Si-alkoxides dissolved in 2-methoxyethanol and ethanol, was modified in terms of viscosity and surface tension to be suitable for piezoelectric inkjet printing. The viscosity of the solution was increased by admixing a more viscous solvent, i.e. glycerol. The as-prepared ink was stable and jetting even after long periods of time. We adjusted the printing parameters to achieve the best patterning quality on indium tin oxide (ITO) covered glass substrates. The functional properties of the inkjet-printed layers were compared to the state-of-the-art spin-coated films.

Keywords: transparent electronics, inkjet printing, thin films, nanotechnology, sol-gel, metal oxides.

1 Introduction

Transparent electronics has received a lot of attention during the past decade, as a range of new applications and devices can be produced with this technology. It aims towards low manufacturing costs, low temperature processing of materials, and employment of large area deposition techniques that are scalable for industrial production. [1] Nowadays, photolithography is the most widely used patterning technique and it is renowned as a high-resolution technique, yet time consuming and expensive. The deposition technique that meets the requirements of transparent electronics is inkjet printing. It is fast, cost-effective and produces no waste.

The specific fluid requirements represent a large restriction for inkjet printing as the fluids should have the viscosity below 40 mPa·s and the surface tension larger than 20 mN/m. The optimization of the printing procedure with the aim to obtain structures with well-defined geometry and good functional properties is still an ongoing process. A lot of work has been done to determine the printing range of fluids in terms of fluid's physical properties [2-4], and to avoid the so-called "coffee stain" drying phenomena. [5-7] However, there are only handful reports on inkjet printing of metal oxide precursor solutions.

In our study we have chosen to print and investigate dielectric structures based on tantalum(V) oxide, suitable for applications in transparent electronics. Ta_2O_5 has a high dielectric constant of ~25 in the amorphous phase, high refractive index, and high chemical stability. [8, 9] A rather small band gap of tantalum(V) oxide results in relatively large leakage currents. The leakage characteristics can be improved by incorporating materials with a larger band gap, e.g., Al_2O_3 or SiO_2, as previously proposed. [10, 11] The high chemical stability of Ta_2O_5 makes respective thin films difficult to etch, and patterning by inkjet printing arises as a potential solution.

On one hand, chemical solution deposition (CSD) of thin films is a well-established research field, and the physical and chemical properties of the precursor solutions or sols have been established, i.e. viscosity, wetting behavior, chemical reactivity/stability and so on. [12] On the contrary, the deposition of functional materials by inkjet printing is still facing problems.

Following the approach of Tellier et al. [13], we modified the 2-methoxyethanol-based CSD-precursor solution in terms of viscosity and surface tension. We optimized the printing process and prepared structures with well-defined geometry. We investigated the quality of printed layers in terms of profilometry, atomic force microscopy, dielectric and electrical characterization.

2 Experimental

Preparation of the solution and the ink. Alkoxide-based precursor solutions (0.1 M) were prepared at room temperature in an inert nitrogen atmosphere as described in [10]. The ternary composition Ta_2O_5-Al_2O_3-SiO_2 with Ta:Al:Si = 8:1:1, further denoted as TAS solution, was prepared by mixing the precursor solutions in 8:1:1 volume ratio. The ink was prepared by admixing 30 vol. % of glycerol to the TAS solution. The final concentration of the ink was set to 0.05 M.

Characterization of liquids. Viscosity and surface tension were measured at 25 °C using a Physica MCR 301 rheometer and a KRÜSS EasyDrop DSA20E tensiometer, respectively.

Chemical solution deposition. Thin-films were prepared by spin-coating the TAS solution for 30 sec at 3000 rpm on ITO-covered glass. The films were heated in air on a hot plate at 150 °C for 10 min and at 350 °C for 10 min after the deposition of each layer. The process was repeated 5 or 10 times to increase the thickness of film to ~25 or ~55 nm, respectively.

Inkjet printing. Inkjet printing was performed using a Dimatix DMP 2831 piezoelectric printer equipped with a 10 pL cartridge (DMC-11610). The optimal printing parameters were: drop spacing of 20 μm, jetting frequency of 20 kHz, driving voltage of 21 V, height between the cartridge and the substrate of 0.7 mm. The temperature of the cartridge and the substrate was set to ambient. The as-printed structures were heated in air on a hot plate at 150 °C for 10 min and at 350 °C for 10 min after each layer deposition.

Characterization of layers. The surface morphology and cross-sections were investigated by Asylum Research MFP-3D-STM atomic force microscope and JEOL Ltd. JSM-7600F field-emission SEM, respectively. For the dielectric and electrical measurements, we sputtered top contacts through a shadow mask to fabricate the metal-insulator-metal (MIM) capacitors. The capacitance and dielectric losses were measured at room temperature with a driving signal of 50 mV at 100 kHz using a HP 4284A impedance analyzer. The leakage currents were measured using the Aixacct TF 2000E system with the voltage step of 0.1 V and the measurement time of 2 seconds.

3 Results

For a proper drop formation, the Z number (eq. 1) of a fluid should be between 1 and 10. [4] The TAS solution designed for CSD had a relatively high surface tension and low viscosity. The calculated Z number of the solution was 17, which is too high for a stable drop formation. We increased the viscosity of the TAS solution by admixing more viscous glycerol. The density, viscosity, surface tension, and calculated Z number of the solution and the ink are presented in Table 1.

$$Z = \frac{\mathrm{Re}}{\sqrt{\mathrm{We}}} = \frac{\sqrt{a\,\rho\,\gamma}}{\eta} \quad , \qquad (1)$$

where Re is the Reynolds number, We is the Weber number, a is the nozzle diameter, ρ is the density, γ is the surface tension, and η is the viscosity.

Table 1: Physical properties of the CSD solution and the ink.

	Density g cm^{-3}	**Viscosity** mPa s	**Surface tension** mN m^{-1}	**Z**
TAS solution	0.971	1.6	29.6	17
TAS solution + 30% glycerol	1.062	10.1	32.9	3

The solution and the ink were transparent, without agglomerates, and stable for more than 1 month. Both exhibited a constant viscosity at the shear rate ranging from 10 to 500 s^{-1}, suggesting Newtonian behavior. The ink could be jetted from a 10 pL nozzle with a stable drop formation and without occurrence of satellites as shown in Figure 1. The drop volume evaluated by the graphical analysis of the in-flight image was 12 pL.

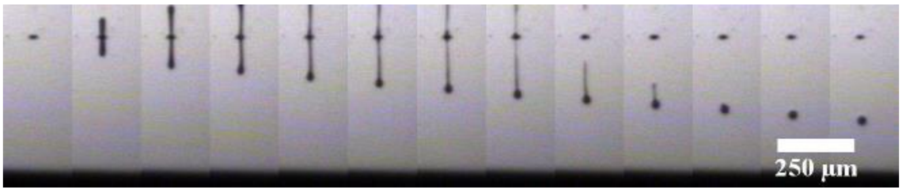

Figure 1: Image sequence of the drop formation upon jetting the ink. The image sequence of the drop formation is separated by 5 µs increments.

During the printing trials we noticed that the contact angle between the ink and the ITO-covered glass decreased when the substrate was annealed prior printing on it. The decrease was induced at temperatures higher than 300 °C and it was time dependent. The contact angle in inkjet printing has to be precisely adjusted. A high contact angle may result in the dewetting process or shape distortion, and low contact angle decreases the resolution of printing. By adjusting the annealing time we were able to control the contact angle and obtain the best printing results.

We printed an array of squares with the lateral dimensions of the squares of 500 x 500 μm^2 and the separation distance between two nearest squares of 250 µm. The drop spacing of 20 µm was selected for printing. The sections of the as-printed, dried and pyrolyzed patterns are shown in Figure 2.

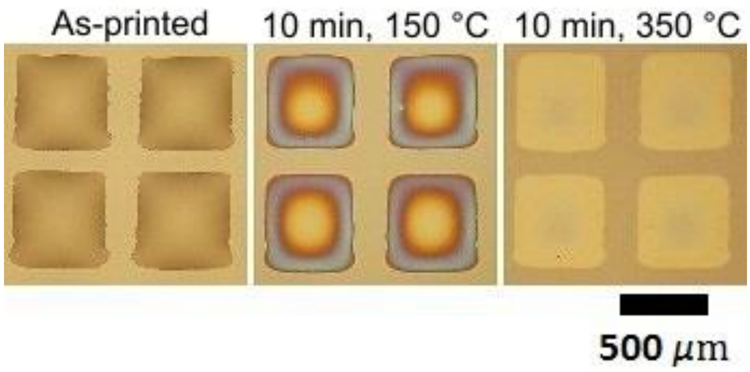

Figure 2: Optical micrographs of the middle part of the inkjet-printed array of squares.

The squares heated at 150 °C [Figure 2 and Figure 3(a)] had a color gradient from the edge toward the center, which corresponded to the thickness variation. The optical observations were confirmed by profilometry measurements shown in Figure 3(b). The measurements of the structures heated at 350 °C revealed higher deposits at the edge of squares. This so-called "coffee stain effect" was more pronounced for the structures consisting of 2 and 3 printed layers.

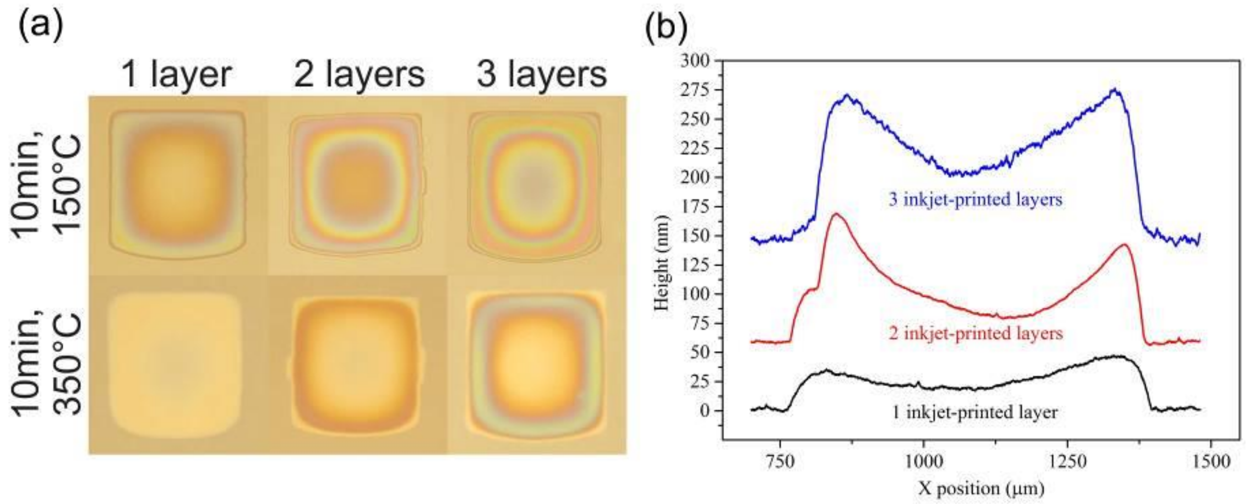

Figure 3: (a) Structures consisting of 1, 2 or 3 inkjet-printed layers. (b) Profilometry measurements of the structures consisting of 1, 2 or 3 inkjet-printed layers, heated at 350 °C.

The surface morphology was investigated by AFM measurements. The printed 2D structures and spin-coated films had uniform surfaces without any evident microstructural details. The Root Mean Square (RMS) surface roughness was found to be in all cases below 0.5 nm for the scan area of 5 x 5 μm^2, confirming that the films were smooth, which agrees with their amorphous nature. [10]

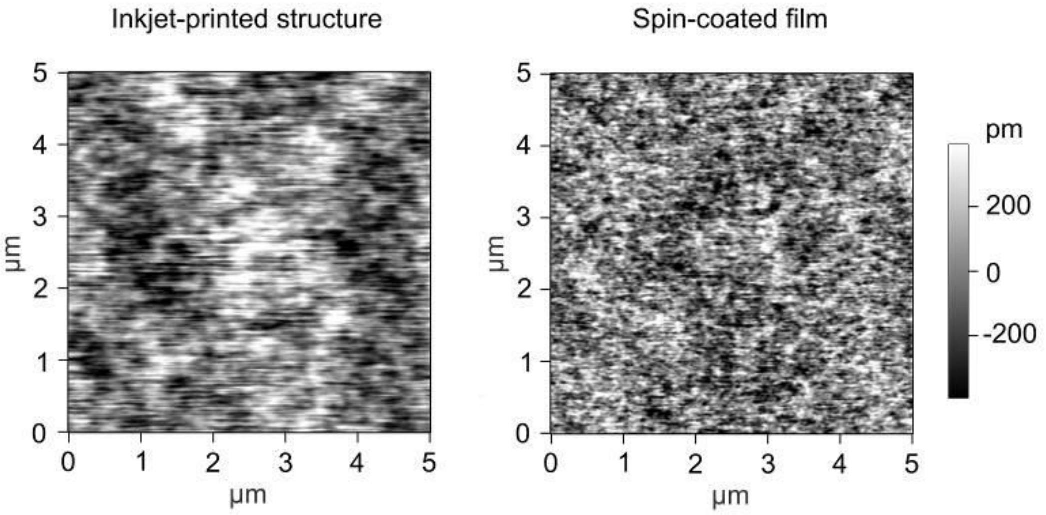

Figure 7: AFM topography image of the structure consisting of 1 layer inkjet-printed and the structure consisting of 10 spin-coated layers on ITO covered glass substrate, heated at 350 °C. The RMS roughness was under 0.5 nm for both samples.

Finally, we investigated the dielectric and electrical performance MIM capacitors. The results are presented in Table 2. The dielectric constant of inkjet-printed structures and spin-coated samples was comparable (~16 at 100 kHz). Regardless of the deposition technique, the dielectric losses decreased with increasing number of layers.

Table 2: The dielectric and electrical performance of thin-film capacitors. The dielectric properties were measured at 100 kHz.

	Dielectric constant	**Dielectric losses**	**J at 200 kV/cm μA/cm²**
1 inkjet-printed layer	**15** ± 2	**0.18** ± 0.06	**8.2** ± 3
2 inkjet-printed layers	**16** ± 2	**0.16** ± 0.06	**1.3** ± 0.1
3 inkjet-printed layers	**15** ± 2	**0.05** ± 0.01	**0.7** ± 0.15
5 spin-coated layers	**17** ± 2	**0.14** ± 0.03	**0.3** ± 0.05
10 spin-coated layers	**16** ± 2	**0.04** ± 0.01	**0.25** ± 0.05

The leakage current measurements revealed a distinct difference between inkjet-printed and spin-coated films (Figure 4). The structures consisting of 1 inkjet-printed layer exhibited the highest leakage currents, about 30 times higher than that of the spin-coated samples. The latter exhibited the lowest leakage currents, with the value below 0.3 μA/cm^2 at the applied electric field of 200 kV/cm. The leakage current of the inkjet-printed structures decreased in with the increasing number of printed layers. The improved performance of multi-layer structures suggests that for a stable operation the printed structure should consist of at least 2 inkjet-printed layers.

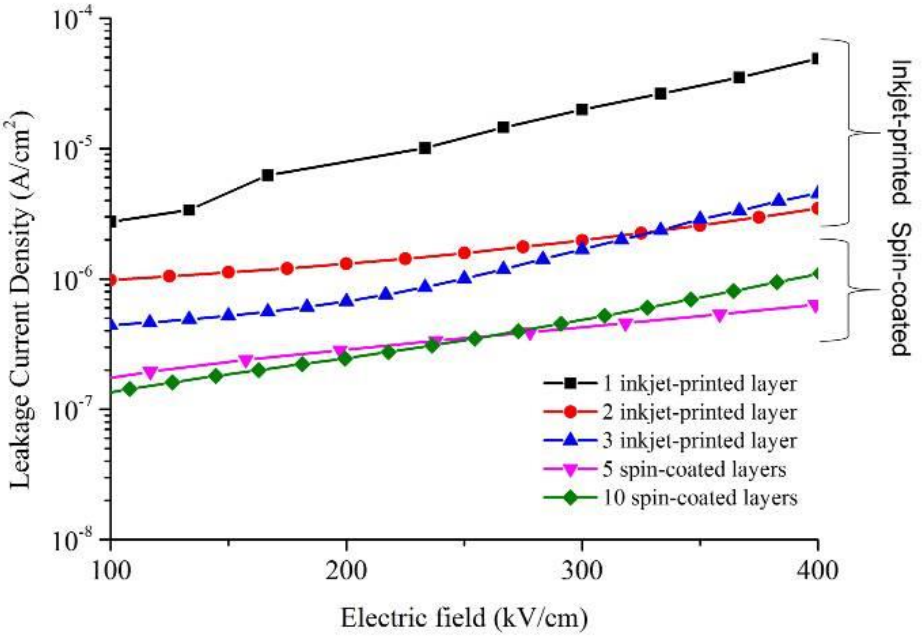

Figure 4: Leakage current measurements of the structures consisting of 1, 2 or 3 inkjet-printed layers and spin-coated films.

4 Conclusions

We successfully modified the alkoxide-based precursor solution originally designed for spin coating to be suitable for inkjet printing. With the addition of a more viscous glycerol we adjusted the physical properties of the TAS spin-coating solution. The jetting of the ink resulted in a stable drop formation, without satellites. The ink could be jetted even after long periods of time, proving good chemical stability of the inks.

We optimized the parameters involved in inkjet printing and fabricated the structures, consisting of 1, 2 or 3 inkjet-printed layers of TAS.

The fabricated features had smooth surfaces, without evident surface details. We compared the dielectric and electrical properties of the inkjet-printed and state-of-the-art spin-coated thin-film capacitors. Both deposition techniques rendered the capacitors with comparable dielectric properties. The spin-coated samples exhibited lower leakage currents, presumably due to the improved film quality with increasing the number of deposited layers.

Acknowledgments

We would like to thank the Centre of Excellence NAMASTE and Nanocenter for providing their equipment. Special thanks go to Aljaž Drnovšek for all profilometry measurements.

We acknowledge the financial support of the Slovenian Research Agency (projects: J2-4173, P2-0105).

References:

1. J.F. Wager, R.E. Presley, and D.A. Keszler. *Transparent electronics*. New York: Springer, 2008.
2. J.E. Fromm. *Numerical calculation of the fluid dynamics of drop-on-demand jets* in IBM Journal of Research an Development, **28**(3): 322-333, 1984.
3. D. Jang, D. Kim, and J. Moon. *Influence of fluid physical properties on ink-jet printability* in Langmuir: the ACS journal of surfaces and colloids, **25**(5): 2629-2635, 2009.
4. N. Reis and B. Derby. *Ink Jet Deposition of Ceramic Suspensions: Modeling and Experiments of Droplet Formation* in MRS Online Proceedings Library, **625**, 2000.
5. E. Tekin, P.J. Smith, and U.S. Schubert. *Inkjet printing as a deposition and patterning tool for polymers and inorganic particles* in Soft Matter, **4**(4): 703-713, 2008.
6. R.D. Deegan, O. Bakajin, and T.F. Dupont. *Capillary flow as the cause of ring stains from dried liquid drops* in Nature, 389: 827-829, 1997.
7. H. Hu and R.G. Larson. *Marangoni effect reverses coffee-ring depositions* in The journal of physical chemistry B, **110**(14): 7090-7094, 2006.
8. P. Barquinha, R. Martins, L. Pereira, E. Fortunato. *Transparent Oxide Electronics*. United Kingdom: John Wiley & Sons, 2012.
9. C. Chaneliere, J.L. Autran, R.A.B Devine, B. Balland. *Tantalum pentoxide (Ta_2O_5) thin films for advanced dielectric applications* in Materials Science & Engineering R-reports, **22**(6): 269-322, 1998.
10. R.C. Frunză, B. Kmet, M. Jankovec, M. Topič, B. Malič. *Ta_2O_5-based high-K dielectric thin films from solution processed at low temperatures* in Materials Research Bulletin, **50**: 323-328, 2014.
11. P. Barquinha, L. Pereira, G. Gonçalves et al. *Low-temperature sputtered mixtures of high-κ and high bandgap dielectrics for GIZO TFTs* in Journal of the Society for Information Display, **18**(10): 762-772, 2010.
12. T. Schneller, R. Waser, M. Kosec, D. Payne, eds. *Chemical Solution Deposition of Functional Oxide Materials*. Wien: Springer, 2013.
13. J. Tellier, B. Malič, D. Kuščer, G. Trefalt, M. Kosec, *Ink-Jet Printing of In_2O_3/ZnO Two-Dimensional Structures from Solution* in Journal of the American Ceramic Society, **94**(9): 2834-2840, 2011.

For wider interest

Inkjet printing is a fairly old deposition technique with the beginnings in 1950s. Since then, it has been extensively used in home and small office applications with a simple task of depositing colored inks on paper. Recently, the technique has caught the interest of scientists as it could be used for micromanufacturing and rapid prototyping.

Inkjet technology has a large potential in transparent electronics as it is economical, produces almost no waste, and is scalable for large-area deposition. In this contribution, we report the fabrication of inkjet-printed capacitors based on tantalum(V) oxide. Dielectrics with high dielectric permittivity, such as tantalum oxide, are essential components of the next generation electronic devices, e.g. field-effect transistors and capacitors.

The physics of drop formation sets restrictions on the viscosity and surface tension of the ink. The precursor solution had a too low viscosity for stable drop formation, thus we admixed 30 vol. % of the highly viscous glycerol. We printed the as-prepared ink onto glass substrates with an ITO conductive coating and fabricated thin-film capacitors with the thickness of the dielectric layer in the nanometer range. The poor electrical performance observed for capacitors consisting of 1 inkjet-printed layer was improved for capacitors consisting of 2 or 3 inkjet-printed layers. The electrical performance of those multi-layer structures was comparable to spin-coated films.

Because of the complexity of inkjet printing, there are only handful reports on printing of metal oxide solutions. We believe our work presents an important contribution to the improvement and the realization of inkjet technology.

Amino-acid-iron-oxide-nanoparticles: adsorption studies and colloidal properties

Klementina Pušnik[1,2], Gregor Marolt[3], Sašo Gyergyek[1], Darko Makovec[1,2,]
[1] Department for Materials Synthesis, Jožef Stefan Institute, Ljubljana, Slovenia
[2] Jožef Stefan International Postgraduate School, Ljubljana, Slovenia
[3]Faculty of Chemistry and Chemical Technology, Ljubljana, Slovenia
klementina.pusnik@ijs.si

Abstract.
For majority of different applications of superparamagnetic iron-oxide nanoparticles in medicine and technology, stable aqueous suspensions are required. One possible type of nontoxic and biocompatible molecules used in the stabilization of aqueous nanoparticles suspensions are amino acids. In this work the adsorption of aspartic amino acid (ASP) onto the iron-oxide nanoparticles and the colloidal properties of their aqueous suspensions were studied. Even the ASP-adsorbed nanoparticles display moderate zeta potential; they form the colloidally-stable aqueous suspensions. Direct analysis of ASP in the supernatant of the ultracentrifuged suspensions using an ion chromatography with pulsed amperometric detection suggested adsorption of the ASP in the form of large molecular associates, sterically stabilizing the suspensions.

Keywords: colloidal stability, adsorption, iron-oxide nanoparticles, amino acids, aspartic acid.

1 Introduction

Superparamagnetic iron-oxide nanoparticles are used in a broad range of technological and biomedical applications. In technology they are mainly used in ferrofluids and in relation to magnetic separation [1]. In medicine they can be used in numerous applications in vitro (e.g., the detection, separation, or sorting of specific cells, magnetofection, etc.) and in vivo for diagnostics (e.g., for contrast enhancement in magnetic resonance imaging (MRI) and in magnetic particle imaging (MPI) and in therapy (e.g., for targeted drug delivery and for cancer treatment using magnetically mediated hyperthermia [2-13]. The iron-oxide nanoparticles are considered safe and have been approved by the US Food and Drug Administration (FDA) for in-vivo applications [2].

Generally, the surface properties of the nanoparticles have to be adapted to meet requirements of different applications. Usually, organic molecules are covalently bonded or adsorbed onto the nanoparticles' surfaces to engineer their surface properties, e.g., surface charge, hydrophilicity/hydrophobicity, or availability of specific functional groups. As the nanoparticles are usually applied in a form of stable suspensions, the surface modification has to provide compatibility with the liquid medium and repulsive forces between the nanoparticles preventing the agglomeration. For in vivo applications, the organic shell of the molecules should be nontoxic and biocompatible. The surface shell at the nanoparticles also significantly determines the interactions of the nanoparticles with living systems, for example, their interaction with the blood. It influences adsorption of plasma proteins onto the nanoparticles, interactions with cells, e.g., the amount of nanoparticles internalized in the cells, a blood-circulation time, and fate of the nanoparticles after intravenous administration. Additionally, it is usually necessary that the surface shell of organic molecules provides specific functional groups (functionalization) for further bonding / (bio)conjugation of different molecules that are needed in a specific application, e.g., targeting ligands, therapy agents, fluorophores, etc.

One possible type of nontoxic and biocompatible molecules that can be used for engineering of the nanoparticles' surface properties and for stabilization of their aqueous suspensions is amino acids. The large number of different amino acids gives opportunity to change the properties, e.g., surface charge and availability of different surface functional groups, in a broad range. Different amino acids have been applied to prepare stable suspensions of iron-oxide nanoparticles [14-20]. It was also proposed, that the adsorbed amino acids can be used for functionalization of the nanoparticles providing specific functional groups at the nanoparticles' surfaces for further bonding of different molecules [14, 15, 18]. As the amino acids play a very important role in the body, their adsorption onto the magnetic nanoparticles was proposed for their targeted delivery [20]. For all mentioned applications the molecules should be bonded to the nanoparticles' surfaces through a strong and stable bond, which will prevent the molecules to be detached from the surface or exchanged with other ligands present in the liquid medium.

Adsorption of the amino acids onto the surfaces of different minerals, including iron oxide, has been intensively studied. Apart from the possible preparation of the nanoparticles suspensions, the adsorption of the amino acids is also important for prebiotic chemistry, in the general frame of evaluating Bernal's hypothesis of prebiotic polymerization in the adsorbed state as a step in organization of molecules in the sequence of organizational events leading to the emergence of life [21]. The interactions between the amino acids and nanoparticles are also very important for understanding the interactions of the nanoparticle with polypeptides and proteins.

It is widely accepted that the amino acids adsorb onto the iron-oxide surface in the form of their respective salts [14-16, 18]. However, the mechanisms of the amino acids adsorption onto the nanoparticles' surfaces are not clear yet and the literature results are frequently inconsistent.

In this work the adsorption of aspartic acid (ASP) onto the iron-oxide maghemite nanoparticles and the preparation of the stable aqueous suspensions have been systematically studied. ASP is an α- amino acid with one amino group and two carboxyl groups ($HOOC-CH_2-CH-(NH_2)COOH$). Sousa et al. [14] showed using FTIR and Raman spectroscopy that the ASP adsorb on the oxide surface by forming a chemical bond of chelate type involving Fe(III) surface species and a carboxylate group. The ASP-modified nanoparticles formed a stable colloidal solution at a pH of 5-8. Mikhaylova et al. [15] reported that an isoelectric point of the suspension of iron-oxide nanoparticles is shifted from neutral pH to alkaline (pH ~ 8.5) suggesting adsorption of ASP with both carboxyl groups onto the surface, leaving the amino group oriented outward the aqueous medium (Scheme 1a). The conductometric measurements have shown that the maximum adsorption of ASP onto the surfaces of iron oxide occurs when the solution pH is near 3. For increasing pH values the uptake of the ASP decreases systematically. The surface saturation at pH ~3 was achieved at approximately 15×10^{-19} mol of the ASP/cm^2 of the oxide surface, corresponding to approximately 90 molecules of ASP/nm^2 [14]. This value is very high and does not support the simple adsorption model based on the adsorption of amino-acid monolayer.

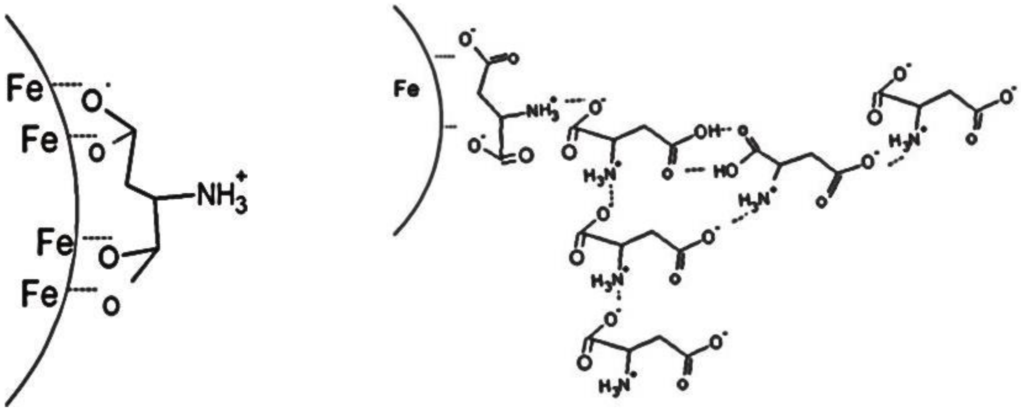

a) b)

Sheme 1: Schematic presentation of aspartic acid adsorption onto iron-oxide nanoparticles as single molecular layer (a) and in the form of molecular associates (b).

2 Experimental Section

The iron-oxide nanoparticles were synthesized using coprecipitation of Fe^{3+} and Fe^{2+} ions from the aqueous solution with aqueous ammonia [22]. Transmission electron microscopy (TEM) revealed that the nanoparticles exhibited a globular shape (Figure 1a). The size distribution (Figure 1a) obtained by measuring at least 150 nanoparticles and fitted by a log-normal distribution showed the equivalent diameter of 10 ± 2 nm. The specific surface area of the nanoparticles was estimated from the TEM average size to be approximately $100 m^2/g$. X-ray diffractometry XRD showed only broad peaks corresponding to a spinel structure. As the nanoparticles were synthesized in an ambient air, it is reasonably to conclude that the Fe^{2+} was completely oxidized and the nanoparticles can be specified as maghemite (γ-Fe_2O_3). The chemical analysis of the nanoparticles synthesized using the same procedure supports this conclusion [22].

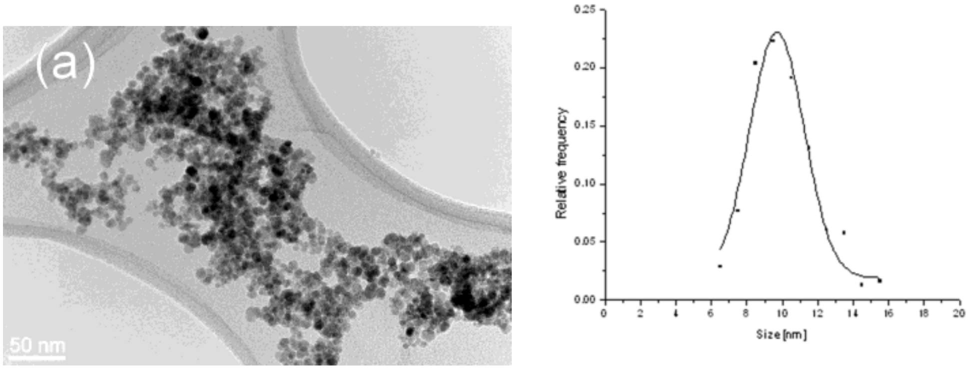

Figure 1. TEM image and the corresponding size distribution of iron-oxide nanoparticles.

Adsorption of ASP onto the iron-oxide nanoparticles was studied indirectly, by observing colloidal properties of the final aqueous suspension of the ASP-adsorbed nanoparticles, and directly, by measuring quantity of the adsorbed ASP in the supernatant of the suspensions.

For the preparation of the stable suspension 2,89 g of ASP was mixed with 450 mL of aqueous suspension containing 1 g of the iron-oxide nanoparticles. The pH of the suspension was set to 4.0 using ammonia and the suspension was mixed for 5 hours. Then, the pH was increased to 11.0 using ammonia. The excess, non-adsorbed ASP was washed from the suspension using ultrafitration (100 mL of the suspension was washed with 300 mL of water). The colloidal properties of the suspensions were investigated by measuring the zeta-potential (Brookhaven, Instruments Corporation, Zeta PALS) and the hydrodynamic-size distribution using the dynamic light-scattering method (DLS) (Fritsch, ANALYSETTE 12 Dynasizer).

The adsorption of the ASP by the nanoparticles was evaluated by measuring of the ASP concentrations in the supernatants of the suspensions after ultracentrifugation of the nanoparticles. First, mother suspension was prepared by mixing 1 g of the iron-oxide nanoparticles in 450 mL of water and setting pH to 4.0 with diluted HCl. The mother suspension was separated in vials containing 45 mL of the suspension with 0.1 g of the nanoparticles. Then, in the vials different amounts of ASP were dissolved, while the pH was maintained at 4.0 with ammonia. After mixing the suspensions for long time (1 week) allowed to reach equilibrium, the nanoparticles were sedimented using ultacentrifugation. The ASP concentrations in the supernatants were measured using ion chromatography (IEC) with pulsed amperometric detection.

3 Results and Discussion

Stable aqueous suspensions of iron-oxide nanoparticles were prepared using aspartic acid (ASP) as the surfactant. First, the ASP was absorbed onto the nanoparticles in aqueous medium at pH = 4. The ASP (HOOC-CH_2-CH-(NH_2)COOH) has two carboxyl groups and one amino group, with pK_1= 2,09, pK_2= 3,86, pK_3= 9,82. We assumed that the ASP at pH = 4 will be attracted to the positively charged surface of nanoparticles with the negatively charged, dissociated carboxyl groups. Figure 2 shows calculated curves showing relative fraction of individual ASP species as a function of pH. At pH = 4 mixture is present, which contains molecules with protonated amino group, and the one or the both carboxyl groups dissociated.

It was directly shown with FTIR and Raman spectroscopy that the aspartic acid forms a chemical bond of chelate type with Fe ions at the iron-oxide surfaces [14-15]. According to a simple model usually described in the literature the amino acid adsorbs onto iron-oxide nanoparticles in a single layer with carboxyl groups attached to the surfaces and amino group oriented toward the medium (see scheme 1a). That should result in a positive surface charge at neutral pH and the shift of the isoelectric point of the aqueous suspension from neutral pH toward an alkaline region [15]. However, zeta-potential measurement (Figure 3) showed no significant differences between the suspensions of the as-synthesized iron-oxide nanoparticles and the ASP-adsorbed-nanoparticles. The as-synthesized nanoparticles exhibited an isoelectric point (IEP) around pH 6. The adsorption of the ASP onto the nanoparticles caused no significant change in the IEP. Also the absolute values of the zeta potential above and below the IEP remained relatively low. The absolute value of zeta potential is related to electrostatic repulsive forces preventing agglomeration of the nanoparticles in the aqueous suspension. Usually, it is assumed that the stable suspension can be formed if the zeta potential exceeds 30 mV [23]. However, when the ASP-absorbed nanoparticles were dispersed at high pH (~ 11) the aqueous suspension seemed colloidally stable, even the zeta potential at that pH was below 30 mV.

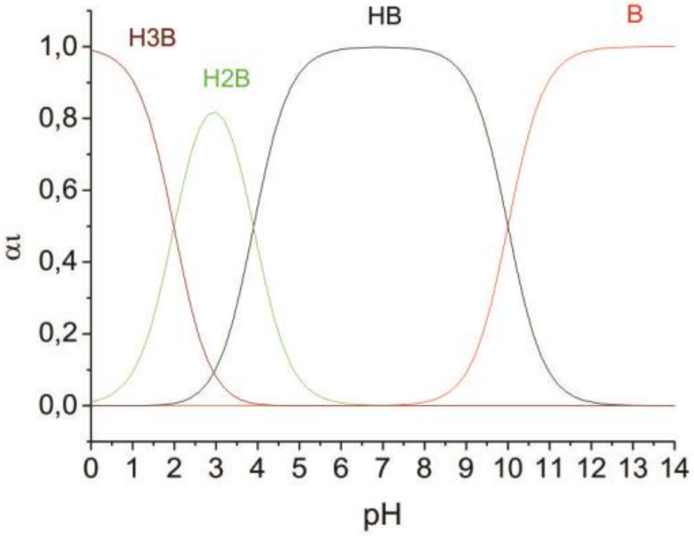

Figure 2. Calculated curves showing relative fraction of individual ASP species as a function of pH (marked in the graph with H3B, H2B, HB, B for undissociated, one carboxyl group dissociated, two carboxyl groups dissociated, amino group deprotonated, respectively).

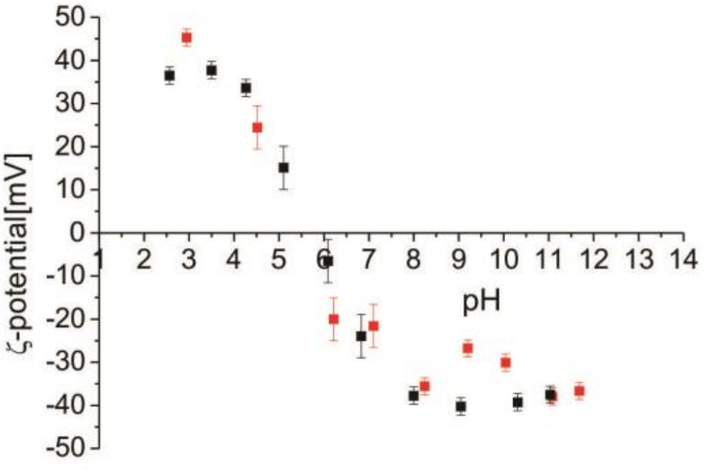

Figure 3. ζ-potential of iron-oxide nanoparticles (black dots) and aspartic-acid-adsorbed iron-oxide nanoparticles (red dots).

The stability of the aqueous suspensions of the aspartic-acid-adsorbed iron-oxide nanoparticles was followed with the DLS measurements. The number-weighted size distribution in Fig. 4 shows that the vast majority of the nanoparticles in the suspension (at concentration of 5 mg of nanoparticles per mL) has hydrodynamic size of approximately 40 nm, however, some larger particles with sizes between approximately 70 nm and 130 nm, were also present. The size did not change significantly with the time. However, after very long time of approximately one month some degree of flocculation was observed in the suspension. The results of DLS measurements also did not change significantly, if the suspension was diluted to 0.1 mg/mL, however, at dilution to 0.05 mg/mL the slow flocculation was visible. The suspension of the as-synthesized nanoparticles was unstable, independently on the pH.

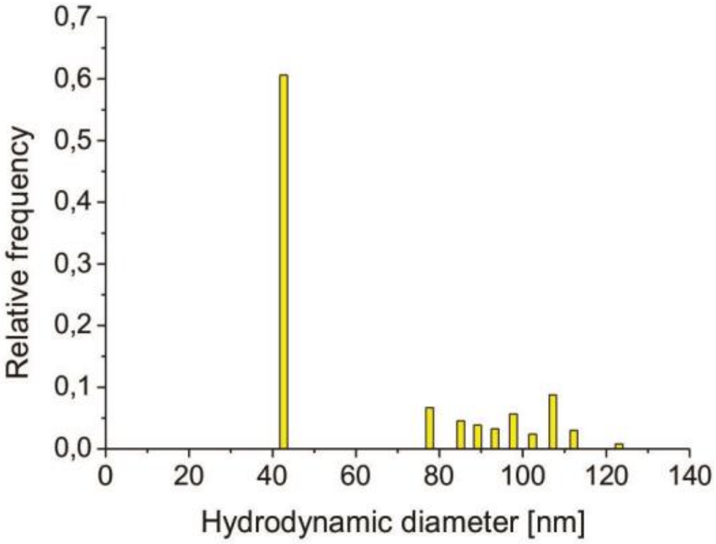

Figure 4. Number-weighted particles size distribution of aspartic-acid-adsorbed iron-oxide nanoparticles in aqueous suspension (5 mg/mL, pH = 11).

The presented zeta potential and DLS measurements are not consistent with adsorption of the ASP onto the iron oxide surfaces in a single molecular layer. Also the good colloidal stability of the ASP-absorbed nanoparticles' suspension is unusual, because the relatively weak electrostatic repulsive forces are expected due to low zeta potential. The hydrodynamic size of the nanoparticles in the suspension measured with DLS (~ 40 nm) is significantly larger the size measured from TEM images (10 nm), suggesting a thicker layer of the molecules at the nanoparticles.

To solve this puzzle, the adsorption of the ASP onto the nanoparticles was systematically studied. The nanoparticles in the aqueous medium were equilibrated with different amounts of the ASP and two different pH values of the suspension. Then, the suspension was ultra-centrifuged to sediment the nanoparticles and the supernatant was analysed using ion chromatography. As the stable colloidal suspension was prepared by adsorption of the ASP onto the nanoparticles at pH=4.0 and their dispersion in water at pH=11, the adsorption of ASP at those two values of pH was measured.

Figure 5 (a) shows the concentration of the ASP in the supernatant of the suspension of the iron-oxide nanoparticles equilibrated with the ASP with different concentrations of the ASP at pH = 4 and pH = 11. The concentrations of the ASP added in the suspensions are expressed in mmol of ASP/g of the nanoparticles. At pH = 4 only very low concentration of the non-adsorbed ASP was present in the supernatant even for the largest addition of the ASP of 21.7 mmol/g of nanoparticles. Thus, the surface concentration of the ASP adsorbed onto the nanoparticles increases almost linearly with the concentration of the added nanoparticles. In the graph of Figure 5b the concentrations of the added ASP and the absorbed ASP are expressed in mmol/cm^2 of the nanoparticles. If the entire added ASP would adsorb at the nanoparticles, the adsorption curve would follow the dashed line in the graph of Figure 5b.

Usually, the adsorption curves show saturation of the surface with the adsorbed ligand. Our results of direct measurements of the ASP in the supernatant of the suspension at pH = 4 did not reach the saturation, even the highest concentration of the ASP added to the suspension of the nanoparticles was close to the solubility limit of the ASP in water. Contrary to our results, Sousa et al. [14] showed by conductometric measurements that the aspartic acids adsorb onto the maghemite surface following an adsorption isotherm. They added the aspartic acid to nanoparticles in the solution of HNO_3 at pH =3. The differences in observed adsorption curves can be related to different procedures.

In the graph of Figure 5a the concentrations of the absorbed ASP are also expressed in number of molecules / nm^2 (right axis). At the highest concentration of the added ASP, more than 120 molecules attach per nm^2 of the nanoparticles' surface. This value is very large and suggests that the ASP is adsorbed in the form of large molecular associates. Most probably, the molecules of ASP in the associates are bonded with hydrogen bonds and also with electrostatic interactions, as schematically presented in Scheme 1b.

The adsorption of the ASP, as well as the formation of the associates depend on the degree of dissociation of the molecules and therefore are a function of the pH. At pH = 11 significantly larger concentration of the ASP remained in the supernatant (Figure 5a). However, the surface concentration of the adsorbed ASP on the nanoparticles is still large, almost 50 molecules of ASP / nm^2 for the highest concentration of the added ASP of 2.17x10^{-5} mmol/cm^2.

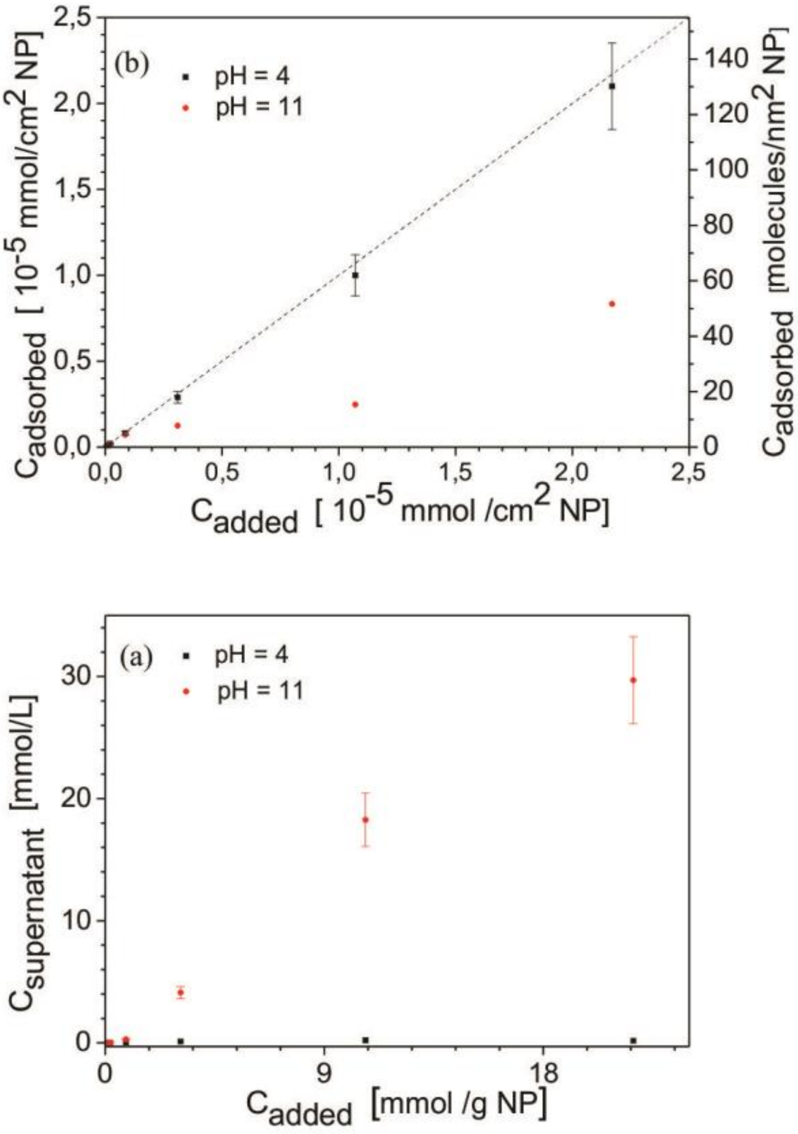

Figure 5: Adsorption isotherm of ASP at pH=4 and pH=11.

The adsorption curves strongly suggest that the ASP is adsorbed onto the nanoparticles' surfaces in the form of the large molecular associates. This is also in accordance with the zeta potential measurements, showing no change in IEP of the suspension with adsorption of the ASP and relatively good colloidal stability of the suspension at relatively low absolute values of the zeta potential. It seems that the suspensions are additionally sterically stabilized by the molecular associates. The presence of the ASP on the nanoparticles' surfaces in the form of the associates also explains the large hydrodynamic size of the nanoparticles in the suspensions measured with DLS, compared to their TEM size.

4 Conclusions

The adsorption of aspartic acid (ASP) on the iron-oxide (maghemite) nanoparticles in aqueous suspension does not change their zeta potential significantly. There is no change in isoelectric point and the absolute values of the zeta potential remained relatively low. However, even the absolute values of zeta potential were low; the suspension of the ASP-adsorbed nanoparticles at basic pH was relatively stable. The adsorption curves measured by direct analysis of ASP in the supernatant of the ultracentrifuged suspensions using an ion chromatography with pulsed amperometric detection suggested that the adsorption of the ASP does not follow an adsorption isotherm. Very high concentrations of the ASP attached onto the nanoparticles suggest that the ASP is adsorbed in the form of large molecular associates, which sterically contribute to stabilization of the suspension.

References:

[1] Primc, D.; Makovec, D. Composite Nanoplatelets Combining Soft-Magnetic Iron Oxide with Hard-Magnetic Barium Hexaferrite. *Nanoscale*, **00**:1-3 (2014).

[2] Magnetic Nanoparticles: From Fabrication to Clinical Applications, T. K. N. Thanh, , Ed.; CRC Press: Boca Raton, USA, 2012.

[3] Safarik I. and Safarikova M. In Magnetic Nanoparticles: From Fabrication to Clinical Applications; N. T. K. Thanh, Ed.; CRC Press: Boca Raton, USA, 2012, pp. 215-241.

[4] Weissleder, R.; Nahrendorf M. and M. J. Pittet, *Nature Mater.*, **13:**125−138 (2014).

[5] Gleich B. and. Weizenecker, J. *Nature*, **435**: 1214−1217 (2005).

[6] Timko, B. P.; Whitehead, K.; Gao, W.; Kohane, D. S.; Farokhzad, O.; Anderson D. and Langer Ann R. *Rev. Mater. Res.*, **41**: 3.1–3.20 (2011).

[7] Yu, M. K.; Jeong, Y. Y.; Park, J.; Park, S.; Kim, J. W.; Min, J. J.; Kim K. and Jon, S. *Angew. Chem. Int. Ed.*, **47**: 5362−5365 (2008).

[8] Lee, J.-H.; Jang, J.-T.;. Choi, J.-S; Moon, S.-H.;. Noh, S.-H; Kim, J.-W. ; Kim, J.-G.; Kim I.-S., Park K.-I. and Cheon J., *Nature Nanotechnol.* **6**: 418−422 (2011).

[9] Meffre, A.; Mehdaoui, B.; Kelsen, V.; Fazzini P. F. and Carrey, J. *Nano Lett.* **12**: 4722−4728 (2012).

[10]Thiesen B. and Jordan, A. *Int. J. Hyperthermia* 24: 467–474 (2008).

[11]Pollert E. and Závêta K. In Magnetic Nanoparticles: From Fabrication to Clinical Applications; N. T. K. Thanh, Ed.; CRC Press: Boca Raton, USA, 2012, pp. 449−478.

[12]Cherukuri, P.; Glazer E. S. and Curley, S. A. *Adv. Drug. Deliv. Rev.*, **62**: (339–345) 2010.

[13]Veverka, P.; Pollert, E.; Závêta, K.; Vasseur S. and Duguet, E. *Nanotehnology* **19**:(215705-1−215705-7)2008.

[14] Sousa, M.H.; Rubim, J.C.; Sobrinho, P.G.; Tourinho,F.A; Biocompaible magnetic fluid precursors based on aspartic and glutamic acid modified maghemite nanostructures. *Journal of Magnetism and Magnetic Materials,* **225**: 67-72 (2001).

[15] Mikhaylova, M.; Kim, D.K.; Berry, C.C.; Zagorodni, A.; Toprak, M.; Curtis. A.S.G.; Muhammed, M. BSA Immobilization on Amine-Functionanalized Superparamagnetic Iron Oxide Nanoparticles. *Chemistry of Materials*, **16**: 2344-2354 (2004).

[16] Durmus, Z.; Kavas, H.; Toprak, M.S.; Bayakal, A.; Altinçekiç T.G.; Aslan.A.; Bozkurt, A.; Coçgun,S. L-lysine coated iron oxide nanoparticles: Synthesis, structural and conductivity characterization. *Journal of Alloys and Coumpounds*, **484**: 371-376 (2009).

[17]Marinescu, G.; Patron, L.; Culita, D. C.; Neagoe, C.; Lepadatu, C. I.; Balint, I.; Bessais, L.; Cizmas, C. B. Synthesis of magnetite nanoparticles in the presence of aminoacids. *Journal of Nanoparticle Research*, **8:** 1045–1051 (2006).

[18]Qu, H.; Ma, H.; Zhou, W.; O'Connor, C. J. In situ surface functionalization of magnetic nanoparticles with hydrophilic natural amino acids. *Inorganica Chemica Acta,* **389**: 60-65 (2012).

[19]Park., Y.J.; Choi, E.S.; Baek, M.J.; Lee, G.H.; Colloidal stability of amino acid coated magnetite nanoparticles in physiological fluid. Materials Letters, 63: 379-381 (2009).

[20]Patel, D.; Chang, Y.; Lee, G.H.; Amino acid functionalized magnetite nanoparticles in saline solution. *Curr. Appl. Phys.* **9** S32–S34 (2009).

[21]Lambert, J.L. Adsorption and Polymerization of Amino Acids on Mineral Surfaces: A Review. *Orig Life Evol Biosph* **38**:211–242 (2008).

[22] Kralj, S.; Drofenik, M.; Makovec, D. Controlled surface functionalization of silica-coated magnetic nanoparticles with terminal amino and carboxyl groups. *J Nanopart Res,* **13**: 2829-2841 (2010).

[23]Tadros, Th. F., 1987. Solid/Liquid Dispersions. Academic Press Inc., London.

[24]Theerdhala, S.; Bahadur, D.; Vitta, S.; Perkas, N.; Zhong, Z.; Gedanken, A. Sonochemical stabilization of ultrafine colloidal biocompatible magnetite nanoparticles using amino acid, L-arginine, for possible bio applications. *Ultrasonics Sonochemistry*, **17**: 730-737(2010).

[25]Viota, J.L.; Arroyo, F.J.; Delgado, A.V.; Horno, J. Electrocinetic characterization of magnetite nanoparticles functionlized with amino acids. *Journal of Colloid and Interface Science*, **344**: 144-149 (2010).

For wider interest

Nano-sized materials such as magnetic nanoparticles, which are a major class of nanoscale materials (ferro/ferrimagnetic materials, such as iron, nickel, cobalt, and magnetic oxides like iron oxides, including magnetite and maghemite), have fascinating physical-chemical properties that if tuned properly, can design new bio-diagnostics and therapeutic strategies, as well as, innovative biotechnology methodologies. The most common synthesis methods of iron-oxides nanoparticles are: co-precipitation, thermal decomposition, hydrothermal synthesis, microemulsion, sonochemical synthesis. Generally, the nanoparticles are used in the form of stable aqueous suspensions.

For biological applications, the magnetic nanoparticles are adsorbed with biocompatible organic molecules, which prevent agglomeration of the iron-oxide nanoparticles in the aqueous suspensions and enables bonding of different molecules needed in application to their surfaces. For in vivo applications, the organic molecules should be nontoxic and biocompatible. One possible type of molecules used in the stabilization of aqueous nanoparticles suspensions is amino acids. The amino acids also play an important role in the body.

In our study, aspartic acid was used for preparation of the stable aqueous suspensions of magnetic iron-oxide nanoparticles. The adsorption of the aspartic acid onto the nanoparticles and the colloidal properties of the suspensions were studied.

Selectivity in the Synthesis of Unsymmetrical Tetraoxanes

Katarina Starkl[1,2], **Jernej Iskra**[1]
[1] Department of Physical and Organic Chemistry (K-3), Jožef Stefan Institute,
Ljubljana, Slovenia
[2] Jožef Stefan International Postgraduate School, Ljubljana, Slovenia
katarina.starkl@ijs.si

Abstract. Unsymmetrical tetraoxanes are representatives of synthetic cyclic peroxides which evolved from artemisinin, a natural product used in the first-line treatment for malaria and a promising antitumor, antiparasitic and antiviral agent. Tetraoxanes might exhibit enhanced antimalarial activity due to two peroxide groups in the molecule that are essential for bioactivity of cyclic peroxides. Chemical synthesis of unsymmetrical 1,2,4,5-tetraoxanes could be straightforward with acid-catalysed cyclization of *gem*-dihydroperoxide and ketone, however problems with formation of various side-products hampers their development. We have studied the cyclization of cyclic *gem*-dihydroperoxides and various ketones in order to develop a general method for synthesis of unsymmetrical tetraoxanes was developed with an emphasis on selectivity of tetraoxanes. The method was adopted for the synthesis of various 1,2,4,5-tetraoxanes which will be evaluated for in-vitro antibacterial and antitumor activity.

Keywords: tetraoxanes, peroxides, artemisinin, antimalarial activity.

1 Introduction

Natural products containing peroxide groups exhibit broad spectrum of bioactivity but they have not been fully exploited as therapeutic agents due to their low availability [1]. Artemisinins and its semi-synthetic derivatives are one of the most important representatives and are recommended as the first-line treatment for malaria for more than a decade (Figure 1). Beside antiparasitic activity, artemisinins exhibit also antitumor, antiviral, antibacterial and anti-inflammatory activity, for which an endoperoxidic group is essential [2].

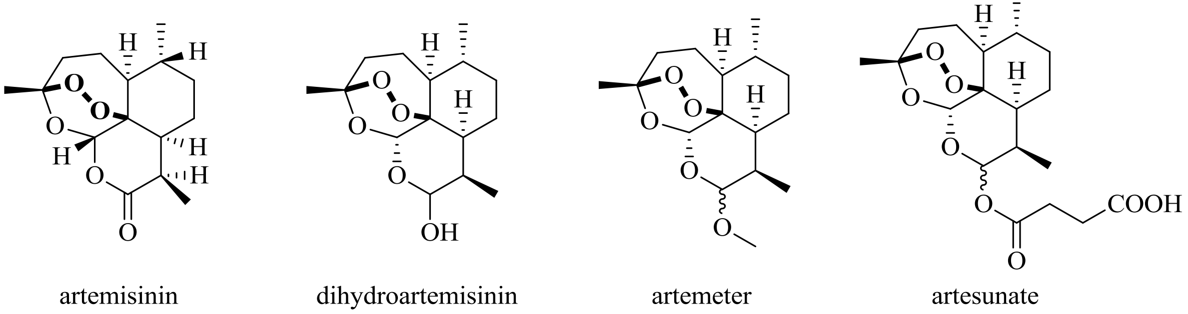

Figure 1: Artemisinin and its semi-synthetic derivatives

Simplification of artemisinin structure, needed to facilitate the production and to improve pharmacokinetic properties, resulted in development of synthetic cyclic peroxides as peroxide bond is essential for their activity (Figure 2).

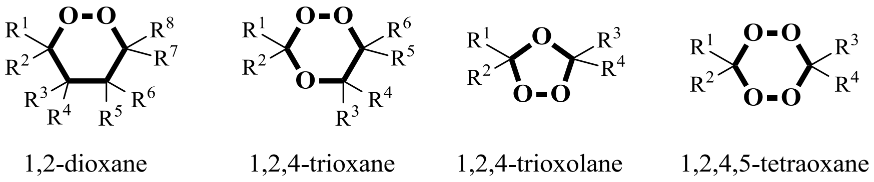

Figure 2: Structural scaffolds of synthetic peroxides

An importance of synthetic peroxides for antimalarial therapy was confirmed in 2011 when the combination of synthetic peroxide arterolane (Figure 3) and quinoline-based drug piperaquine was approved for treatment of uncomplicated malaria [3]. Amongst synthetic peroxides, 1,2,4,5-tetraoxanes may exhibit an enhanced pharmacological activity due to two peroxide groups in the molecule [4]. RKA182 (Figure 3) was identified as the most potent antimalarial candidate with tetraoxane scaffold [5] and, recently, it is undergoing preclinical trials [6].

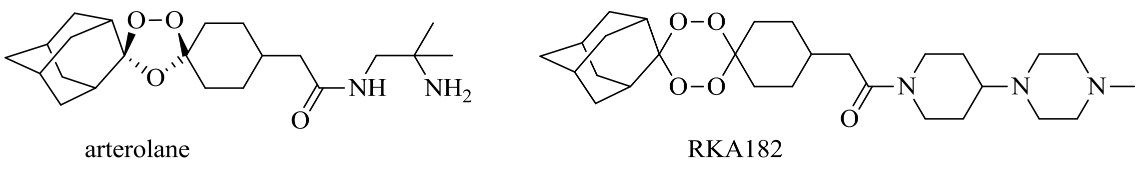

Figure 3: Structure of the most promising synthetic peroxides

In accordance with an increasing role of artemisinins and synthetic peroxides in therapy accompanied by indications of potent bioactivity of tetraoxanes, an interest for development of new synthetic approaches for producing tetraoxanes is augmenting. Symmetrical tetraoxanes could be synthesized directly from carbonyl compounds, while unsymmetrical ones, that hold better potential due to wider structural scope, could only be prepared in two-step procedure with *gem*-dihydroperoxides as intermediate products (Scheme 1) [7].

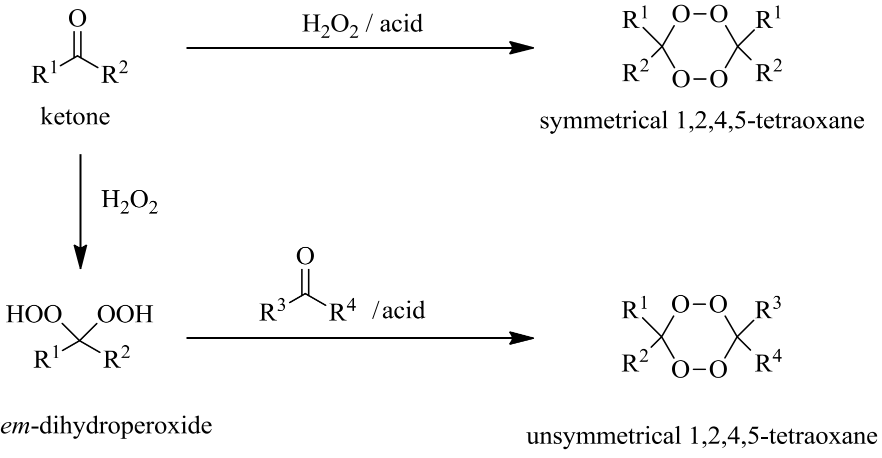

Scheme 1: Synthesis of symmetrical tetraoxanes and two-step procedure for synthesis of unsymmetrical tetraoxanes via *gem*-dihydroperoxides.

The main obstacle of acid catalysed peroxidations of ketones is selectivity due to formation of Baeyer-Villiger products and/or other cyclic products (Figure 4) [8]. Most of all, it is of great importance to avoid formation of 1,2,4,5,7,8-hexaoxonanes which have negligible bioactivity [9] and cannot be separated from desired product due to similar polarity.

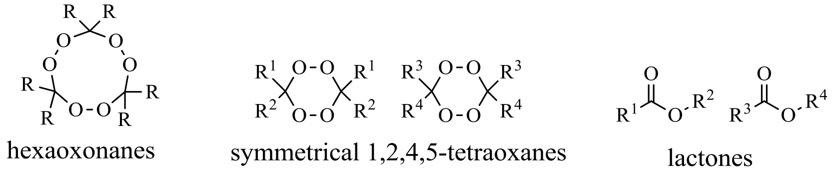

Figure 4: By-products in the acid catalysed peroxidation of ketones

2 Results and discussion

Our research focuses on synthesis of structurally diverse tetraoxanes under simple reaction conditions with emphasis on using hydrogen peroxide as a source of peroxide bond. Unsymmetrical 1,2,4,5-tetraoxanes can be synthesized by cyclization of *gem*-dihydroperoxide and ketone under acidic conditions but the reaction faces problems with formation of various side-products. Absence of formation of 1,2,4,5,7,8-hexaoxonanes and symmetrical tetraoxanes is of crutial importance as they are very difficult to separate from the desired product.

When searching for the best reaction conditions, we oriented our research towards finding of good combination of solvent, temperature and time in order to optimally activate cyclization to avoid formation of hexaoxonanes, while on the other hand, too activating conditions lead to decomposition of tetraoxanes into Beayer-Villiger products.

Optimization of reaction conditions were performed in reaction of cyclization of 4-phenylcylohexyl-1,1-diyl dihydroperoxide and 4-methylcyclohexanone as model substrates in the presence of one equivalent of HBF_4 (Scheme 2). Reaction of cyclization was studied in two solvents (1,1,1-trifluoroethanol - TFE, acetonitrile - MeCN) at different temperatures (0 °C, room temperature) and the outcome of the reaction was analysed after 5 minutes or 1 hour (Table 1). Performing reaction at room temperature for 1 hour resulted mainly in the formation of Baeyer-Villiger products in both solvents. Stopping reaction after 5 minutes at the same temperature in TFE still leads to lactones as major products. On the other hand, using less activating solvent MeCN results in good and selective formation of unsymmetrical tetraoxanes (52% yield). By lowering temperature to 0 °C, reaction system is deactivated and hexaoxonanes start to appear in the mixture of products especially when reaction is stopped after 5 minutes.

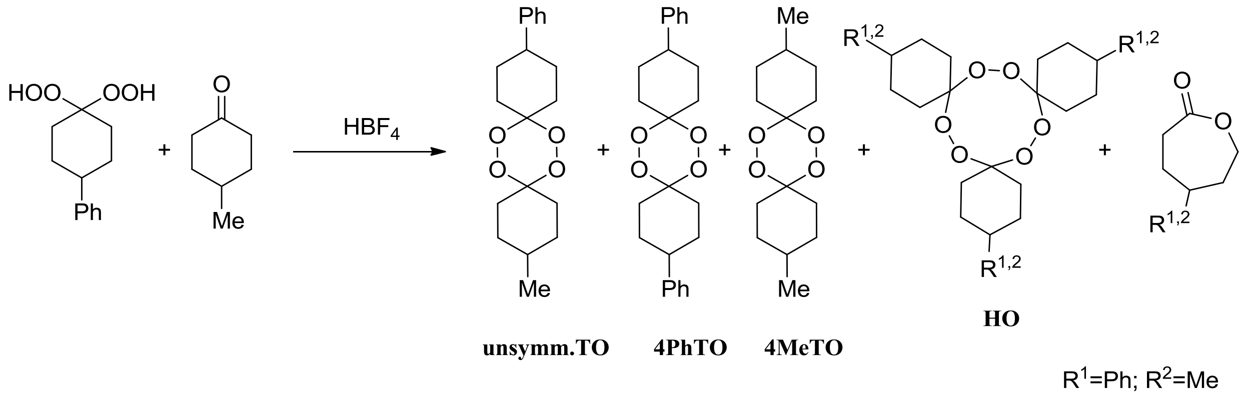

Scheme 2: Products that can be formed in the acid-catalysed cyclization of 4-phenylcylohexyl-1,1-diyl dihydroperoxide with 4-methylcyclohexanone.

Table 1: Distribution of products after the cyclization of 4-phenylcylohexyl-1,1-diyl dihydroperoxide with 4-methylcyclohexanone in different reaction conditions.

				Distribution of cyclic peroxides		
solvent	**t (min)**	**T (°C)**	**cyclic peroxides (%)[d]**	**unsymm.TO[a] (%)[e]**	**4PhTO[b] (%)[e]**	**HO[c] (%)[e]**
TFE	60	22	25	16	84	/
MeCN	60	22	19	53	47	/
TFE	5	22	28	29	71	/
MeCN	**5**	**22**	**52**	**100**	**/**	**/**
TFE	60	0	37	89	11	/
MeCN	**60**	**0**	**82**	**100**	**/**	**traces**
TFE	5	0	78	79	/	21
MeCN	5	0	71	56	/	44

[a] Unsymmetrical tetraoxane (3-methyl-12-phenyl-7,8,15.16-tetraoxadispiro[5.2.5.2]-hexadecane).

[b] Symmetrical tetraoxane (3,12-diphenyl-7,8,15.16-tetraoxadispiro[5.2.5.2]-hexadecane).

[c] Hexaoxonane.

[d] Isolated yield of the mixture of cyclic peroxides or pure compound after column chromatography.

[e] Distribution of cyclic peroxides was determined by NMR spectra of the mixture of cyclic peroxides after column chromatography.

Furthermore, we were interested in the effect of acid on the selectivity of formation of unsymmetrical tetraoxanes and experiments with different amount of acid (0,1 to 2 equivalents of HBF_4) were performed (

Table 2). As expected, less acidic conditions in MeCN promote formation of hexaoxonane. On the other hand, smaller amount of acid in reaction in TFE increases the yield of unsymmetrical tetraoxane and, interestingly, retains the selectivity. By increasing the quantity of acid in this reaction, formation of hexaoxonane is discouraged and the yield of unsymmetrical tetraoxane is reduced, while reaction had to be stopped after 5 min as longer reaction time would lead to preferential formation of lactones.

Table 2: The effect of acid on the cyclization of 4-phenylcylohexyl-1,1-diyl dihydroperoxide with 4-methylcyclohexanone.

					Distribution of cyclic peroxides		
equiv. HBF_4	**solvent**	**T (min)**	**T (°C)**	**cyclic peroxides (%)[a]**	**unsymm.TO (%)[b]**	**4PhTO (%)[b]**	**HO (%)[b]**
1	MeCN	5	RT	52	100	/	/
0,1	MeCN	5	RT	95	36	/	64
1	TFE	60	0	37	89	11	/
0,1	TFE	60	0	54	100	/	traces
1	TFE	5	0	78	79	/	21
2	TFE	5	0	41	100	/	traces

[a] Isolated yield of the mixture of cyclic peroxides or pure compound after column chromatography.

[b] Distribution of cyclic peroxides was determined by NMR spectra of the mixture of cyclic peroxides after column chromatography.

Results showed that TFE might be more appropriate solvent for general method of cyclization keeping in mind that no formation of hexaoxonane is preferential to a slightly higher yield of unsymmetrical tetraoxanes. Also less reactive starting materials would demand more activation so performing reaction in TFE at room temperature would increase yield of formation of unsymmetrical tetraoxanes. Taking all that into account, various unsymmetrical tetraoxanes were synthesized (Scheme 3). From the results we can summarize that we cannot use one set of reaction conditions for all substrates and instead for the selective conversion of substrates into unsymmetrical tetraoxanes reaction conditions should be modified based on reactivity of substrates.

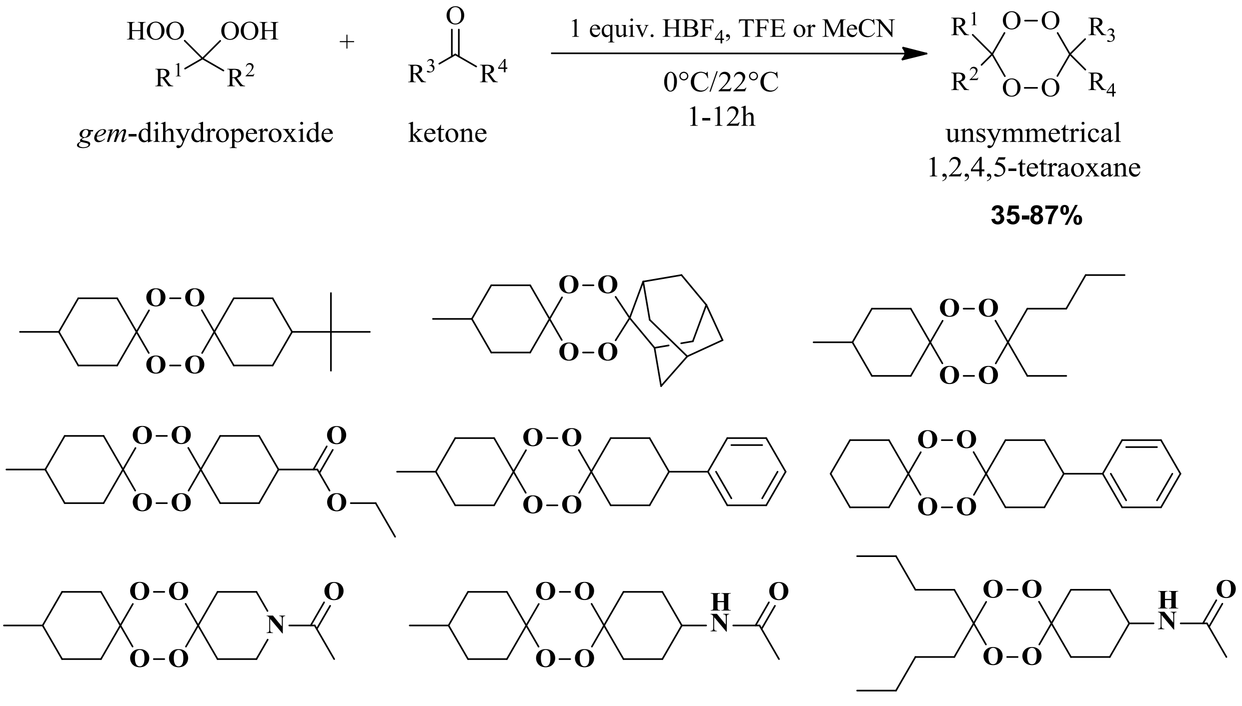

Scheme 3: Conversion of several *gem*-dihydroperoxides and ketones into unsymmetrical tetraoxanes (isolated yields are reported).

3 Conclusions

We have studied cyclization of *gem*-dihydroperoxides with carbonyl compound to deliver simple and selective method for synthesis of unsymmetrical 1,2,4,5-tetraoxanes. The effect of reaction conditions on the selectivity of reaction was studied and various unsymmetrical tetraoxanes were isolated. Due to different reactivity of *gem*-dihydroperoxides and ketones it is not possible to develop a general method for synthesis of unsymmetrical tetraoxanes, however, our study gives guidelines for predicting the optimal reaction conditions based on reactivity of substrates.

4 Acknowledgements

The authors are grateful to Slovenian Research Agency (Programme P1-0134 and Young Researcher Fellowship) for the financial support.

5 References

[1] Jung M, Kim H, Lee K, Park M. Naturally Occurring Peroxides with Biological Activities. Mini Reviews in Medicinal Chemistry 2003;3:159-65.

[2] Krishna S, Bustamante L, Haynes RK, Staines HM. Artemisinins: their growing importance in medicine. Trends in Pharmacological Sciences 2008;29:520-7.

[3] Anthony M, Burrows J, Duparc S, JMoehrle J, Wells T. The global pipeline of new medicines for the control and elimination of malaria. Malaria Journal 2012;11:316.

[4] Kumar N, Singh R, Rawat DS. Tetraoxanes: Synthetic and Medicinal Chemistry Perspective. Medicinal Research Reviews 2012;32:581-610.

[5] O'Neill PM, Amewu RK, Nixon GL, Bousejra ElGarah F, Mungthin M, Chadwick J, et al. Identification of a 1,2,4,5-Tetraoxane Antimalarial Drug-Development Candidate (RKA 182) with Superior Properties to the Semisynthetic Artemisinins. Angewandte Chemie International Edition 2010;49:5693-7.

[6] Flannery EL, Chatterjee AK, Winzeler EA. Antimalarial Drug Discovery: Approaches and Progress towards New Medicines. Nature reviews Microbiology 2013;11:849-62.

[7] Zmitek K, Zupan M, Iskra J. alpha-Substituted organic peroxides: synthetic strategies for a biologically important class of gem-dihydroperoxide and perketal derivatives. Organic & Biomolecular Chemistry 2007;5:3895-908.

[8] Zmitek K, Stavber S, Zupan M, Bonnet-Delpon D, Iskra J. Fluorinated alcohol directed formation of dispiro-1,2,4,5-tetraoxanes by hydrogen peroxide under acid conditions. Tetrahedron 2006;62:1479-84.

[9] Dong Y, Creek D, Chollet J, Matile H, Charman SA, Wittlin S, et al. Comparative Antimalarial Activities of Six Pairs of 1,2,4,5-Tetraoxanes (Peroxide Dimers) and 1,2,4,5,7,8-Hexaoxonanes (Peroxide Trimers). Antimicrobial Agents and Chemotherapy 2007;51:3033-5.

Selectivity in the Synthesis of Unsymmetrical tetraoxanes

Katarina Starkl[1,2], **Jernej Iskra**[1]
[1] Department of Physical and Organic Chemistry (K-3), Jožef Stefan Institute, Ljubljana, Slovenia
[2] Jožef Stefan International Postgraduate School, Ljubljana, Slovenia
katarina.starkl@ijs.si

Natural products containing peroxide groups exhibit broad spectrum of bioactivity. Unsymmetrical tetraoxanes are representatives of synthetic cyclic peroxides which were developed based on the structure of artemisinin, a natural cyclic peroxide used in first-line treatment for malaria and a promising antitumor, antiparasitic and antiviral agent. Tetraoxanes might exhibit enhanced antimalarial activity due to two peroxide groups in the molecule that are essential for bioactivity of cyclic peroxides. Chemical synthesis of unsymmetrical 1,2,4,5-tetraoxanes could be straightforward with acid-catalysed cyclization of *gem*-dihydroperoxide and ketone, however problems with formation of various side-products hampers their development. We have studied the reaction conditions in the cyclization of model substrates in order to develop a general method for synthesis of unsymmetrical tetraoxanes with an emphasis on selectivity. The method was adopted for the synthesis of various 1,2,4,5-tetraoxanes which will be evaluated for in-vitro antibacterial and antitumor activity.

IPSSC: Oligomerization properties of G-quadruplex structures with GC end groups

Blaž Tašič[a,b], Irena Drevenšek Olenik[b,c], Katarína Tlučková[d], Viktor Víglaský[d], Lea Spindler[e,b]

a Study programme Nanosciences and Nanotechnologies, Jozef Stefan International Postgraduate School, Jamova 39, 1000 Ljubljana, Slovenia

b Department of Complex Matter, Jozef Stefan Institute, Jamova 39, 1000 Ljubljana, Slovenia

c Faculty of Mathematics and Physics, University of Ljubljana, Jadranska 19, 1000 Ljubljana, Slovenia

d Department of Biochemistry, Institute of Chemistry, Faculty of Sciences, P. J. Safarik University, Moyzesova 11, Kosice, Slovakia

e Faculty of Mechanical Engineering, University of Maribor, Smetanova 17, 2000 Maribor, Slovenia

blaz.tasic@gmail.com

Abstract. Guanine-rich DNA sequences have the ability to grow into long nanowires made up of guanine (G:G:G:G) tetrads. These so called G-wires can be deposited on solid substrates and are due to their mechanical and thermal stability interesting candidates for molecular electronic devices. Our recent investigation showed that the sequence 5'-GCGGTG$_4$TGGCG-3' forms G-wires via formation of (G:C:G:C) tetrads [1]. To obtain more insight into the related self-assembly mechanism, we performed a comparative study of assembly properties of four analogous oligonucleotides: the above denoted one and the three similar ones with either 5', 3' or both GC-ends missing. Circular dichroism (CD) and polyacrylamide gel electrophoresis (PAGE) were used to investigate the structure, thermal stability, ageing, and the effect of adding different cations to the formation of G-quadruplex structures and to their oligomerization properties.

Keywords: G-quadruplex, Circular Dichroism, Polyacrylamide Gel Electrophoresis, Nanowire, G-wires

1 Introduction

When deposited on solid substrates, guanosine monophospate and guanine-rich DNA sequences have the ability to grow into long nanowires made up of guanine (G:G:G:G) tetrads [2-4]. These so called G-wires are due to their mechanical and thermal stability very suitable candidates for applications in optoelectronic, electronic, electromechanical and electrochemical devices.

To avoid discontinuities in the G-wire formation, it is essential that the DNA quadruplex stem remains uninterrupted. One possibility to achieve this aim is to use G-rich DNA sequences with CG "sticky-end" overhangs. Previous studies [5,6] showed that sequences with the structure d(GCGGXGGAT) (where X was either T, TT, A, or TC) first assembled into a dimer by two sequences forming a bimolecular quadruplex linked by the (G:G:G:G) tetrads. In the next step, two such dimers growed into a multimer by their CG overhangs arranging into the (G:C:G:C) tetrads, which established a link in the middle of the two dimers.

For our study we selected the sequence **GC**G$_2$TG$_4$TG$_2$**CG** with CG overhangs at both ends. This sequence forms long nanowires when deposited onto a mica substrate [7]. The growth of these G-wires is expected to be stimulated by the formation of (G:C:G:C) linking tetrads at both, 5' and 3', ends. The proposed basic structure for the selected sequence is a bimolecular quadruplex as depicted in Scheme I. To more clearly elucidate the role of CG ends, three control sequences were selected: 5'-GCG$_2$TG$_4$TG$_2$ (Scheme II), G$_2$TG$_4$TG$_2$CG-3' and G$_2$TG$_4$TG$_2$.

Preliminary measurements by UV-Vis absorption spectrometry confirmed the formation of G-quadruplexes from all four sequences in 100 mM NaCl and 10 mM NaPi solutions. Dynamic light scattering (DLS) further revealed that G-wires are indeed formed at suitable conditions [1].

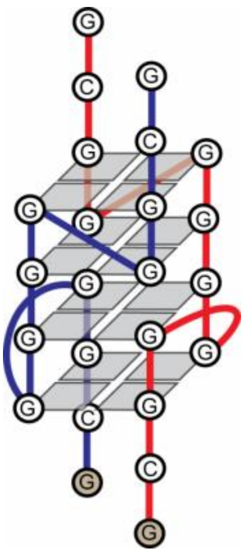

I GCG$_2$TG$_4$TG$_2$CG

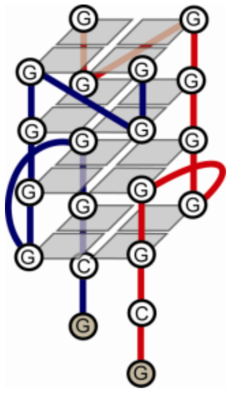

II 5'-GCG$_2$TG$_4$TG$_2$

To resolve additional details of the above described oligomerization process, we used polyacrylamide gel electrophoresis to investigate G-wire growth under various solution conditions (different oligonucleotide concentration, added salt, etc.). Besides this, we used circular dichroism to determine thermal stability of the investigated structures.

2 Methods and Materials

The oligonucleotides used in our experiments were: d(**GC**GGTG$_4$TGG**CG**), d(**GC**GGTG$_4$TGG), d(GGTG$_4$TGG**CG**) and d(GGTG$_4$TGG). All oligonucleotides were purchased from Eurogentec, Belgium, as 4 mM water solutions. They were at first purified on a Sephadex-15 coloumn and were subsequently diluted in 100 mM NaCl solution buffered with 10 mM sodium phosphate buffer (pH = 6.8).

Native polyacrylamide gel electrophoresis (PAGE) was run in a temperature-controlled vertical electrophoretic apparatus (Z375039-1EA; Sigma–Aldrich, San Francisco, CA) at 10 °C with 16 % of acrylamid in gel. Electrophoreses were run at 80 V for 3 - 5 hours. For staining Stains-All dye (Sigma-Aldrich) was used.

Circular dichroism melting curves were obtaind with spectrometer Jasco J-810. The heating rate was 1 °C per minute. Melting curves were recorded at 263 nm.

3 Results and Discussion

As can be resolved in *Figure 1*, all sequences except **GC**GGTG$_4$TGG folded differently before and after they were purified on a Sephadex 15 coloumn. From purified samples the sequence **GC**G$_2$TG$_4$TG$_2$**CG** (lane 1) forms two structures, which can be most probably attributed to a single quadruplex and to two quadruplexes linked by the (G:C:G:C) tetrads. The sequence **GC**G$_2$TG$_4$TG$_2$ (lane 3) is characterised by a large smeared band that could result from two different structures in rapid exchange and one hardly seen band higher above that represents 4 stacked quadruplexes. We observed only one strong band for G$_2$TG$_4$TG$_2$**CG** (lane 5), which we attribute to two stacked quadruplexes. The sequence G$_2$TG$_4$TG$_2$ (lane 7) shows a ladder effect which is typical for a long structure. We therefore conclude that this sequence definitely forms long G-wires.

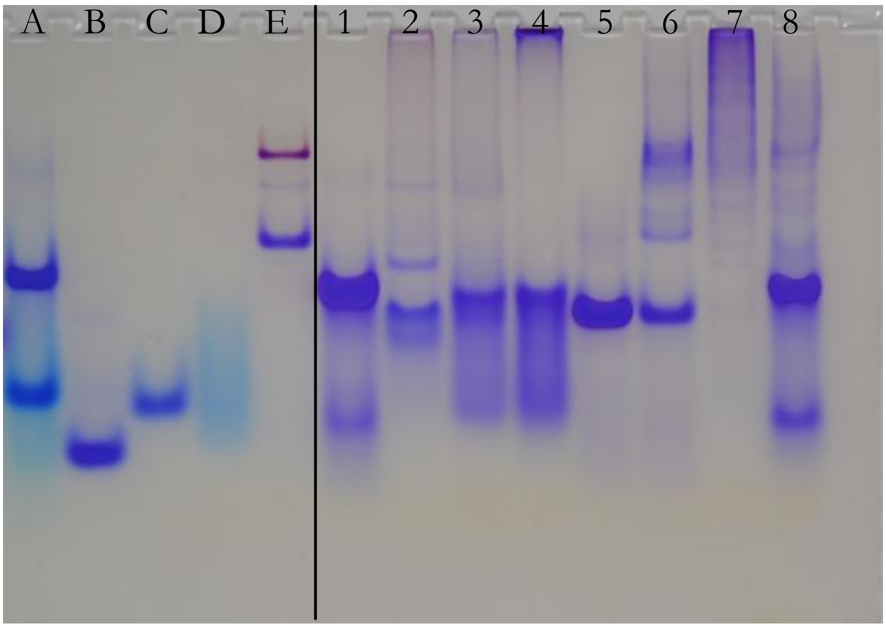

Figure 1: References *A) AC18 + AC36, B)* $[G_3T_2A]_3G_3$, *C)TBA, D)* $[G_3T_2]_3G_3$, *E) HIV*

$\mathbf{GC}G_2TG_4TG_2\mathbf{CG}$: *1) purified, 2) not purified*

$\mathbf{GC}G_2TG_4TG_2$: *3) purified, 4) not purified*

$G_2TG_4TG_2\mathbf{CG}$: *5) purified, 6) not purified*

$G_2TG_4TG_2$: *7) purified, 8) not purified*

3.1 Melting temperatures

With circular dichroism we obtained melting temperatures of different structures. In accordance with the PAGE results (*Figure 1*), which show that the sequences $\mathbf{GC}G_2TG_4TG_2\mathbf{CG}$ and $G_2TG_4TG_2\mathbf{CG}$ form only a single structure, the associated CD spectra exhibit only one melting temperature (*Figure 2, Figure 4*).

In contrast, the sequence $\mathbf{GC}G_2TG_4TG_2$ (*Figure 3*) exhibits two melting temperatures during heating and only one melting temperature during cooling (performed immediately after heating). This is because larger aggregates cannot form in such a short time.

The sequence $G_2TG_4TG_2$ (*Figure 5*) shows two melting processes at relatively high temperatures (T_{m1} = 66°C, T_{m2} = 82°C). This sequence is the longest and it most probably forms G-wires. When T_m is measured at cooling, only one melting temperature (T_m = 34°C) is obtained also in this case. This is the T_m of single quadruplexes. If we wait for a longer time (3 days), we observe a mixture of less and more stable structures (three melting temperatures).

The thermal stability of basic quadruplex structures (T_{m1}) decreases in the order **GC**GGTG$_4$TGG**CG** > **GC**GGTG$_4$TGG > GGTG$_4$TGG**CG** > G$_2$TG$_4$TG$_2$. These results indicate that GC-ends significantly stabilise the basic quadruplex stem.

Figure 2: GCGGTG$_4$TGG**CG**

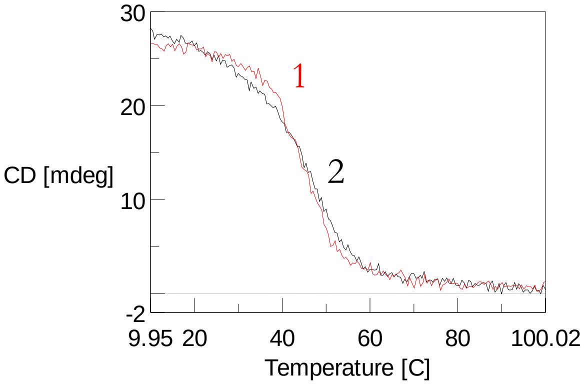

Figure 3: GCGGTG$_4$TGG

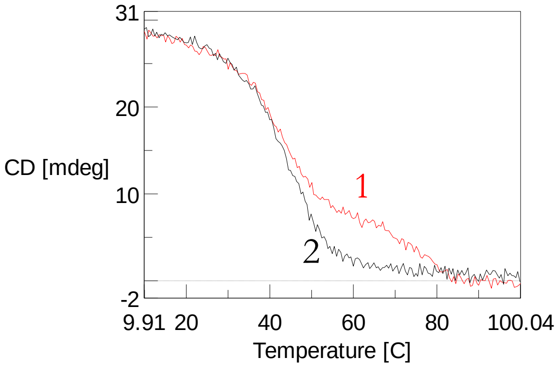

Figure 4: GGTG$_4$TGG**CG**

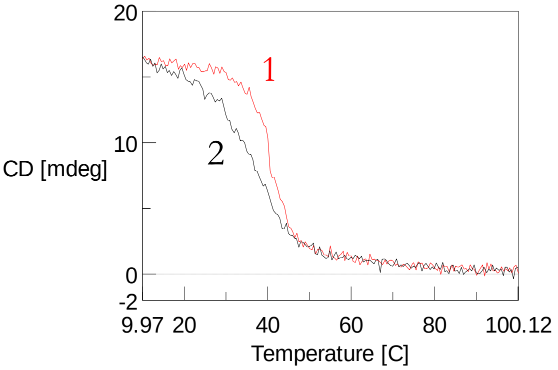

Figure 5: G$_2$TG$_4$TG$_2$

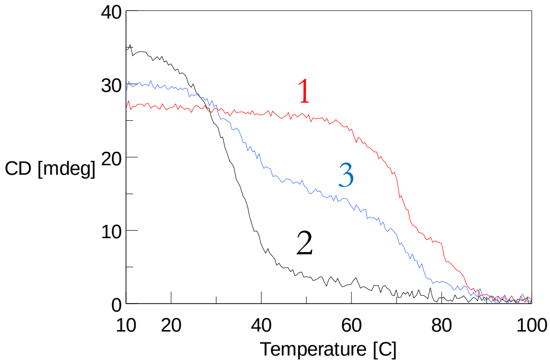

*1: Heating (**red**), 2: Cooling (**black**), 3: Second heating after 3 days (**blue**)*

3.2 Ageing

In *Figure 6* the growth of sequence G$_2$TG$_4$TG$_2$ by the sample aging is presented. The sample was heated at high concentration (c = 1 mM) and the buffer was added just before the measurement. When analogous measurement was repeated at a lower concentration of the oligonucleotide (c = 0.06 mM), different results were obtained (*Figure 7*), i.e. the growth of G-wires was much slower.

The sequence GGTG$_4$TGG**CG** forms long structures only at high concentration, but these structures are not stable for a long time.

The other two sequences (**GC**GGTG$_4$TGG**CG** and **GC**GGTG$_4$TGG) after three days formed the same structures regardless of their concentration.

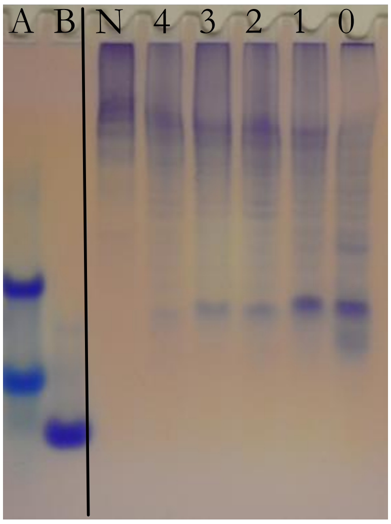

Figure 6: Ageing of $G_2TG_4TG_2$.

A) AC18+AC36, B) $[G_3T_2A]_3G_3$*, N) Not heated, 4) 4 days old sample, 3) 3 days old sample, 2) 2 days old sample, 1) 1 day old sample, 0) 0 days old sample.*

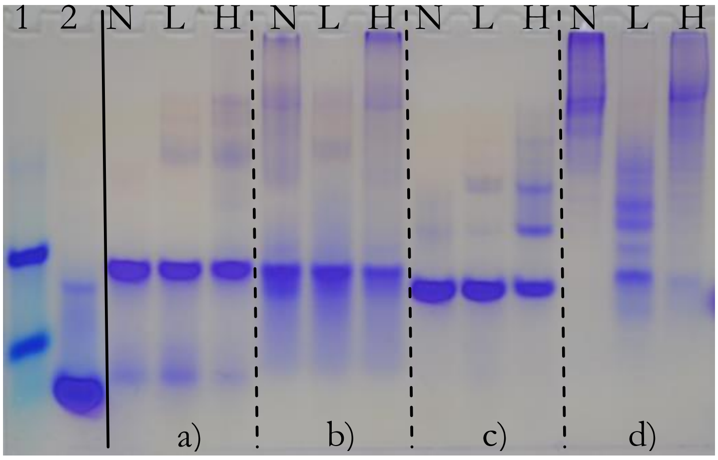

Figure 7: Ageing in High/Low concentration of oligonucleotides.

1) AC18+AC36, 2) $[G_3T_2A]_3G_3$*, a)* **GC**$G_2TG_4TG_2$**CG**, b) **GC**$G_2TG_4TG_2$, c) $G_2TG_4TG_2$**CG**, d) $G_2TG_4TG_2$*; N – not heated, L – heated at low concentration, H – heated at high concentration.*
All samples are 3 days old.

3.3 Effect of adding cations

We added different cations at high concentration (c = 1 M) to our samples (Fig. 8, 9, 10, 11). For a specific sequence, all CD curves had the same shape regardless of the added ion species. From this it can be concluded that the same quadruplex structure forms independent of the type of cations. The cations thermally stabilized the investigated G-quadruplexes in the following order **$K^+ > Na^+ > Li^+$**, which agrees with the well-established quadruplex-stabilising cation series.

Figure 8: GCG$_2$TG$_4$TG$_2$**CG**

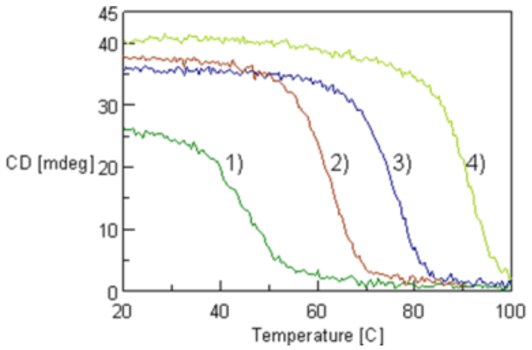

Figure 9: GCG$_2$TG$_4$TG$_2$

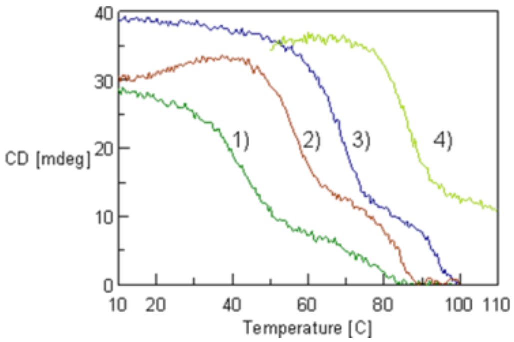

Figure 10: G$_2$TG$_4$TG$_2$**CG**

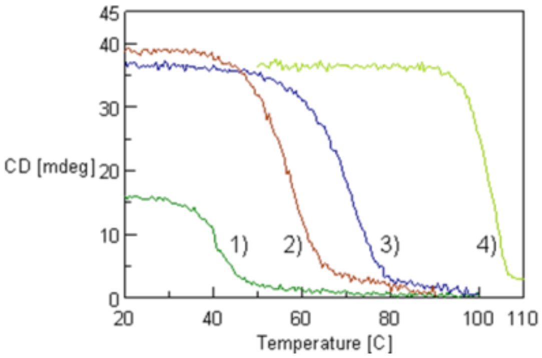

Figure 11: G$_2$TG$_4$TG$_2$

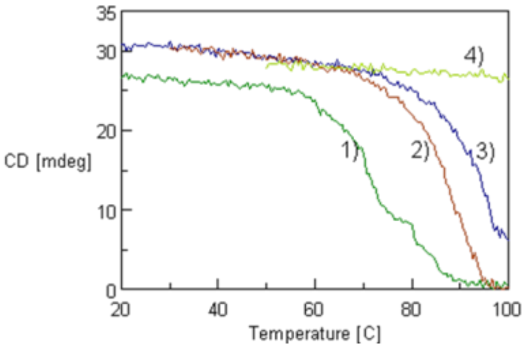

1) 100 mM NaCl, 2) 1 M LiCl + 100 mM NaCl, 3) 1 M NaCl, 4) 1 M KCl + 100 mM NaCl

4 Conclusion

The results of our CD measurements show that the oligonucleotides with GC-ends are more thermally stable than those without GC-ends. They also reveal that adding monovalent cations notably increases the thermal stability of the quadruplex structures. Both, the CD melting curves and the PAGE analysis, confirmed formation of multimer structures for the sequences GCG$_2$TG$_4$TG$_2$ and G$_2$TG$_4$TG$_2$. Surprisingly, no G-wires in solution were observed for the sequence GCG$_2$TG$_4$TG$_2$CG, although this sequence forms extended G-wire networks on mica substrates. This finding indicates that in addition to the quadruplex stacking and GC linking processes that are present already in the solution, G-wire formation may be facilitated also by the surface interactions taking place during solution deposition.

References:

[1] T. Ilc, P. Šket, J. Plavec, M. Webba da Silva, I. Drevenšek-Olenik, L. Spindler, J. Phys. Chem. C **117**, 23208–23215 (2013).
[2] K. Kunstelj, F. Federiconi, L. Spindler, I. Drevensek-Olenik, Colloids and Surfaces B: Biointerfaces **59**, 120-127 (2007).
[3] J. Vesenka, D. Bagg, A. Wolff, A. Reichert, R. Moeller, W. Fritzsche, Colloids And Surfaces B-Biointerfaces **58**, 256-263 (2007).
[4] N. Borovok, N. Iram, D. Zikich, J. Ghabboun, GI Livshits, D. Porath, A. Kotlyar, Nucleic Acids Research **36**, 5050-5060 (2008).
[5] M. Webba da Silva, Biochemistry **42**, 14356-14365 (2003).
[6] J-L. Mergny, A. De Cian, S. Amrane, M. Webba da Silva, Nucleic Acids Res. **34**, 2386-2397 (2006).
[7] T. Troha, "Površinsko urejanje z gvaninom bogatih sekvenc DNK", diploma work, 2013.

For wider interest

DNA sequences that contain a lot of guanosine (G) have the ability to form special four-stranded macromolecular structures known as G-quadruplexes. When deposited on solid substrates and also in aqueous solutions, G-quadruplexes can associate into long G-wires, which have promising properties for applications in molecular electronics devices. Consequently there exists a broad interest to obtain understanding and control of the G-wire formation process. We performed a systematic investigation of the G-wire formation in solutions of four very similar G-rich DNA oligonucleotides and discovered that a presence/absence of the GC end groups strongly affects the wire growth. We also investigated the effect of various cations on the stability of the formed assemblies and found that potassium acts as the most efficient stabilization agent.

The optimization of cleaning pre-treatment of aluminium alloy AA 7075

Urša Tiringer[1,2]
[1] Department of Physical and Organic Chemistry, Jožef Stefan Institute, Ljubljana, Slovenia [2] Jožef Stefan International Postgraduate School, Ljubljana, Slovenia
ursa.tiringer@ijs.si

Ingrid Milošev[1]
[1] Department of Physical and Organic Chemistry, Jožef Stefan Institute, Ljubljana, Slovenia ingrid.milosev@ijs.si

Abstract. Aluminum and its alloys belong to light metals and are most commonly used in transportation industry. Present work aims to study the effect of cleaning of aluminium alloy of series AA 7075 with two different alkaline cleaners, first based on 0.01 M NaOH and exposed to 50% HNO_3 and second supplied by SurTec which is based on phosphates. According to the results obtained by electrochemical method, the cleaner based on NaOH and HNO_3 causes the passivation of AA 7075, while the potentiodynamic curve of surface cleaned with SurTec is similar to pure aluminium. XPS results show that both discussed cleaners remove contamination quite effectively. High resolution spectrum of Al 2p shows that in all samples aluminium is mostly present in its oxide state. Moreover, after both cleaning, with NaOH/HNO_3 and SurTec, the surface of AA 7075 becames almost superhydrophilic, while the untreated sample is hydrophilic.

Keywords: aluminium, aluminium alloy, surface cleaning, alkaline cleaners

1 Introduction

Reduction of CO2 emission is an important goal set by the directives of the European Union. One of the possible ways to achieve this goal is to use light alloys in transportation industry. Aluminum and its alloys belong to the group of light metals and are most commonly used in transport industry such are aircraft industry, automotive industry, train industry and marine industry.

Despite the fact that aluminum resists corrosion well, its alloys may not be corrosion resistant in various environments. Chromate conversion coatings have been effective as aluminium protection against corrosion for many years. Nowadays their use is becaming increasingly limited because of their toxicity. Many studies have been focused on the development of technologies alternative to chromates. Before any kind of surface treatment, it is necessary to perform a proper cleaning of the surface which will be treated. Cleaning of aluminum is necessary for hygiene (in food industry), for maintenance (for buildings and transport equipment) and for quality control. The goal of cleaning is to remove inorganic and organic residues that are present on the surface of aluminum and its alloys. There are three issues that should be controlled during cleaning and are labeled and described below:

- The chemical issue; cleaning agent should not attack the substrate
- The physical issue; dirt is removed from the surface by modifying its surface tension
- The mechanical issue; dirt which is insoluble in cleaning agent can be removed from the surface by brushing or by high-pressure water jets.

Most cleaning agents consist of acidic or alkaline media which have different functions. They can have a role of pickling agents, detergents, degreasing agents or of corrosion inhibitors. Suitable cleaning agent has to be compatible with aluminum or its alloys, nontoxic for human health and nonpolluting for environment. As aluminum and its alloys are amphoteric, they can be attacked by acids and by bases. In highly alkaline medium the oxide film is formed which is difficult to modify, but, on the other hand, use of alkaline cleaner increases the corrosion resistance of these materials. Products based on acids form stable and insoluble salt with aluminum and alloys, but do not increase their corrosion resistance.

Our goal is to optimize the cleaning process of aluminum alloy AA 7075 by finding a proper cleaning agent. The original composition (in atomic percent) of aluminum alloy AA 7075 is the following: Zn (5.6-6.1), Mg (2.1-2.5), Cu (1.2-1.6) and less than half percent of Si, Fe, Mn, Ti, Cr and other metals. In our research we compared two different alkaline cleaners, the first was based on 0.01 M NaOH including desmutting process and the second was manufactured by SurTec and based on phosphates.

2 Material and methods

2.1 Preparation of the samples

Samples of aluminium alloy AA 7075 were ground using 2400 and 4000-grid SiC emery papers, ultrasonically cleaned in ethanol for 5 minutes, rinsed with deionized water and dried with a stream of N_2. Samples of AA 7075 were divided into three groups:

- Followed by the first was immersed in the 0.01 M NaOH for 3 minutes and than in 50% HNO_3 for 30 seconds.
- The second was cleaned using SurTec product, which was formed by combination of 3% SurTec132 liquid recyclable builder and of 0.5% SurTec089 recyclable detergent component. The sample was immersed in the mixture for three minutes at 40°C.
- The third was untreated sample.

The comparison of cleaners was carried out by electrochemical polarization method, X-ray photoelectron spectroscopy, profilometer, tenziometer and scanning electron microscopy.

2.2 Electrochemical measurements

Electrochemical measurement were performed in 0.1 M NaCl at room temperature. An Autolab corrosion cell with a volume 0.350 L was used. The working electrode was embedded in a Teflon holder with exposed area 0.87 cm^2. Graphite electrode served as a counter electrode and saturated calomel electrode (SCE) was a reference electrode (E = 0.214 V vs. standard hydrogen electrode, SHE). After 1 h stabilization at open circuit potential (OCP) measurements were performed in the following order: linear polarization, ±10 mV versus OCP, using a scan rate of 0.1 mV/s and potentiodynamic measurements starting from -250 mV vs. OCP up to -0.5 V using a scan rate of 1 mV/s. Experiments were repeated in triplicate and representative measurement is presented in graphical form.

2.3 X ray photoelectron spectroscopy (XPS)

The X-ray photoelectron spectroscopy analysis was carried out on the PHI-TFA XPS spectrometer (Physical Electronics Inc.). The vacuum during the XPS analyses was in the range of 10^{-9} mbar. The analyzed area was 0.4 mm in diameter and the analyzed depth was about 3 - 5 nm. Sample surfaces were excited by X-ray radiation from monochromatic Al source at photon energy of 1486.6 eV. Spectra were analyzed by a Multipak software, version 8.0 (Physical Electronics Inc company).

Prior and after the immersion test the morphology, topography and contact angle of the surface were examined.

2.4 Measurement of surface morphology, topography and contact angle

Scanning electron microscopy (SEM) images were taken with JEOL JSM-7600F microscope equipped with chemical analysis (EDXS).

A profilometer, model Bruker DektakXT, was employed for analysis of surface topography. The instrument has a lateral resolution of 1 μm and vertical resolution 5 nm. It measures the surface profile in one direction. Measurements were performed at 1 mm^2 spot size on the sample. The data were processed with TalyMap Gold 6.2 software. 3-D surface topography and calculation of the mean surface roughness (S_a) were obtained.

The contact angles (Θ) were measured using the tensiometer Krüss DSA 20 (Krüss GmbH, Hamburg, Germany). A Drop-shape-analysis software enables the fitting of the image of the deionized water drop on the sample surface and allows a precise determination of the contact angle value. Each contact angle value is the mean of at least three measurements made on different positions of the same sample.

3 Results and discussion

Potentiodynamic curves for untreated and samples cleaned with NaOH/HNO3 and with Surtec phosphate cleaner are presented in Figure 1.

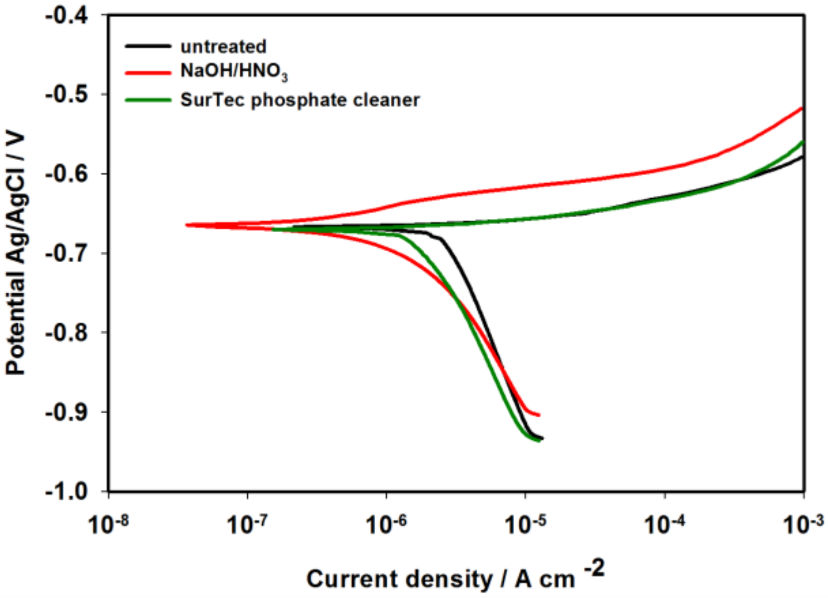

Figure 1: Polarization curves of AA 7075 samples cleaned with NaOH/HNO$_3$, SurTec phosphate cleaner and of untreated AA 7075 sample. Curves were recorded in 0.1 M NaCl.

According to the results obtained by electrochemical method, the cleaner based on NaOH and HNO$_3$ causes the passivation of AA 7075, while the potentiodynamic curve of surface cleaned with SurTec is similar to the curve of pure aluminium.

The concentration of elements obtained by X-ray photoelectron spectroscopy after various surface treatments are presented in Figure 2.

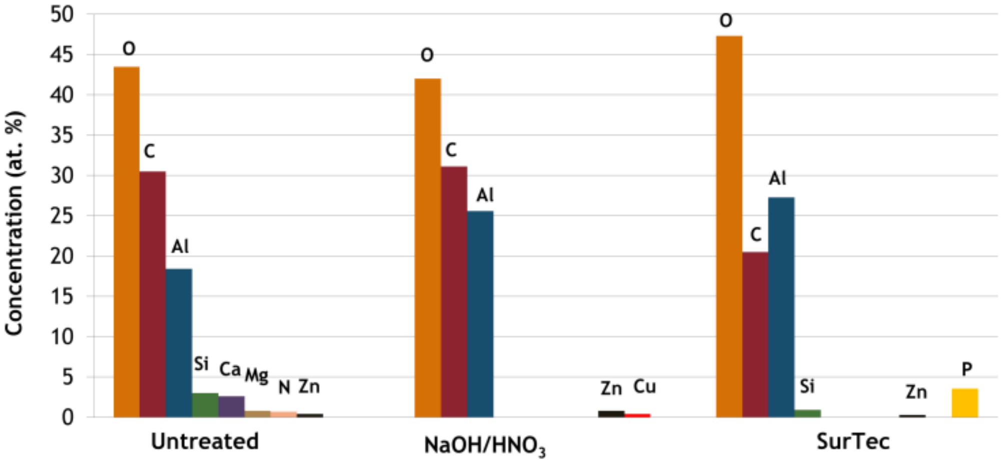

Figure 2: The concentration of elements obtained by XPS after various surface treatments: untreated, exposed to 0.01 M NaOH and HNO_3 and exposed to SurTec cleaner.

Results obtained by XPS technique show that carbon and nitrogen contaminations are reduced by cleaning. At the same time oxygen and aluminium content increased and alloying elements Mg and Si are removed. After using NaOH and HNO_3 the content of copper increased while after using SurTec cleaner the content of phosphorus increased.

Aluminium, which is the major element in alloy AA 7075, was interpreted in details, with high resolution spectra-qualitative analysis and fitting-quantitative analysis. Figure 3 presents XPS high resolution spectra of Al 2p.

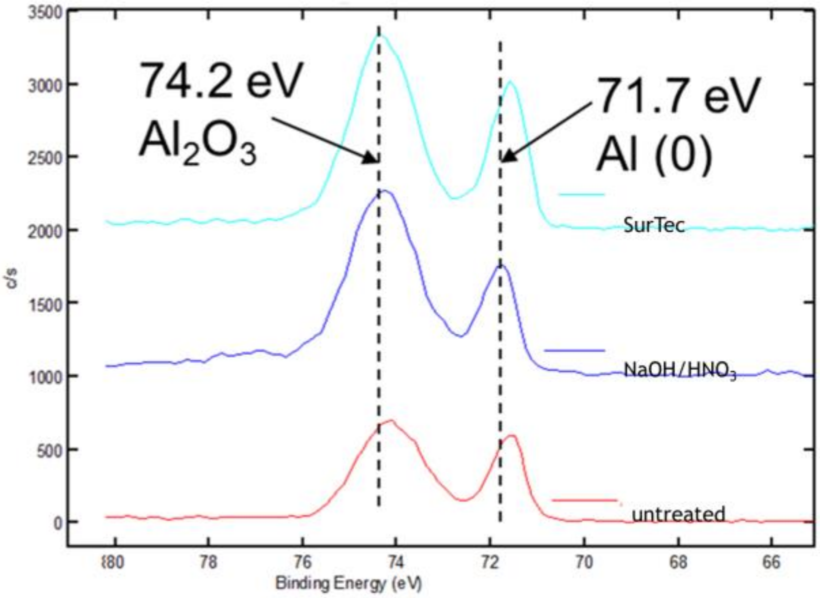

Figure 3: High resolution spectra of Al 2p obtained by XPS technique show the formation of aluminium oxide on differently cleaned samples.

As it is seen from Figure 3, two peaks of aluminum were detected on all three samples. One of them corresponds to energy of 74.2 eV, which belongs to oxide state of aluminum, and other of energy 71.7 eV, which belongs to elemental (metallic) state of aluminum.

Top view of profiles obtained by profilometer and values of surface roughness (S_a) of untreated sample, sample cleaned with NaOH and HNO_3 and with SurTec cleaner are presented in Figure 4. The colouring is according to the scale on the right which spans in the +- 1.5 μm. Image spot size is 1 mm x 1mm range.

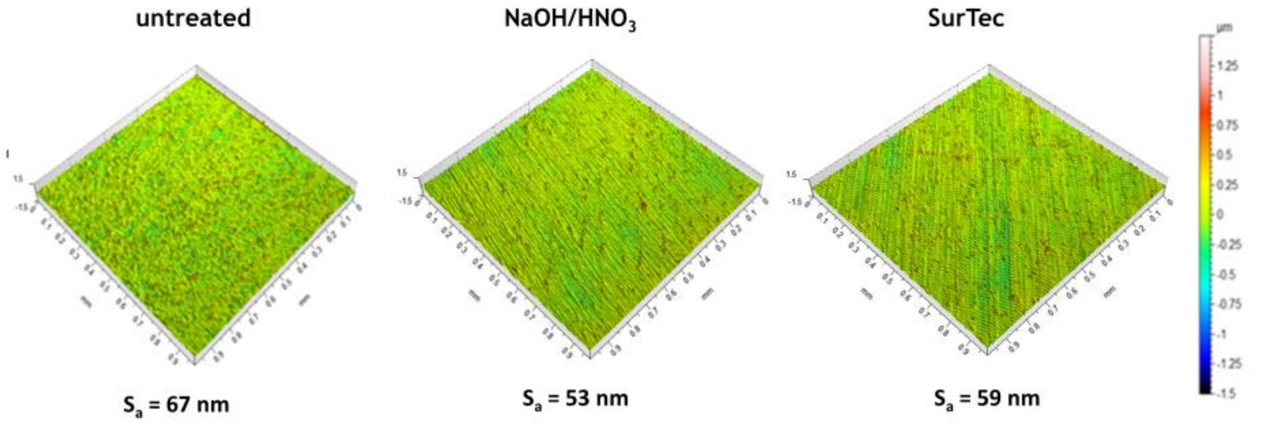

Figure 4: Top view of profiles obtained by profilometer and values of surface roughness (S_a) of untreated sample, sample cleaned with NaOH and HNO_3 and with SurTec cleaner.

As it is seen from Figure 4 images and surface rougness obtained by profilometer do not indicate the difference in surface topography of of untreated sample, sample cleaned with NaOH and HNO_3 and with SurTec cleaner.

SEM images of the surface cleaned with SurTec cleaner is presented in Figure 5.

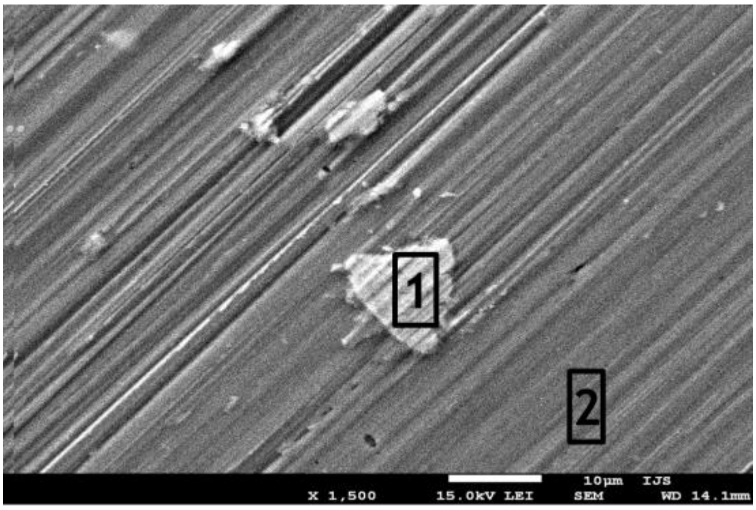

Figure 5: SEM analysis of sample AA 7075 cleaned with SurTec.

EDX analysis which is carried out at different locations at the treated sample AA 7075 as denoted in Figure 5 are presented in Table 1.

Table 1: EDX analysis carried out at different locations at the treated sample as denoted in Fig. 5.

[at.%]	**Al**	**Zn**	**Mg**	**O**	**Fe**	**Cu**
Spectrum						
1	82.4	3.3	2.3	5.3	1.9	4.8
2	94.6	2.5	8.9	/	/	/
δ	8.6	0.57	4.67	/	/	/

Images of water drops on the surface and values of contact angles (CA) of untreated sample, cleaned with NaOH and HNO_3 and with SurTec cleaner, are presented in Figure 6.

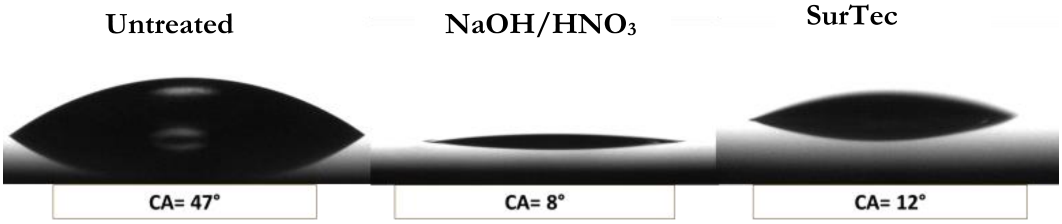

Figure 6: Images of water drops on the surface after different treatment and the values of contact angles.

After cleaning with NaOH/HNO_3 and with SurTec cleaner, the surface of aluminum alloy AA 7075 becomes almost superhydrophilic because the contact angle in this case is less than 10°. The surface of untreated sample is hydrophilic. The contact angle in this case is 47°.

4 Conclusions

According to the results obtained by electrochemical method the cleaner based on NaOH and HNO_3 causes the passivation of AA 7075, while the potentiodynamic curve of surface cleaned with SurTec is similar to the curve of pure aluminum.

Results obtained by XPS technique show that carbon contamination is reduced by cleaning. At the same time oxygen and aluminum content increased and alloying elements Mg and Si are removed. After using NaOH and HNO_3 the content of copper increased. After using SurTec cleaner the content of phosphorus increased. High resolution spectrum of Al 2p shows that in all samples aluminum is mostly present in its oxide state. Energy of 74.2 eV denotes to the oxide state of aluminum and of energy 71.7 eV, elemental aluminum.

Images and surface roughness obtained by profilometer do not indicate the difference in surfaces topography of differently treated samples.

SEM image shows that the surface of AA 7075 cleaned with SurTec in addition to aluminum consists of alloying elements zinc, magnesium, iron and copper, while inclusion (1) is probably zinc oxide.

After cleaning with NaOH/HNO_3 and with SurTec cleaner the surface of aluminum alloy AA 7075 becomes almost superhydrophilic (CA≤10°), while the untreated is hydrophilic (CA = 47 °).References:

References:

[1]

[2] I. H. Witten and E. Frank. *Data Mining: Practical machine learning tools and techniques, 2nd Edition*. Morgan Kaufmann, 2005.

[3] D. Petelin, J. Kocijan. Evolving Gaussian process models. In *Proceedings of the IEEE Symposium Series on Computational Intelligence 2011*, Paris, France, 2011.

[4] IPSSC submission form. 5th Jožef Stefan International Postgraduate School Student's Conference. http:// ipssc.mps.si/submission.asp, 2013

[5] J. R. Quinlan. Improved use of continuous attributes in C4.5. *Journal of Artificial Intelligence Research*, 4(1):77-90, 1996

[6] I. H. Witten and E. Frank. *Data Mining: Practical machine learning tools and techniques, 2nd Edition*. Morgan Kaufmann, 2005.

[7] D. Petelin, J. Kocijan. Evolving Gaussian process models. In *Proceedings of the IEEE Symposium Series on Computational Intelligence 2011*, Paris, France, 2011.

[8] IPSSC submission form. 5th Jožef Stefan International Postgraduate School Student's Conference. http:// ipssc.mps.si/submission.asp, 2013

Cobalt-Platinum alloy nanostructures as potential candidates for Racetrack Magnetic Data Storage Devices

Muhammad Shahid Arshad[1,2], Darja Pecko[1,2], Janez Zavasnik[3], Saso Sturm[1], Spomenka Kobe[1,4], Kristina Žužek Rožman[1]

1 Department for Nanostructured materials K7, Jozef Stefan Institute, Ljubljana, Slovenia
2 Jožef Stefan International Postgraduate School, Ljubljana, Slovenia
3 Centre for Electron Microscopy and Microanalysis (CEMM), Ljubljana, Slovenia
4 Center of Excellence on Nanoscience and Nanotechnology (CENN Nanocenter), Ljubljana, Slovenia
shahid.arshad@ijs.si

Abstract. Magnetic hard disk drives have been the prime repository of digital data for more than half a century. Over this period of time, the area of one magnetic bit, use to store information has decreased in size by about around nine order to magnitudes; it is now so tiny that it is reaching fundamental limit that are difficult or too expensive to overcome. A number of alternatives to the magnetic disk drive have been suggested. Among them racetrack memory devices seems to be potential candidates and close to the realization. Such devices are based on magnetic nanowires with magnetic domains which can be move with electrical current. In this article we will present the possibilities to produce nanowires which can be use in racetrack memory devices and we will also present the methods to manipulate magnetic domains in nanowires.

Keywords: Magnetic nanowires, Racetrack memory devices, Magnetic Domains

1 Introduction

Co-based alloys are integral part of modern magnetic recording media such as hard disk drive (HDD) due to their excellent magnetic properties. Alloying Co with metals like Pt enhances its intrinsic magnetic properties such as magnetocrystalline anisotropy. In addition it shows excellent chemical stability, higher coercivity and resistance against corrosion which makes such alloys suitable candidates for magnetic data storage devices. Due to size-confinement-trend in magnetic storage devices, it is reasonable to expect that Co-Pt alloy nanostructures such as nanowires (NWs) and nanotubes (NTs) would replace their counterparts in future. One of such ideas are racetrack memory devices, where information is stored in the form of magnetic domains with opposite magnetization along the length of the nanowires. One of the fascinating point of such devices is domains in nanowires can move forward or backward direction depending on current direction. Many researcher believes that such devices have potential to keep the Moore's law going and big IT companies like IBM are funding for research on racetrack memory devices. [1] Main features of such devices are enlisted below

1. Non-volatile (information remains stored even if there is no power, such as HDD and flash)
2. Higher Density (upto 10x information in comparison to HDD can be stored)
3. Super Speed (reading and writing of information would be equivalent or higher than SRAM)
4. Universal Memory devices (such devices can replace all type of memory devices such as SRAM, DRAM and flash memory)

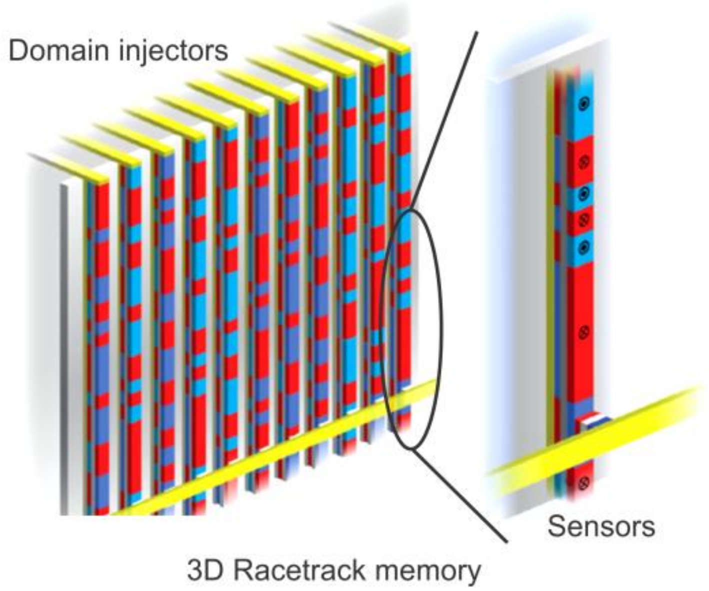

Figure 1: Schematic of Racetrack memory devices showing working principle of device. After [2]

For such devices to function properly it is necessary to have 1) magnetic domains with opposite magnetization as shown by red and blue boxes in Fig.1 and 2) it is also important to have pinning sites for the domains to manipulate them efficiently. In the present work, the Co-Pt nanostructures have been synthesized into polycarbonate (PC) as well as anodic alumina oxide (AAO) membranes with diameter range from 200-50 nm. We have studied the magnetic domains in such Co-Pt nanowires and investigated the manipulation of domains. We have utilized micromagnetic simulations (NMAG) to understand magnetization reversal in such nanowires. Due to the page limitation and to make the text more fluent we will focus on results which are mainly concerned here. For further details we suggest readers to read our published articles.

2 Results and Discussions

We will present three main concepts to produce and manipulate magnetic domains in Co-Pt nanowires in the following

I. Periodic Magnetic Domains in Co-Pt Nanowires

As-deposited Co-Pt alloys can exhibit either a disordered phase (fcc-based L11-CoPt) and/or a hcp-based D019-Co3Pt crystal structure depending on the composition between Co and Pt. X-ray diffraction (XRD) and transmission electron microscope (TEM) was employed to study the microstructure and crystal structure of Co-Pt nanowires (NWs) with 200 nm diameter. Results are given elsewhere. [3] Detailed analysis on NWs have shown the presence of a textured fcc and hcp phases with the [111] of fcc and [001] of hcp crystal planes almost perpendicular to NWs long axis. Such analysis have explained periodic domains structure observed with magnetic force microscope (MFM) along the length of the NWs as shown in Fig.2. Such domain structure is ideal for racetrack memory devices. In future we are planning to perform current induced domain wall motion experiments to move these domain along the length of NWs.

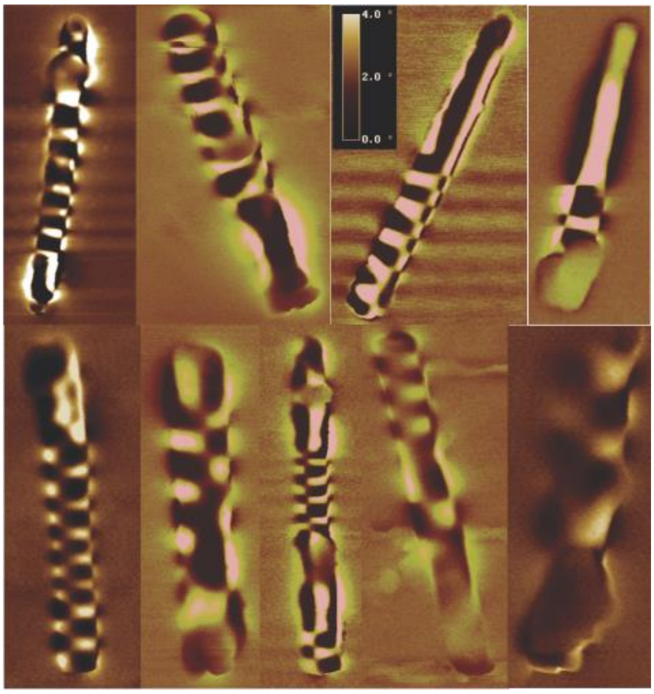

Figure 2: Periodic domain structure along the length of the Co-Pt nanowires with diameter around 200 nm.

II. Nanostructures with tube-wire morphology

We have successfully fabricated Co-Pt nanostructures with 200 nm diameter with tube-wire morphology as shown in Fig.3. We have studied their magnetization reversal and it turns out that transverse as well as vortex domain wall nucleation contribute to the magnetization reversal depending on the geometrical parameters. A plateau (kink) in the hysteresis curve (Fig. 4a) was observed which may be attributed to the partial pinning of the domain walls at the tube-wire interfaces.

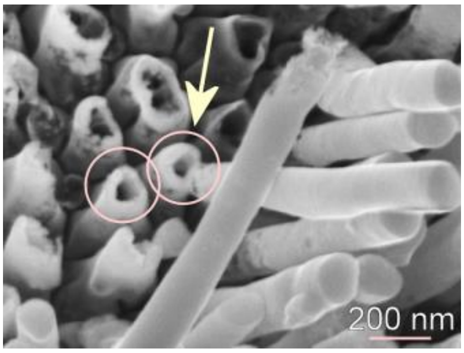

Figure 3: SEM image of nanostructure with tube-wire morphology.

We have performed micromagnetic simulation using a micromagnetic simulator [4] based on Landau-Lifshitz-Gilbert equations. Co-Pt nanostructures with tube-wire morphology were invested and we found out that this kink is present in the hysteresis loop as shown in Fig. 4b. This kink is representing a partial domain pinning during the magnetization reversal at the interface between tube and wire. [5]

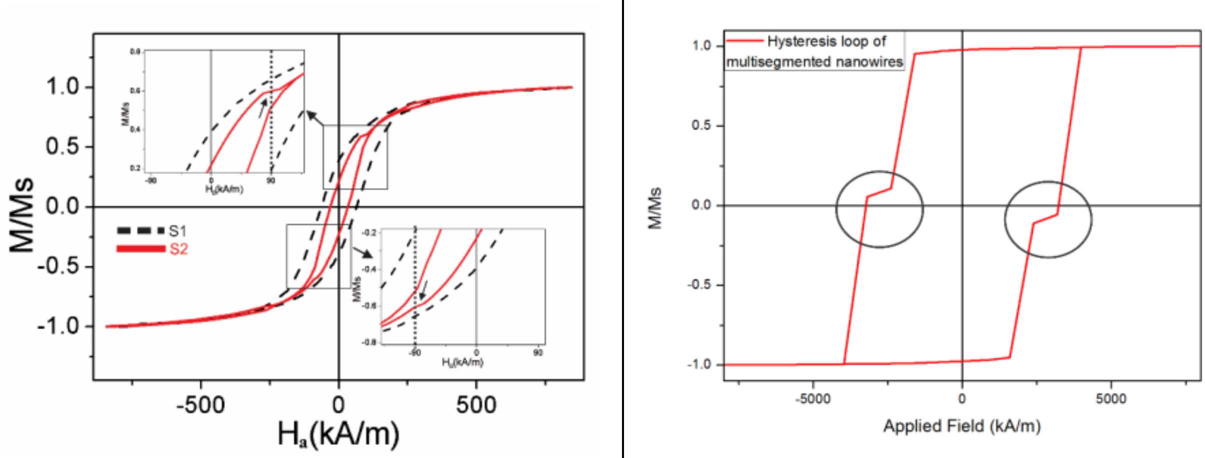

Figure 4a: Hysteresis loop of nanostructure with tube-wire morphology. **b:** Simulation hysteresis of nanostructure with tube-wire morphology

Pinning of the domains at the interface is represented in simulation as shown in Fig. 5.

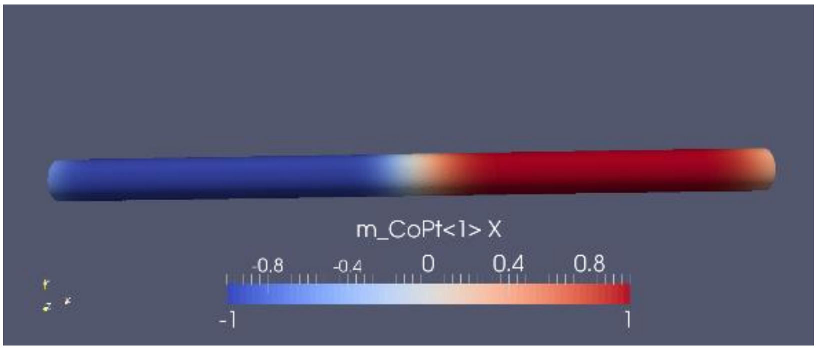

Figure 5: Micromagnetic simulation results of nanostructure with tube-wire morphology showing domain pinning at the interface between tube and wire.

III. Pinning of domain wall with physical notches on Nanowires

Recently a focused ion beam (FIB) was utilized to produce notches with different sizes and shapes along the length of the Co-Pt NWs with 50 nm diameters. MFM imaging was applied to observe magnetic domain patterns in NWs lying horizontally on substrates. In order to inject the domain walls into the wire a magnetic field (~500 Oe) was applied perpendicular to NW axis. We were successful to trap the domain walls in the Co-Pt NWs at the induced notches with the depth ~50% of the NWs diameters as shown in Fig. 6. However, further optimization of notches in the Co-Pt NWs is necessary in order to utilize them for racetrack memory devices. Moreover, micromagnetic simulations of notched NWs are in progress which will be followed by spin-induced domain wall motion experiments in the future.

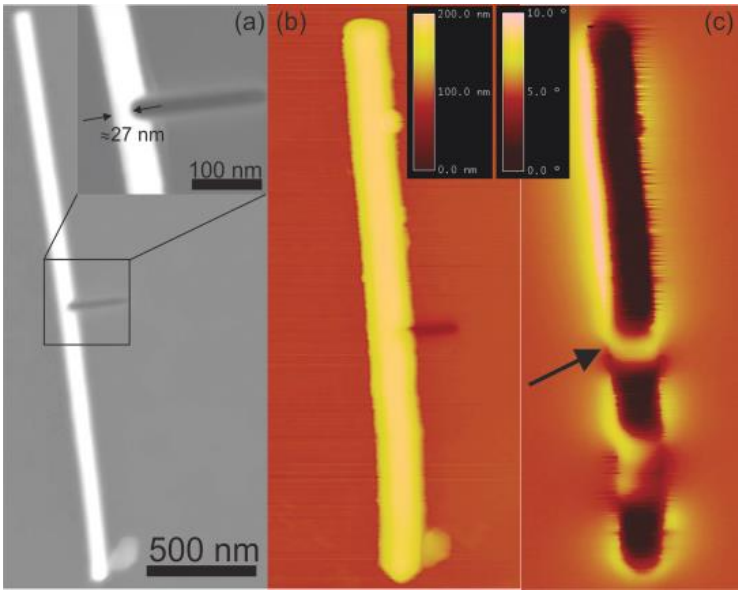

Figure 6: (a) SEM image of the Co-Pt nanowire with a notch in the middle, (inset) closeup image of the notch area. (b) AFM image (c) MFM image

References:

[1] http://researcher.watson.ibm.com/researcher/view_group_subpage.php?id=3811, 04-04-2015.
[2] S. S. P. Parkin, M. Hayashi and L. Thomas, "Magnetic Domain-Wall Racetrack Memory," *Science* vol. 320, pp. 190-194, 2008.
[3] M. S. Arshad, S. Šturm, J. Zavašnik, A. Espejo, J. Escrig, M. Komelj, P. McGuiness, S. Kobe and K. Rožman, "Effect of magnetocrystalline anisotropy on the magnetic properties of electrodeposited Co–Pt nanowires," *Journal of Nanoparticle Research* vol. 16, pp. 1-16, 2014.

[4] Nmag — a micromagnetic simulation environment, http://www.soton.ac.uk/~fangohr/nsim/nmag, 2012.

[5] M. S. Arshad, D. Pecko, S. Sturm, J. Escrig, M. Komelj, P. J. McGuiness, S. Kobe and K. Z. Rozman, "Angular Dependence of the Coercivity in Electrodeposited Co-Pt Nanostructures With a Tube-Wire Morphology," *IEEE Trans. Magn.* vol. 50, pp. 1-4, 2014.

For wider interest

Magnetic hard disk drives have been the prime repository of digital data for more than half a century. Over this period of time, the area of one magnetic bit, use to store information has decreased in size by about around nine order to magnitudes; it is now so tiny that it is reaching fundamental limit that are difficult or too expensive to overcome. A number of alternatives to the magnetic disk drive have been suggested. Among them racetrack memory devices seems to be potential candidates and close to the realization. Such devices are based on magnetic nanowires with magnetic domains which can be move with electrical current. In this article we have presented the possibilities to produce such nanowires which can be utilized in racetrack memory devices and we have also presented the methods to manipulate magnetic domains in nanowires.

Kazalo Avtorjev (List of Authors)

Sodelujoča podjetja in organizacije:

Institut
”Jožef Stefan”
Ljubljana, Slovenija

ISO
Fd
Food
ERA Chair
Safety
Quality
Traceability

greener

ADORA

IZVOR
by OriginTrail

SPIRIT
SLOVENIJA
JAVNA AGENCIJA
I FEEL SLOVENIA

REPUBLIKA SLOVENIJA
MINISTRSTVO ZA GOSPODARSKI
RAZVOJ IN TEHNOLOGIJO

LJUBLJANSKI UNIVERZITETNI
INKUBATOR


ECO
samples
compounds
tea
bread
high
mercury
products
temperature
activity
separation
provide
care
release
environment
materials
fate
results
fractionation
organic
chromatographic
columns
exist
applied
PPCPs
human
data
ketoprofen
confirm
spite
run
years
milk
gas
MoS2
work
stable
information
different
presence
enables
Monolithic
experiments
effects
low
follow
structure
study
monolithic
several
chromatography
small
coal
solid
sunscreen
speciation
substrates
related
catalytic
recent
50Cr
adulteration
complex
offer
isotope
analysis


new
materials
magnetic
nanoparticles
applications
IPS
high
methods
network
properties
coding
sensor
sensors
compounds
activity
drug
model
work
data
using
process
system
based
samples
learning
body
main
organic
mercury
physical
node
information
wireless
machine
rules
study
iron
well
being
Ta2O5
human
different
developed
measured
years
way

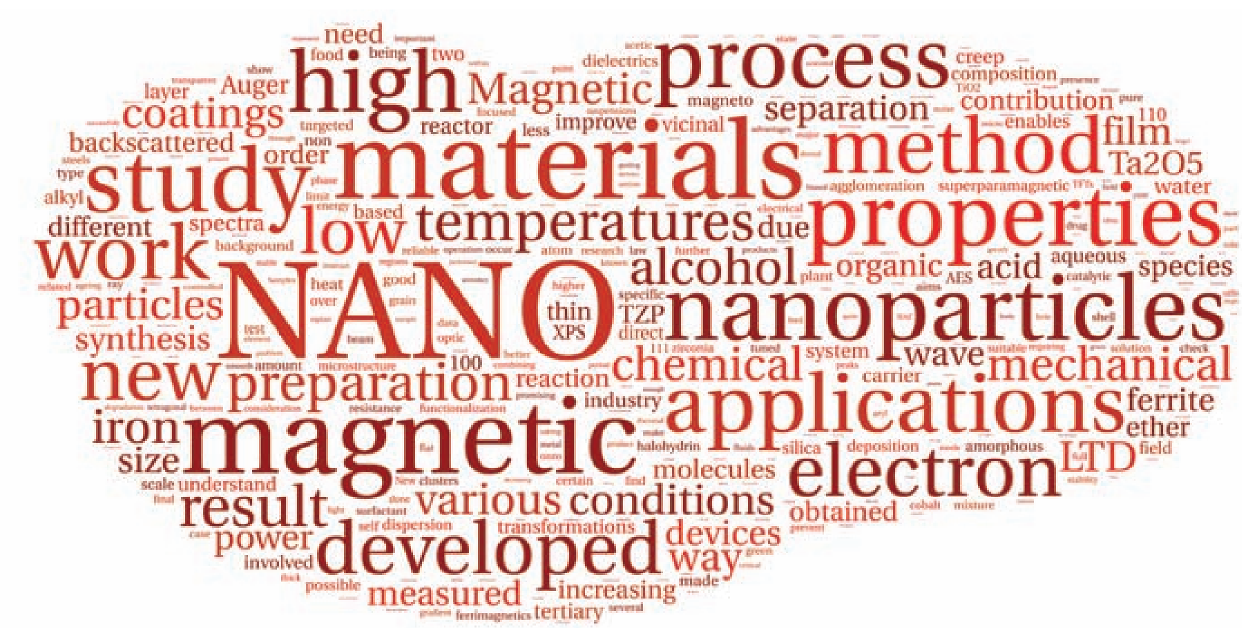
NANO
materials
magnetic
nanoparticles
properties
applications
process
high
study
method
temperatures
developed
electron
new
work
low
preparation
particles
synthesis
alcohol
chemical
mechanical
result
various
conditions
coatings
Magnetic
iron
size
power
measured
devices
way
film
Ta2O5
separation
dielectrics
Auger
backscattered
spectra
organic
acid
aqueous
species
water
ferrite
ether
LTD
wave
reaction
thin
TZP
XPS
obtained
increasing
tertiary
molecules
need
creep
composition
contribution
superparamagnetic
agglomeration


ICT
model
network
system
learn
data
rule
process
sensor
coding
node
method
develop
activity
approach
applications
predict
wireless
new
human
routing
biological
amount
machine
drug
fall
domain
physical
packet
using
result
user
function
measured
build
information
semantic
knowledge
tool
language
pattern
gene
detect
hand
thus
described
construct
show
optimization
smartphone
platform
towards
exist
means
way
news
inertial
artificial
dynamical
computers

MEDNARODNA
PODIPLOMSKA ŠOLA
JOŽEFA STEFANA

JOŽEF STEFAN
INTERNATIONAL POSTGRADUATE SCHOOL

Jamova 39, SI-1000 Ljubljana

T +386 (0)1 477 31 00
F +386 (0)1 477 31 10

E info@mps.si
www.mps.si

ISBN 9789619287194
9 789619 287194

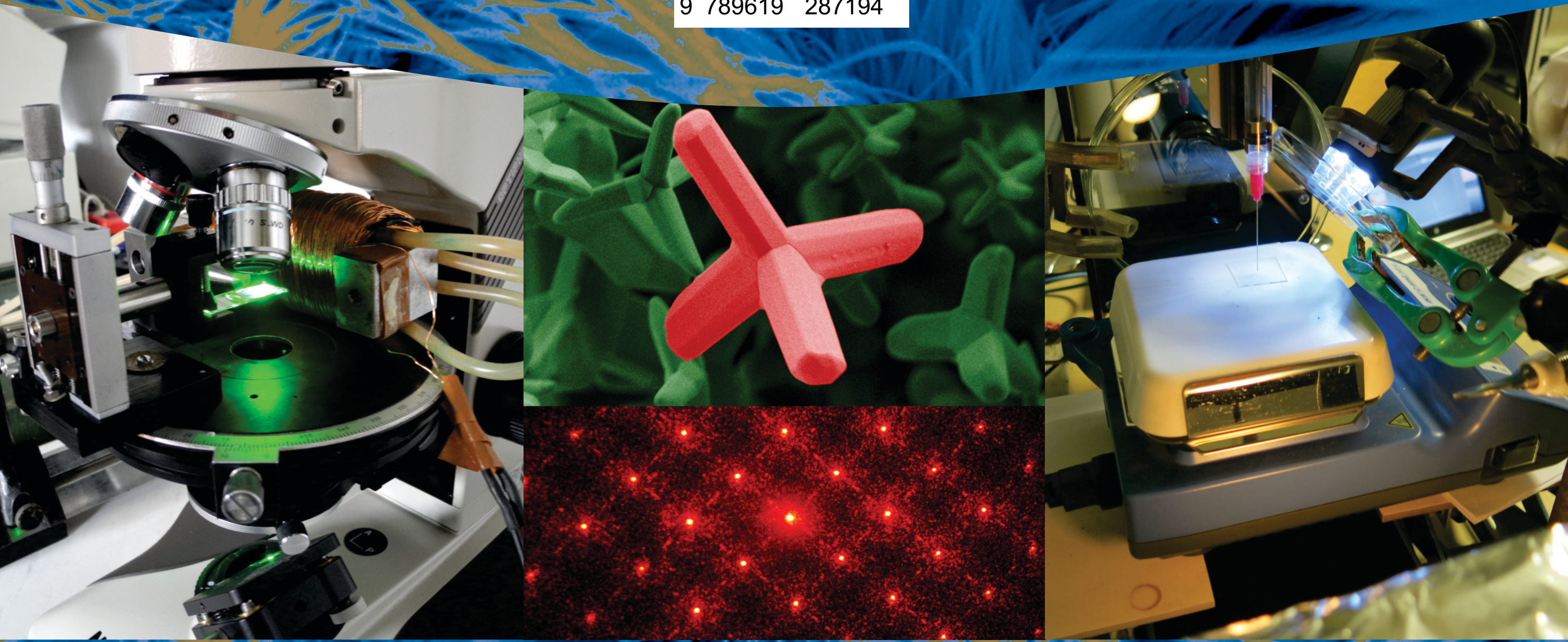

20. - 21. 05. 2015, Ljubljana